Mohamed Boudiaf University - M’sila

FACULTY OF TECHNOLOGY

DEPARTMENT

Serial number:……

Registration number: **D.CM/3C/06/21**

Thesis

Presented for obtaining the diploma of

LMD DOCTORATE

Sector: Mechanical Engineering

Option: Mechanical construction

THEME

Numerical and Experimental study of a bio composite material reinforced with lignocellulosic fibers

Presented by

SAADA Khalissa

Supported on: 11/05/2024

In front of the jury composed of:

Rokbi Mansour	**Professor**	University of **M’sila**	President
Zaoui Moussa	**Professor**	University of **M’sila**	Supervisor
Amroune Salah	**Professor**	University of **M’sila**	Co- Supervisor
Moussaoui Mustafa	**Professor**	University of **Djelfa**	Examiner
Farsi Chouki	**MCA**	University of **M’sila**	Examiner

Academic year: 2023/2024

Acknowledgments

To commence, we extend our heartfelt gratitude to the Almighty for providing us with strength and perseverance, guiding us through this endeavor. Special recognition is owed to ***Professor Moussa Zaoui****, our supervisor, and* ***Professor Salah Amroune*** *for their unwavering guidance and support throughout the entirety of this project.*

A special thank you goes to ***Pr. Rokbi Mansour*** *at the University of M'sila, who chaired the jury with distinction. Gratitude is also expressed to the members of the jury, including* ***Pr. Moussaoui Mustafa*** *at the University of Djelfa, and* ***Dr. Chouki Farsi*** *at the University of M'sila.*

We sincerely thank the Head of the Mechanical Engineering Department and all the educators who played a crucial role in guiding us throughout our educational journey.

Additionally, our appreciation extends to the Technology Hall staff for their cooperation and assistance, with special gratitude to Dr: ***Abdraouf Khaldoune*** *and Dr:* ***Belkacem Aoufi****. Furthermore, we acknowledge the invaluable contributions of* ***Dr. Amina Hachaichi*** *and Engineer* ***Said*** *from the University of Boumerdes, who contributed significantly to our results in the tensile test. Our gratitude also extends to* ***Dr. Madani Grine*** *at the University of M'Sila for supplying the silicone material from El-Elma, and* ***Naana Houssem*** *from Constantine, who assisted in printing samples using a 3D printer. Without forgetting to express our sincere thanks, we extend our gratitude to the honorable professors* ***Amin Houari*** *and* ***Kouider Madani*** *from the University of Sidi Bel Abbes And also* ***Pr Mohammed Jawaid*** *from the University of*

*Malaysia . We would like to express our thanks to **Loran** Company (Bouira) for generously providing 5 kg of epoxy used in this research.*

*Finaly, I dedicate this doctoral thesis to my family, with a special tribute to the late my dad **Tahar**, may God have mercy on him. I extend my heartfelt gratitude to my mother, **Aicha**, whose unwavering support has been instrumental in the completion of this thesis. May God protect her.*

Khalissa

Contents

Contents

Contents

Contents

List of Figures

List of Figures

List of Figures

List of Tables

List of abreviations

[PLA]: Polylactic acid.

[FEM]: Finite element method.

[RSM]: Response surface methodology.

[ANN]: Artificial neural network.

[FTIR]: Fourier transform infrared

[ANOVA]: Analysis of Variance

[PD]: Peridynamic.

[ABS]: Acrylonitrile butadiene styrene.

[OHT]: Open-hole tensile.

[CAD]: Computer-aided design.

[K_t]: Concentration factor.

[UTM] Universal Testing Machine.

[ODE]: Ordinary differential equation.

[A]: Area (mm^2).

[F]: Force (N).

[f]: The distributed force (N)

[σ]: Stress component (MPa).

[ε]: **S**train components (%).

[S]: Compliance matrix of the material.

[E]: Young's modulus (MPa).

[$\mathcal{V}$ **]** Poisson's coefficient .

[ρ **]** Aangular/linear deformation.

[UP] Unsaturated polyester.

[3DP] 3D printing.

[RP] Rapid prototyping.

[FDM] Fused deposition modeling.

[YL] Universal testing Machine.

ملخص

بعد توقيع بروتوكول كيوتو في عام 1997، تحول الاهتمام تدريجياً نحو التنمية المستدامة وتقليل البصمة الكربونية، خاصة في مجالات البحث والابتكار. ظهرت المواد المركبة المعززة بألياف نباتية كبديل مباشر لمواجهة هذه التحديات البيئية مع تحسين الأداء الميكانيكي وزيادة المتانة. تعتبر هذه المواد بديلاً بيئياً للمواد المركبة التقليدية، التي غالباً ما تصنع من ألياف اصطناعية مشتقة من موارد غير متجددة. من خلال استخدام ألياف نباتية مثل الكتان والقنب والجوت وربما الكيناف، توفر هذه المواد فوائد بيئية هامة، حيث تقلل من الاعتماد على الموارد الأخرى وتساهم في تقليل انبعاثات الغازات الدفيئة على مدار دورة حياتها، من الإنتاج إلى نهاية استخدامها. تركز هذه الدراسة على تصنيع قوالب من السيليكون لإنتاج عينات للاختبار الميكانيكي والانحناء، بالإضافة إلى بناء هياكل النحل بأشكال هندسية متنوعة، باستخدام تقنية الطباعة ثلاثية الأبعاد ومادة البوليلاكتيك الحمضية (PLA). الهدف هو إنتاج مواد حيوية مركبة معززة بالإيبوكسي والبوليمرات بألياف طبيعية مختلفة مثل نخيل التمر وسيسال واللوفا والجوت. تم تصنيع عينات من الإيبوكسي عن طريق إدراج ثقب في المنتصف، ثم تم تقييم سلوكها الميكانيكي من خلال اختبارات الجر، مع التحقق الرقمي باستخدام برنامج أباكوس. تم تحسين الخصائص الميكانيكية للمواد الحيوية المركبة المعززة بألياف طبيعية باستخدام شبكات العصب الاصطناعي ومنهجية استجابة السطح، مما أظهر ترابطاً خطياً مع النتائج التجريبية.

الكلمات الرئيسية: عناصر محدودة، ANN، RSM، الألياف الطبيعية، المركبات الحيوية، الهندسة

Résume

Après la signature du protocole de Kyoto en 1997, l'attention s'est progressivement portée sur le développement durable et la réduction de l'empreinte carbone, notamment dans les secteurs de la recherche et de l'innovation. Les matériaux composites renforcés de fibres végétales ont alors émergé comme une solution prometteuse pour répondre à ces défis environnementaux tout en offrant des performances mécaniques améliorées et une durabilité accrue. Ces matériaux sont considérés comme une alternative écologique aux composites traditionnels, souvent fabriqués à partir de fibres synthétiques provenant de ressources non renouvelables. En utilisant des fibres issues de plantes telles que le lin, le chanvre, le jute, voire le kenaf, ces matériaux présentent des avantages environnementaux significatifs. Ils permettent de réduire la dépendance aux ressources non renouvelables et en contribuant à la diminution des émissions de gaz à effet de serre tout au long de leur cycle de vie, de la production à la fin de leur utilisation. Cette étude se concentre sur la fabrication de moules en silicone pour la création d'échantillons de traction et de flexion, ainsi que sur la construction de structures en nid d'abeille avec divers motifs géométriques, en utilisant l'impression 3D et le matériau d'acide polylactique (PLA). L'objectif est de produire des bio-composites d'époxy et de polymères renforcés par différentes fibres naturelles comme le palmier-dattier, le sisal, le luffa, le sisal et le jute. Des échantillons d'époxy ont été fabriqués en insérant des trous au milieu, puis leur comportement mécanique a été évalué par des tests de traction, avec une vérification numérique effectuée à l'aide du logiciel Abaqus. Les propriétés mécaniques des bio-composites renforcés de fibres naturelles ont été améliorées en utilisant des réseaux de neurones artificiels (ANN) et la méthodologie de surface de réponse (RSM), montrant une corrélation linéaire avec les résultats expérimentaux.

Mots-clés : Éléments Finis, ANN, RSM, Fibre Naturelle, Bio-composites, géométrie

Abstract

After the signing of the Kyoto Protocol in 1997, attention gradually shifted towards sustainable development and carbon footprint reduction, particularly in research and innovation sectors. Plant fiber-reinforced composite materials emerged as a promising solution to address these environmental challenges while offering improved mechanical performance and increased durability. These materials are considered an eco-friendly alternative to traditional composites, often made from synthetic fibers derived from non-renewable resources. By utilizing fibers from plants such as flax, hemp, jute, and even kenaf, these materials offer significant environmental advantages. They help reduce dependence on other resources and can contribute to reducing greenhouse gas emissions throughout their lifecycle, from production to end-of-life use. This study focuses on the fabrication of silicone molds for creating traction and flexion samples, as well as the construction of honeycomb structures with various geometric patterns, using 3D printing and polylactic acid (PLA) material. The goal is to produce epoxy and polymer bio-composites reinforced with different natural fibers such as date palm, sisal, loofah, and jute. Epoxy samples were manufactured by inserting holes in the middle, and their mechanical behavior was evaluated through traction tests, with numerical verification using Abaqus software. The mechanical properties of natural fiber-reinforced bio-composites were enhanced using artificial neural networks (ANN) and response surface methodology (RSM), demonstrating a linear correlation with experimental results.

Keywords: Finite Elements, ANN, RSM, Natural Fiber, Bio-composites, geometry

General Introduction

In recent years, scientific researchers and industrial experts have focused their efforts on biocomposite materials, due to their properties of being sustainable, renewable, biodegradable, and biocompatible. Biocomposites can be used in different fields of applications, especially in light structures and it is necessary to determine their mechanical properties through different experimental techniques used under different types of loads such as traction, compression, torsion, fatigue and impact. The study of the geometric effect of samples on mechanical properties has gained importance from many authors, including the honeycomb. The effect of hole size and position on the mechanical properties of tensile specimens was also experimentally studied using peridynamic (PD) theory and compared numerically using the code developed in MATLAB ,ANSYS , employing optimization methods.

In this context, our primary goal for this thesis is to investigate how the mechanical characteristics of a plant fiber-reinforced composite evolve when subjected to tensile, compressive, and flexural tests. The second objective is to simulate and predict the properties of the composite based on the observed behaviors. The natural fibers selected for this study include palm fibers, jute, sisal, diss, and luffa, chosen for their remarkable mechanical properties. The thesis is structured into five chapters to comprehensively address these research objectives.

Chapter I: provides a comprehensive overview by defining composites and specifying the roles and properties of their components, specifically fibers and matrices. The spotlight is on plant fibers, and a thorough literature review is conducted to uncover potential challenges associated with them. This chapter is instrumental in framing the research problem, revisiting fundamental concepts, and establishing the groundwork for the thesis. It also delves into the various matrices that can be paired with these natural fibers, with a notable emphasis on thermoplastics due to their capacity to maintain

the eco-friendly characteristics offered by the fibers. Giving priority to numerical and experimental studies, the focus is placed on both computational simulations and practical investigations.

Chapter II: The second chapter aims to describe the implementation of samples in various forms Honeycomb(hexagonal, Re-entrant, star-fish), tensile, and bending samples. It includes the presentation of structures based on standard dimensions, along with a detailed account of the different stages involved in creating silicon molds, starting from design to manufacturing. The explanation also covers all the machines and tools used throughout this study

Chapter III: delves into a detailed exploration of the mechanical properties of three composite structures—honeycomb, re-entrant, and starfish—reinforced with palm, jute, and sisal fibers, utilizing epoxy resin. The fabrication of these structures involves casting processes within silicone molds. Furthermore, the chapter elucidates the mechanical properties of tensile epoxy samples with and without hole notched, while also presenting an account of the bending properties of biocomposite samples.

Chapter IV: The objective of this chapter is to propose a mixed XFEM formulation for the elasto-plastic analysis of stress and strain. The goal is to investigate the impact of a geometric discontinuity on the tensile strength of an epoxy-type polymer. Tensile tests were conducted on specimens featuring different forms of geometric discontinuity (hole, elliptical notch). The influence of these geometric shapes (hole and ellipse) on the mechanical properties of the polymer was examined and compared with unnotched samples. Experimental results were juxtaposed with those obtained through finite element numerical analysis using ABAQUS software. The effect of the geometric notch shape was assessed in terms of maximum stress and maximum deformation.The stress concentration factor (Kt) in different epoxy specimens was also determined.

Chapter V: The objective of this chapter is to employ an optimization program, utilizing both response surface methodology (RSM) and artificial neural networks (ANN). This approach seeks to discern the impact of input parameters on the output parameters, specifically focusing on the mechanical properties highlighted in our thesis. Simultaneously, the identification of promising fibers for structural applications is a key aspect of this endeavor. The assessment involves evaluating complex responses under varied conditions, encompassing stress, strain, Young's modulus, and water absorption.

CHAPTER I:
Literature review

I.1. Introduction

This chapter unveils itself in two distinct parts. Part One immerses readers in the realm of biocomposites and natural fibers, offering an insightful exploration of current knowledge surrounding plant fibers. This encompasses discussions on the intricacies of chemical modification and fiber extraction methods. Furthermore, it delves into the domain of plant fiber-reinforced composite materials, illustrating exemplary applications across diverse fields. The concluding part seamlessly intertwines methods of modification and improvement, culminating in the introduction of the fundamental Finite Element Method (FEM) process.

I.2. General information on composite materials

Composite material can be defined as the fusion of two or more materials, resulting in a final assembly that possesses properties superior to those of each individual constituent material. These materials are often referred to as reinforcement arrangements or fillers, which are embedded in a matrix [1, 2] .The synthesis of natural fiber composites involves the amalgamation of diverse natural fiber preforms with matrix resins obtained from natural or synthetic polymers. These matrix resins fall into two categories: thermosets or thermoplastics. The classification of composite materials is based on their reinforcement, which can be divided into particle reinforcement, fiber reinforcement, and structure reinforcement. **Figure I.1**. shows the different forms of reinforcing the composite material, with fibers being the most commonly used due to their lightness, stiffness, and strength. Fibers have stronger properties than the base material due to the alignment of molecules and fewer defects. Fibers can be classified according to length (short, long, continuous), and chemical composition (organic, inorganic), as shown in **Figure I.2.** The matrix of the composite material holds the fibers together and transfers load through the interface to the reinforcing fiber and the composite from an external source. There are three major types of matrices: polymer, metal, and ceramic matrices [3].

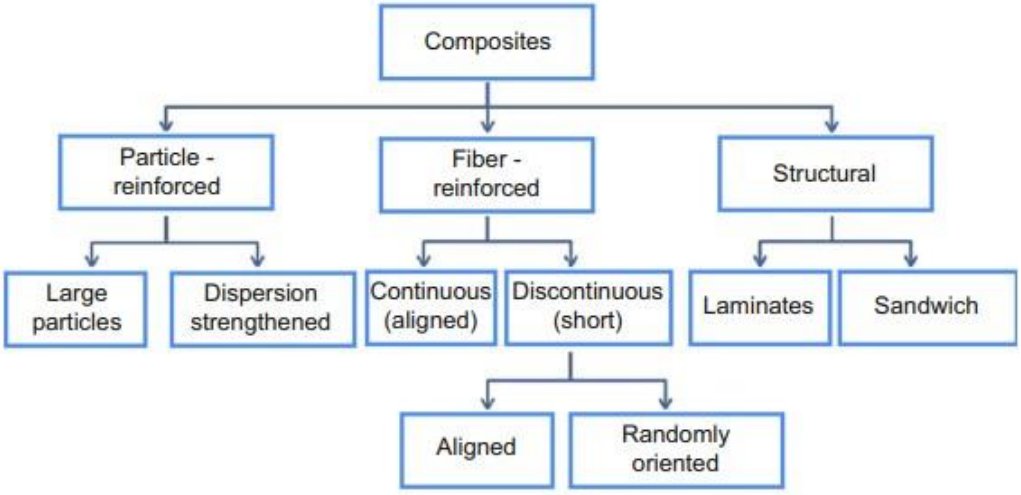

Figure I.1: The categorization of composite reinforcement [4]

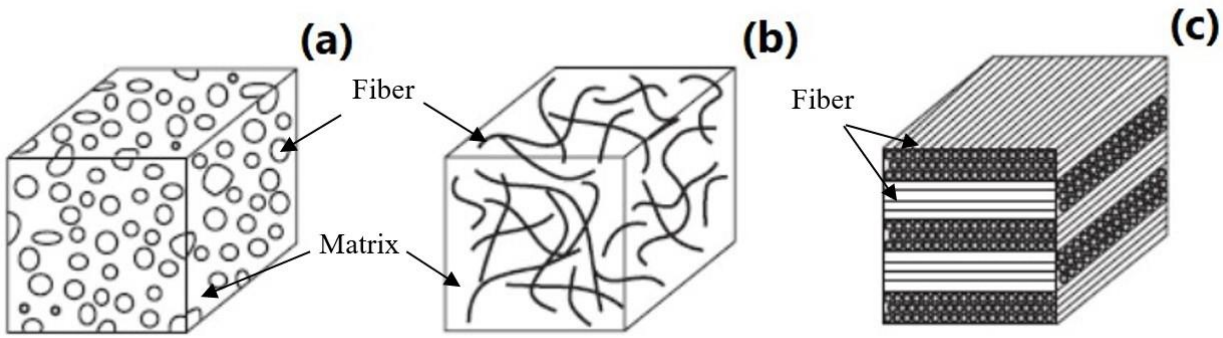

Figure I.2:The reinforcement geometries of composite materials include: (a) particulate composites, (b) Short Fibers composites and (c) laminar composites [5]

I.3. Plant fibers

Natural fibers refer to fibers that are either manmade or not synthetic. These fibers can be found in both plants and animals. The utilization of natural fiber from these sources can be either renewable or nonrenewable in nature[6, 7]**.**The utilization of natural fiber can be both renewable and nonrenewable depending on the resources used. There is a wide variety of

natural cellulose fiber available, including flax, hemp, sisal, banana, kenaf, jute, and oil palm fruit bunch cellulose fiber. In recent decades, there has been significant attention towards composite materials made from jute fiber. The plants that produce cellulose fibers can be categorized into different groups, such as bast fibers (jute, flax, ramie, hemp, and kenaf), seed fibers (cotton, coir, and kapok), leaf fibers (sisal, pineapple, and abaca), grass and reed fibers (rice, corn, and wheat), core fibers (hemp, kenaf, and jute), as well as other types of fibers (wood and roots)[9 ,8]. Natural fibers offer numerous benefits in comparison to synthetic ones. They are recyclable, biodegradable, renewable, possess relatively high strength and stiffness, and do not cause skin irritation. Presently, the utilization of natural fiber reinforcement has gained significant popularity among researchers. Chemically treated natural fibers have shown improvements in impact toughness and fatigue strength. Furthermore, they are readily available at low costs, biodegradable, eco-friendly, and have lower density compared to synthetic fibers[10] . Plants that produce natural fibers are categorized into primary and secondary plants based on their purpose. Primary plants are specifically cultivated for their fiber content, while secondary plants are those that yield fibers as a by-product. Examples of primary plants include jute, hemp, kenaf, and sisal, whereas pineapple, oil palm, and coir are examples of secondary plants[11].

The table presented in **Table I.1**. displays photographs representing the sources of various natural fibers.

Table I. 1: Images highlighting the origins of various natural fibers

Name of plant	*Image of plant*	*Fiber of plant*	*References*
Enset			[12]
Sisal			[12]
date palm			[13]
cotton			[14]
jute			[15]
Diss			[16]

Figure I.3. Illustrates the global production of these fibers natural in a graphical representation. At the same time. Displays photographs representing the sources of various natural fibers. According to the report, Brazil and Tanzania are the leading producers of sisal fiber, while Bangladesh, China, and India are the primary producers of jute fiber.[17]

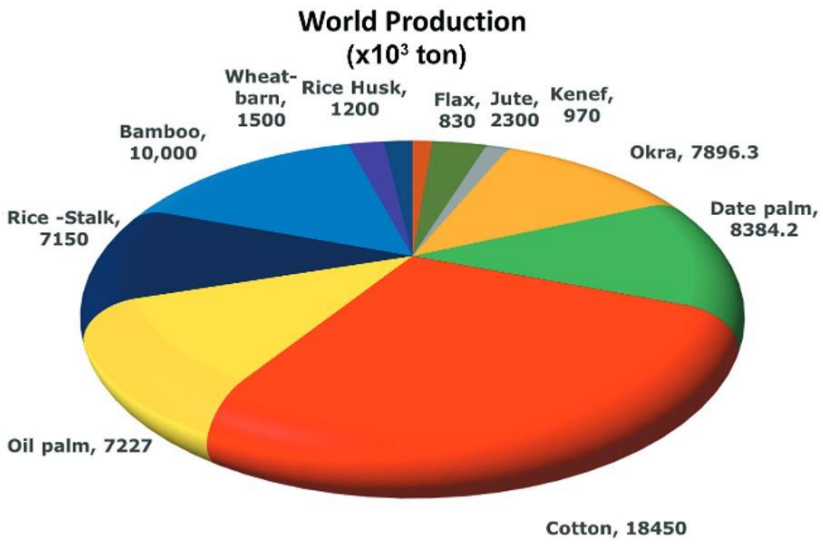

Figure I. 3: International manufacturing of natural fibers. [18]

I.3.1. Date palm fibers

The date palm belongs to the Arecaceae family and is cultivated for its renowned fruits, dates. It stands out for its prolificacy and high resistance to cold and drought. With ancient origins, the cultivated date palm is believed to have originated in western India or the Persian Gulf region. It can be found in all hot zones of North Africa, from the Sahara to the Red Sea, as well as in the Middle East and extending eastwards to the Indus region. It primarily thrives between latitudes 15 and 30 degrees north. Beyond this zone, it can be cultivated, but yields either no fruits or fruits of mediocre quality. The date palm has been introduced on all five continents, particularly in the Americas since the 16th century and in Australia since the 19th century. It is commercially grown in North Africa (Algeria), the Middle East, and the United States[19].

I.3.2. Luffa fibers

Luffa, also known as sponge gourd, belongs to the vegetable sponges family[20]. It is widely distributed in countries such as China, India, and Japan. Young luffa plants serve multiple purposes; they can be consumed as a vegetable and utilized for medicinal reasons[21]. Luffa fiber, obtained from the fruit of the Luffa cylindrica plant, is a naturally occurring biological material. These cellular fibers exhibit exceptional specific mechanical properties and are commonly used for packaging and cladding applications to protect products from collisions and impacts. Furthermore, Luffa, in conjunction with other natural fibers, can be reinforced with various thermoplastic and thermosetting matrices, such as epoxy novolac resin[22].

I.3.3. Jute fibers

Jute, derived from various plants belonging to the Corchorus genus, which comprises approximately 100 species, is considered one of the most affordable natural fibers. It currently holds the title for being the fiber with the highest production volume. Bangladesh, India, and China are known for providing the most favorable conditions for jute cultivation[8]. Jute, known for its softness, glossiness, and strength, is a coarse thread derived from plant fibers. Jute fiber is extensively utilized in the packaging of agricultural and industrial products, such as bags, sacks, packs, and wrappings. Jute fibers offer effective insulation against both thermal and acoustic energy, exhibit minimal moisture absorption, and do not cause any skin irritations[23] .

I.3.4. Diss fibers

Ampelodesmos mauritanicus, also known as Diss in Arabic, is a large grass plant native to Northern Africa, Southern Europe, and the dry regions of Greece and Spain. It belongs to the Poaceae family. This grass grows naturally and has a chemical composition comprising 44-46% α-cellulose, 26-27% hemicelluloses, 17-25% lignin, and 1.3% fats and waxes. The mineral

content, including SiO_2, Al_2O_3, Fe_2O_3, CaO, Na_2O, and K_2O, can vary from approximately 8-10% depending on factors such as plant growth conditions, soil composition, and growth climate[24].

I.3.5. Sisal fibers

Sisal, obtained from the Agave sisalana plant, is produced both in East Africa and Brazil. The plant closely resembles giant pineapples, and during the harvest, the leaves are separated from the pulp and plant material, leaving behind the sturdy fibers. These fibers are then softened either by hand or machine. Following this, the fibers are dried and brushed to eliminate any remaining dirt. Sisal is known for its strong fiber, as well as its full biodegradability, high tenacity, high tensile strength, toughness, resistance to abrasion, acid and alkali, corrosion resistance, and ability to withstand exposure to seawater[7]. Furthermore, Zhang et al[25]. utilized a benzylation treatment to convert wood flour into thermoplastics and combined both discontinuous and continuous sisal fibers to create plant fiber composites from renewable resources. Degradation tests confirmed that the sisal/plasticized wood flour composites were completely biodegradable. To expedite the decomposition process, the cellulose and lignin in the composites should be taken into consideration. When contemplating practical applications, it is crucial to consider the hydrophobicity and flame resistance of the composites. Molecular modification and/or the inclusion of inorganic additives are appropriate actions, provided the biodegradability of the composites remains unaffected. Additionally, Alvarez et al [26] examined how the creep behavior of random-oriented sisal fiber/starch composites, manufactured using injection molding, is affected by the fiber content. They conducted short-term flexural creep tests and observed that a higher fiber content in the matrix resulted in improved creep resistance.

The structure of the fiber-cell is displayed in **Figure I.4.**Individual fiber-cells are connected through the middle lamella, consisting of hemicellulose and lignin. The lumen's size varies, but its shape is typically well-defined (**refer to Figure I.4.b**). Each fiber-cell comprises four main parts: the primary wall, the thick secondary wall, the tertiary wall, and the lumen (as depicted in **Figure I.4.c**) [27].

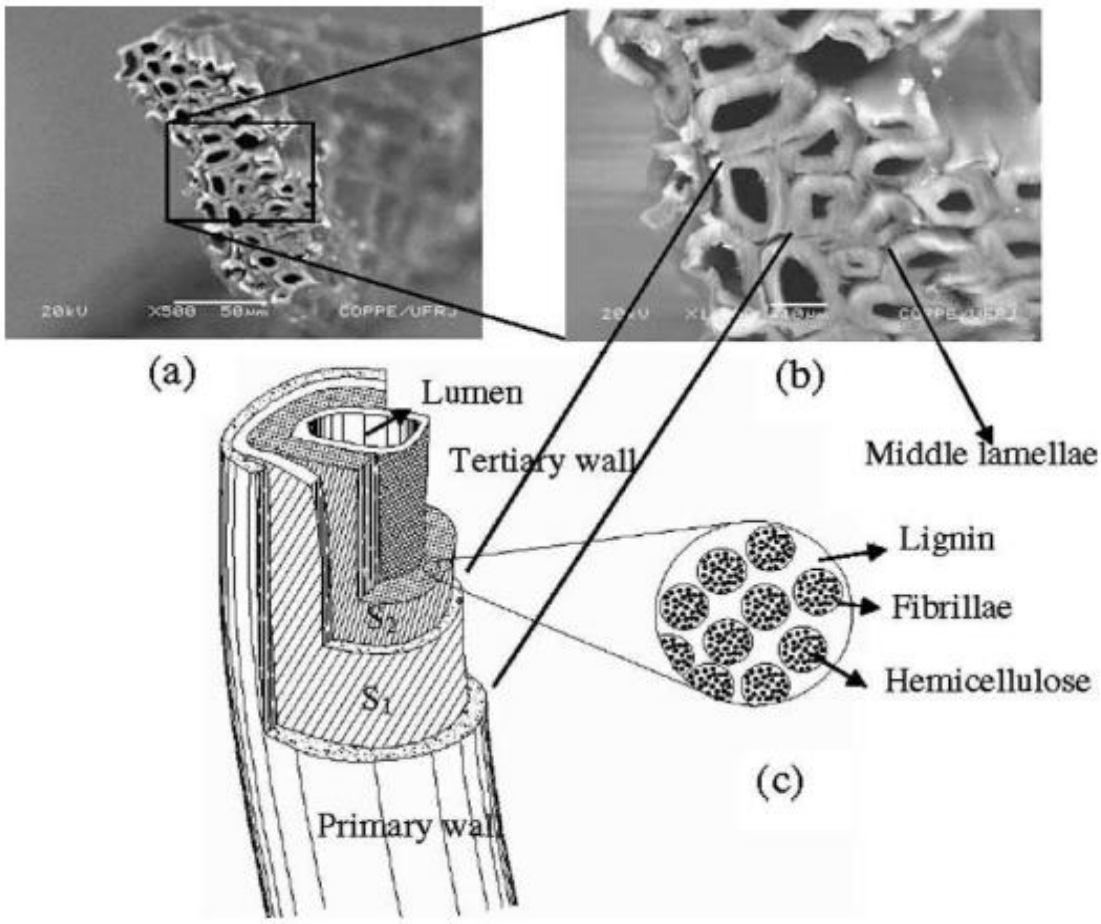

Figure I.4: the microstructure of the fiber-cell is depicted, including (a) a cross-sectional view revealing fiber-cells, lumens, and middle lamellae, (b) a closer examination of the cross-section, and (c) a schematic drawing outlining the different la [27]

I.4.Extraction of plant fibers

Several plants can be a source of fibers, with extraction possible from roots, leaves, stems, or clusters, as exemplified by the palm tree. In our case, it is necessary to highlight various fiber extraction methods to enhance comprehension of the extraction techniques. The pulping processes commonly employed today are illustrated in **Figure I.5.**

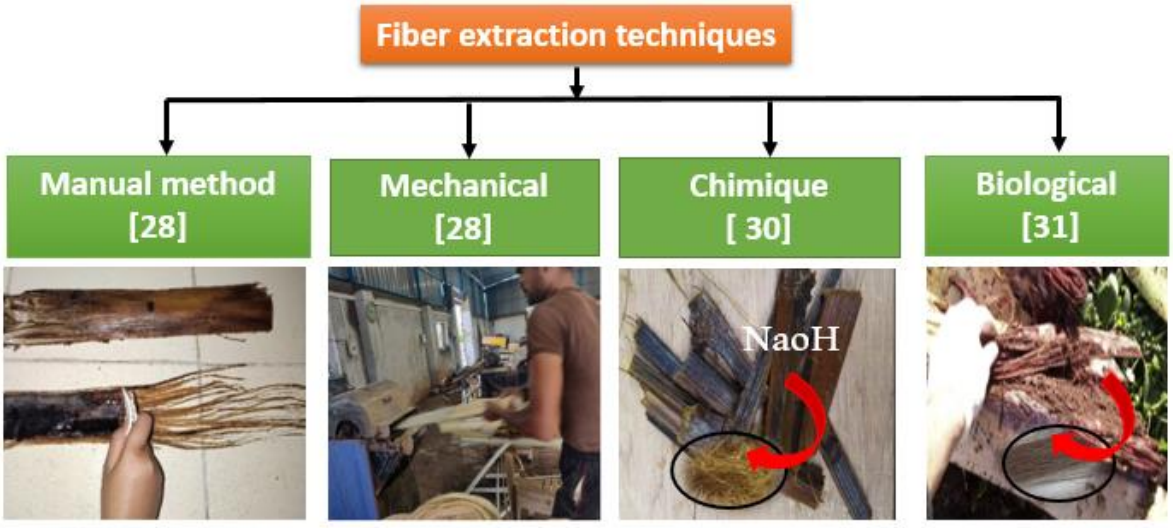

Figure I. 5: Diagram of plant fiber extraction techniques [28-31]

I.4.1. Manual method

The manual method is a primitive and simple extraction technique achieved through direct extraction using sharp tools like blades or pottery fragments. This method is commonly used in villages and rural regions. While it yields high-quality fiber with minimal debris on the surface, the process is labor-intensive and results in limited production, making it impractical for extensive-scale manufacturing[32] .During the manual production of fibers, they are gathered from river banks and subsequently immersed in water for approximately 168 hours[33, 34]. After this soaking period, the fibers are air-dried at room temperature to reduce their moisture content, thus rendering them suitable for textile applications. The separation of fibers from the plant tissues involves a manual peeling process, which in turn enables the

detachment of the stem bundle from the draining water. Following this step, the stems are individually stripped. Once the fibers are amassed into clusters, a cleaning procedure is carried out. The stems encased within the fibers are grasped and pounded on surfaces until the root ends are adequately crushed and detached [33, 34].The loosely intertwined fibers can then be isolated from the rest of the stems. These fibers are subsequently extracted, organized, and subjected to cleaning. Gently massage the plant's surface until the outer layer is eliminated, revealing the plant's fibers that necessitate careful drying [35, 36].

I.4.2.Mechanical method

It is a technique that depends on spinning through a decorticator machine. This machine comprises cylindrical drums with a 30 cm diameter, equipped with blades. The blades facilitate the separation of fibers during the spinning motion. The fiber extraction process lasts about 10 seconds. Overall, mechanical extraction can lead to significant fiber damage caused by intense high-speed mechanical agitation[28, 37].

I.4.3.Water retting (Biological method)

The primary and widely acknowledged approach for producing natural fibers involves water retting. In this method, clusters of stalks are submerged in water. Eventually, the water seeps into the stems, causing an increase in moisture content, resulting in the outermost layer rupturing. This elevated moisture absorption leads to the presence of damp air and the growth of decomposing bacteria. When yeast is employed in cloth production, it necessitates the careful selection of the optimal harvesting time, a decision crucial for the cloth maker. As mentioned in the preceding slide, the process entails delicately submerging the bark's grain into water through a raking procedure, and the fiber undergoes several months of retting in an anaerobic environment before it becomes usable. Natural water retting takes advantage of still or slow-moving water bodies such as ponds, sluggish streams, bogs, and rivers[33, 35, 38].

I.4.4.Chemical method

Retting is commonly carried out using alkaline or mildly acidic solutions. Enzymes are introduced to initiate the process of fiber separation. Among alkalis, caustic soda is the prevailing choice, while mild acids such as oxalic acid and sulfuric acid, when combined with detergent, are also employed for fiber extraction. It's worth highlighting that the relative composition of the treatment solution plays a pivotal role in influencing the resulting fiber quality[39]

I.4.5.Biological method

The utilization of microorganisms like bacteria and enzymes in the biological treatment process is an environmentally friendly method for extracting of good quality fibers from plants. This technique offers several benefits, such as achieving a high yield, minimizing energy consumption, and enhancing selectivity. However, it's important to note that this approach also has drawbacks, including its relatively high cost and the extended duration required, which imposes limitations on its practical application[40, 41].

I.5.Chemical surface treatment of plant fibers

The plant fibers offer a compelling option as a substitute for synthetic fibers, particularly glass fibers. The primary challenge faced by these cellulosic reinforcements is the issue of achieving a satisfactory level of adhesion between the fiber and the matrix. Consequently, numerous research papers focus on the surface treatment of the fibers to enhance the adhesion between the fiber and matrix[42]. After the chemical treatment of natural fibers, their mechanical properties are greatly affected by various factors, such as fiber length, fiber aspect ratio, and fiber-matrix adhesion[7].The reason fibers are chemically modified is because their hydrophilic nature causes them to adhere poorly to the polymer matrix. The defined process involves treating a vegetable fiber with a concentrated aqueous solution of a strong base, causing

substantial swelling and resulting in alterations to the fine structure, dimensions, morphology, and mechanical properties[19]. There are various treatments available for treating natural fibers, including sodium chloride NaCl , Hydrogen chloride Hcl and Ethanoic acid CH_3COOH[43].In this discussion, we will focus on two types of treatments: the first being the most commonly used treatment involving NaOH, and the second being an environmentally eco-friendly option sodium carbonate $NaHCO_3$.

I.5.1.Traitement NaOH

Alkaline treatment is commonly utilized for chemically modifying natural fibers. One of the significant benefits of this treatment is the alteration or breakdown of hydrogen bonding within the entire structural system, resulting in increased surface roughness. Additionally, alkaline treatment partially removes lignin, oils, and wax from the outer layer of the fiber cell wall. The treatment also depolymerizes cellulose in the fiber, thereby exposing shorter length crystallites. With reference to Eq. $(I.1)$below, the presence of an aqueous solution of sodium hydroxide (NaOH) promotes the ionization process of the hydroxyl group into an alkoxide [40, 44].

$$Fiber-OH+NaOH \rightarrow Fiber-o-Na+H_2O \ldots\ldots\ldots \textbf{(I.1)}$$

Furthermore, when treating fibers with NaOH, impurities like pectin, lignin, and other contaminants are eliminated from the surface layer, resulting in an enhancement of surface roughness[45]. In other study, the study found that this treatment increased the tensile strength by (+17.8%), modulus by (+6.9%), flexural strength by (+16.7%), and modulus by (+7.4%) in comparison to untreated fibers. Based on these findings [46].

I.5.2.Traitement $NaHCO_3$

Sodium bicarbonate ($NaHCO_3$), commonly recognized as baking soda, is utilized as an environmentally eco-friendly chemical treatment[47]. Moreover, $NaHCO_3$ served as widely accessible and cost-effective fillers commonly employed to reduce composite production expenses and enhance thermal properties. Where , the incorporation of nanocellulose into nanocomposites has shown considerable advancements in their thermal and mechanical characteristics[48]. Additionally, NaHCO3 leads to the liberation of sodium ions while also giving rise to the creation of carbonic acid and hydroxide ions. The interaction between the fibers and the sodium ions closely resembles the process observed in alkali treatment. Due to its mild alkaline nature, $NaHCO_3$ is deemed safe for natural fibers. The fibers are subjected to the treatment by being submerged in a solution containing $NaHCO_3$. The reaction of $NaHCO_3$ in water is represented by the subsequent formulas for the solute[47].

$$NaHCO_3 \rightarrow Na^+ + HCO_3^- \quad \text{..... (I.2)}$$

$$HCO_3^- + H_2O = H_2CO_3 + OH^- \quad \text{..... (I.3)}$$

As the concentration of sodium bicarbonate increases, the tensile and flexural properties of the material improve. In both instances, the strongest strength is achieved with a 10 % treatment, surpassing the untreated and 5 % treatment options. This may be attributable to the 10 % treatment modifying the surface topography of the used fibers. This synergy between the fibers and matrix leads to the production of high-strength natural composites[49]. In addition to , The application of sodium carbonate treatments enhances both the tensile strength and modulus of the composite [50].Fiore et al [51] utilized Sisal plants that were harvested and processed. Where, specific portions of the cleaned fibers were immersed in a 10 wt% $NaHCO_3$ solution for varying durations of 24 h, 120 h, and 240 h, all at room temperature. Afterward, the fibers

were thoroughly washed with distilled water and subjected to drying in an oven set at 40°C for 24 h. Tensile tests were carried out using a Universal Testing Machine (UTM). The results indicated a noticeable increase in both Young's modulus and tensile strength as the treatment time was extended up to 120 h. However, beyond the 120-hour mark, while Young's modulus continued to rise, the tensile strength of the treated fibers began to decline. This observed decrease in tensile strength might be attributed to degradation phenomena that tend to occur when the treatment time becomes excessively prolonged.

Figures I. 6 and **I .7** compare the experimental results of Young's modulus in tension and bending for epoxy samples reinforced with untreated jute/hemp/flax and those treated with sodium bicarbonate ($NaHCO_3$) and alkali (NaOH) at different concentrations (3%, 6%, and 9%), highlighting any variations in modulus values. The outcomes reveal a significant enhancement in both tensile strength and Young's modulus compared to the untreated reinforced fibers.

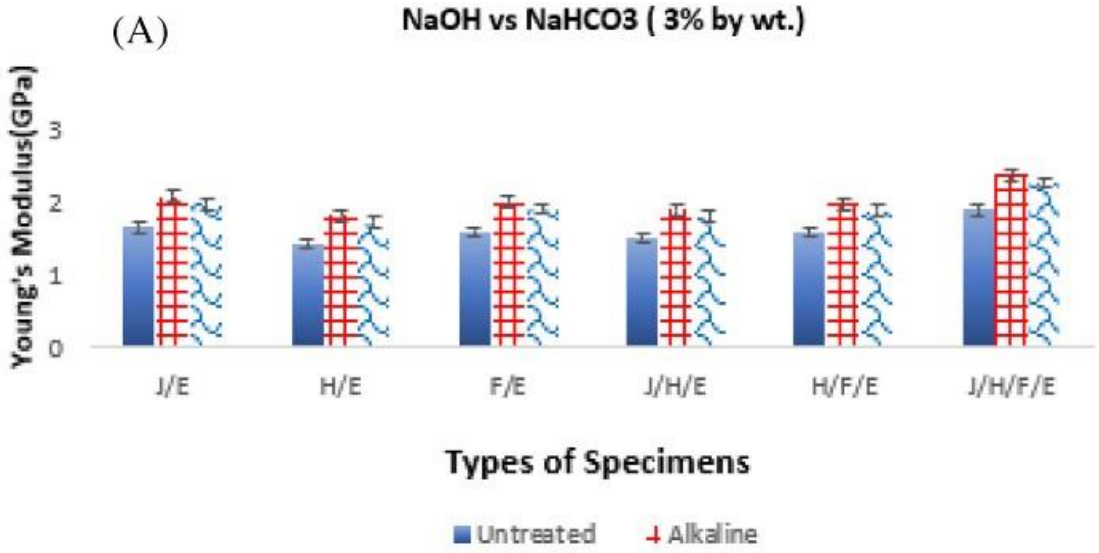

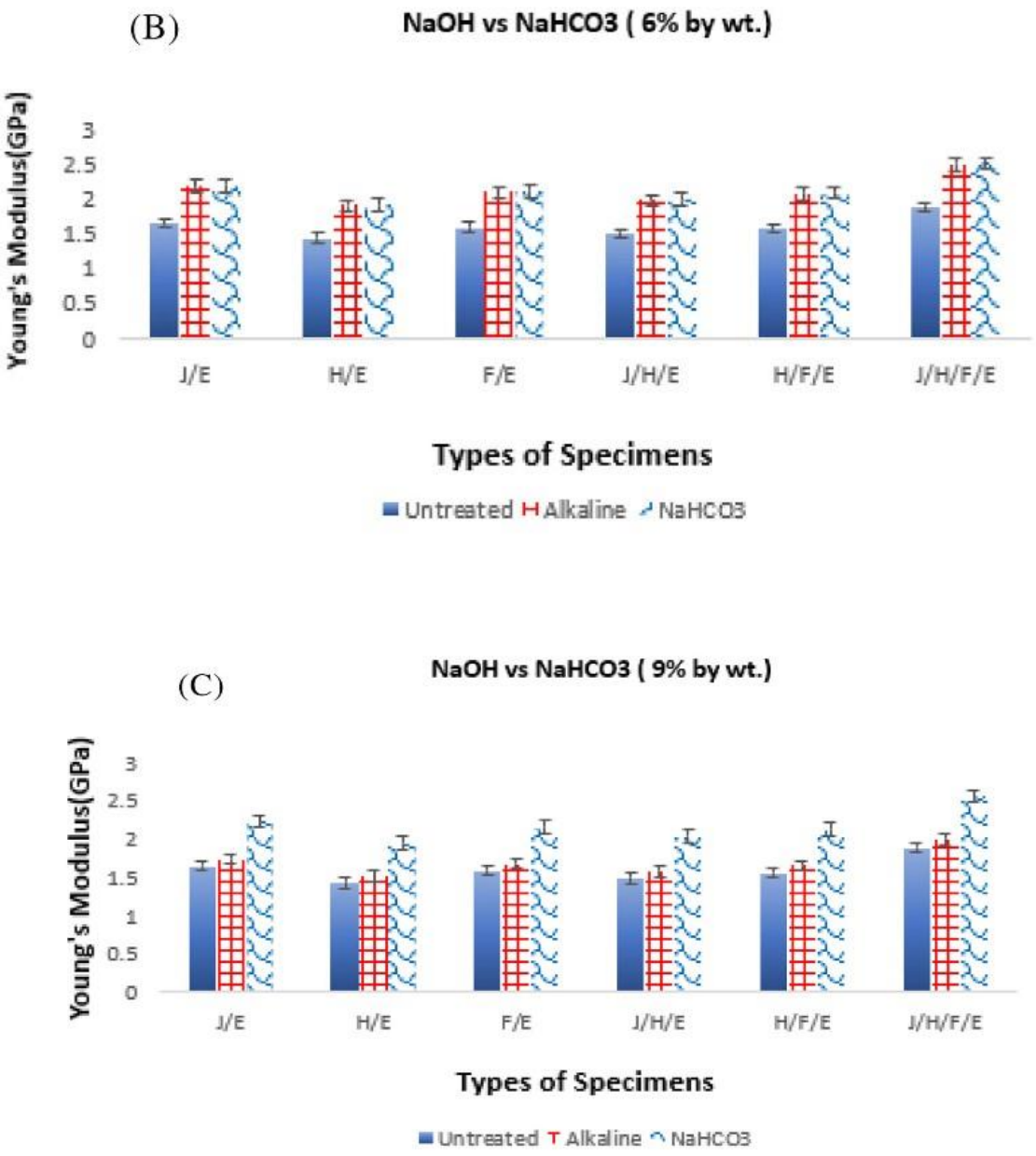

Figure I. 6: The tensile strength of different natural fiber composites after being treated with NaOH and $NaHCO_3$: (a) NaOH VS $NaHCO_3$ (3%), (b) NaOH VS $NaHCO_3$ (6%) and (c) NaOH VS $NaHCO_3$(9%) [52]

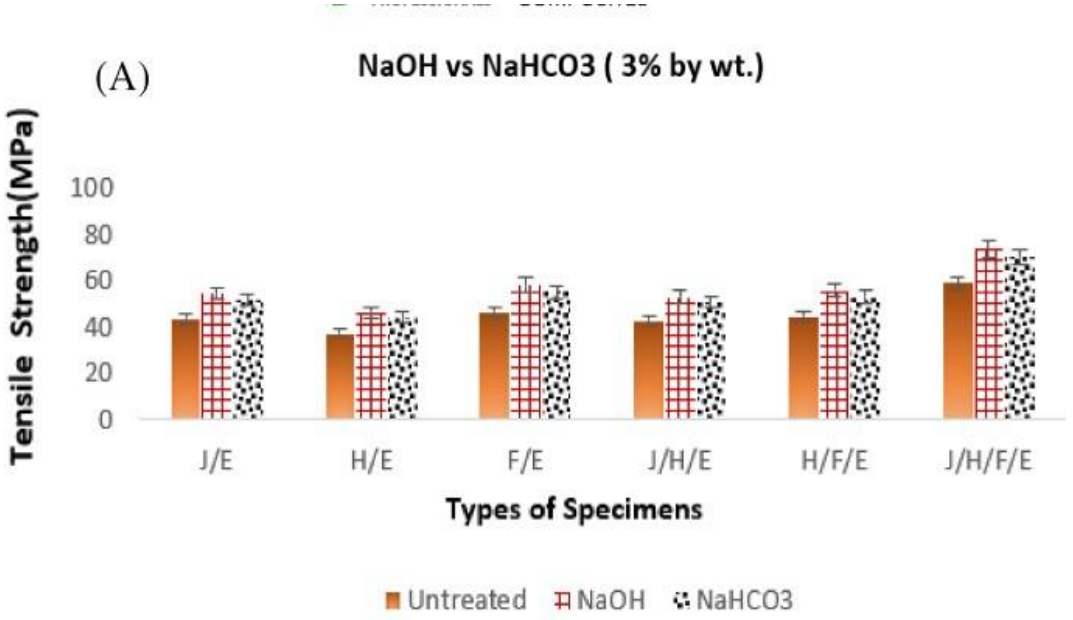
(A)
NaOH vs NaHCO3 (3% by wt.)
Tensile Strength(MPa)
100
80
60
40
20
0
J/E
H/E
F/E
J/H/E
H/F/E
J/H/F/E
Types of Specimens
Untreated
NaOH
NaHCO3

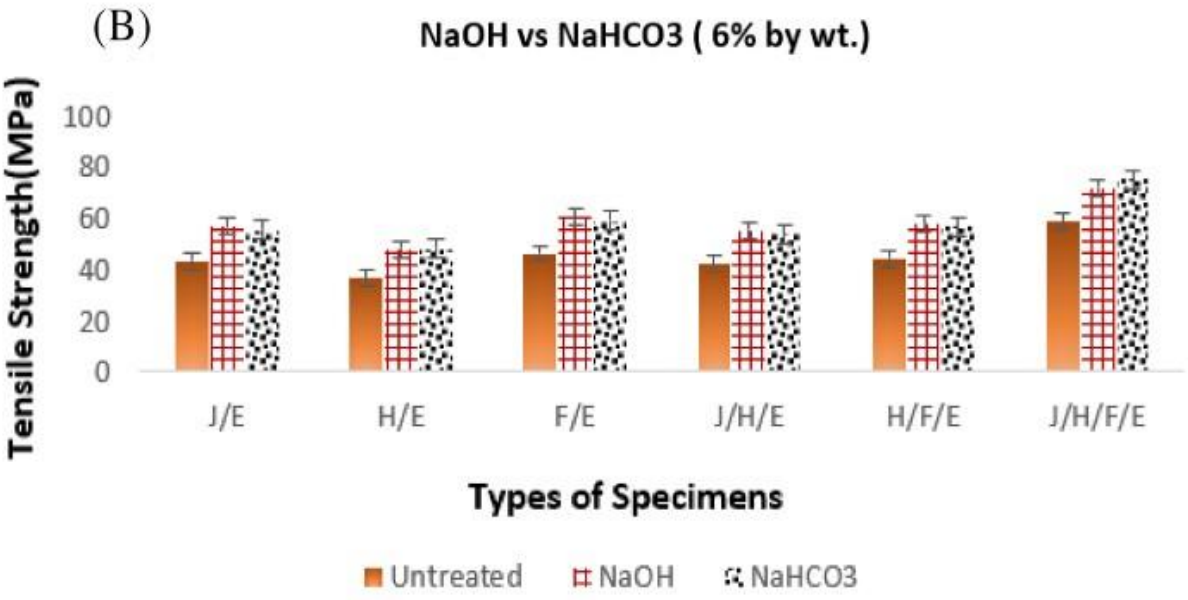
(B)
NaOH vs NaHCO3 (6% by wt.)
Tensile Strength(MPa)
100
80
60
40
20
0
J/E
H/E
F/E
J/H/E
H/F/E
J/H/F/E
Types of Specimens
Untreated
NaOH
NaHCO3

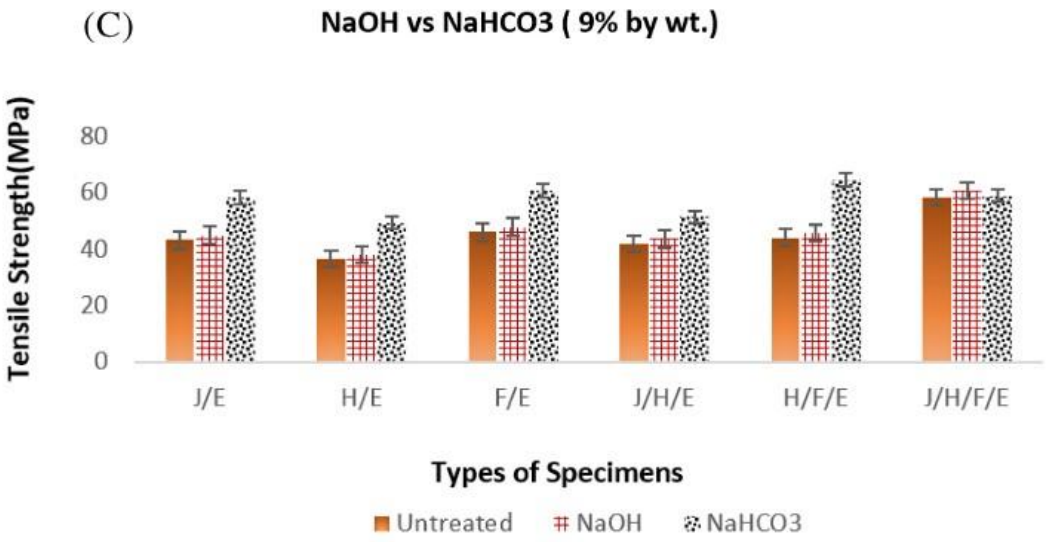

Figure I.7: The bending test of various natural fiber composites following treatment with NaOH and NaHCO33: (a) NaOH VS NaHCO3 (3%), (b) NaOH VS NaHCO3 (6%) and (c) NaOH VS NaHCO3(9%)

[52]

I.6. Applications and uses of composite materials

The prevalence of products made from bio fibers has risen, with an increased adoption in applications like window frames, decking, dashboards, parcel shelves, door panels, seat cushions, backrests, and cabin linings. The trend of favoring natural fibers over petroleum-based alternatives has gained momentum across various industries, including automotive, aerospace, marine, electrical and electronics, sports, recreational equipment, and machinery office equipment. This shift is driven by the appealing characteristics of bio fibers, such as their lightweight nature, recyclability, biodegradability, low processing costs, commendable mechanical properties, and resistance to corrosion and fatigue[53] . The chemical composition of these fibers varies not only between different plant species but also within distinct parts of the same plant, influenced by factors like geographic location, age, climate, and soil conditions.

Sisal fiber, obtained from sisal plants' leaves, is especially versatile, finding application in the creation of diverse products.[54].

As for sisal, fiber is unsuitable for textiles and fabrics due to its toughness and is not recommended for wall finishing purposes. Instead, it is primarily utilized for mats, roofs, carpets, cement reinforcement, the automobile industry, slippers, clothes, and disc buffers. However, there has been a decline in the global demand for sisal fiber products since 1998-2000. Despite this, sisal fibers are known for their durability, low maintenance cost, recyclability, resistance to moisture absorption, and excellent sound and impact absorbing properties[7].Also, the primary market for jute fibers lies in the production of bag cloth. Jute bags have become increasingly popular as a more environmentally friendly alternative to paper bags, which require the use of significant amounts of wood, and non-biodegradable poly bags made from petroleum[23] .In another study, the Diss plant has demonstrated intriguing mechanical and thermal characteristics, making it suitable for the creation of traditional construction materials in North Africa as well as artisanal baskets. Additionally, these fibers have been extensively researched due to their notable antiparasitic properties, which have long been associated with traditional use of this plant. In recent times, it has also been examined as a potential bioenergy resource, as these fibers contain minimal amounts of fats and waxes[55].

In India, there has been notable progress in the development of inorganic boards. Furthermore, researchers have explored innovative approaches by combining industrial and agricultural wastes with cement and cementitious materials as binders to create a diverse range of building materials. These inventive combinations find application in the manufacturing of composition boards, flooring tiles, roof sheathing, and weatherproof coatings. Shifting focus to the Middle East, particularly in Egypt, rice straw emerges as a crucial lignocellulose material used in the production of fiberboards. Despite its lower quality compared to wood fibers due to a higher

content of non-fibrous materials, careful processing of rice straw can significantly enhance the properties of the boards [56].

Moreover, in Asian countries, alternative agricultural fibers such as bagasse, hemp, cotton, and kenaf have been employed for producing hardboards, showcasing superior properties when compared to composition boards made from rice straw. In Saudi Arabia, manufacturers have opted for bagasse fibers as an alternative in composites for building materials. Meanwhile, in the Philippines, research efforts are concentrated on incorporating coconut coir, banana, and pineapple fibers with wood waste for particleboard production[56] .

The use of bio-composites in building materials offers several advantages, including cost-effectiveness, lightweight construction, environmental friendliness, bio-renewability, and enhanced durability. **Figures I.8, 9, 10** and **11** shows various applications of bio-composites.

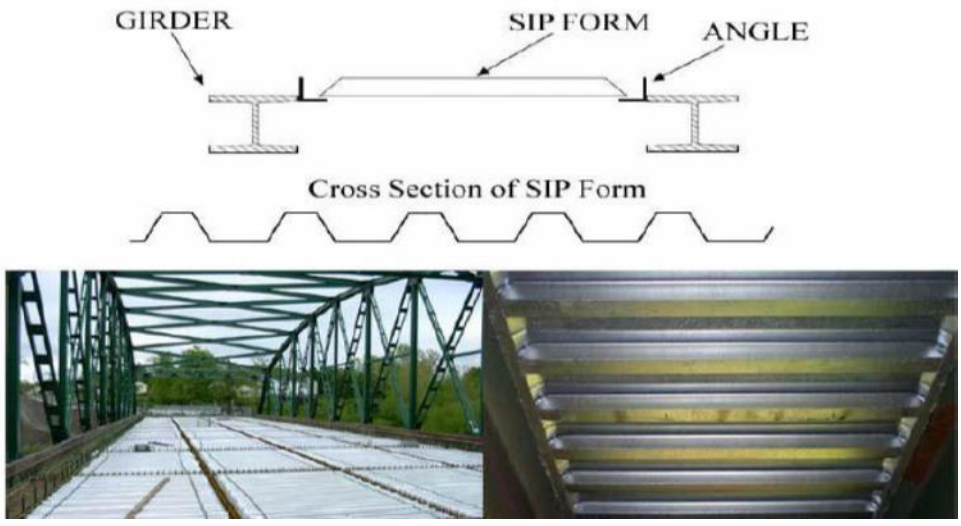

Figure I. 8:Stay-In-Place Bridge Form [56]

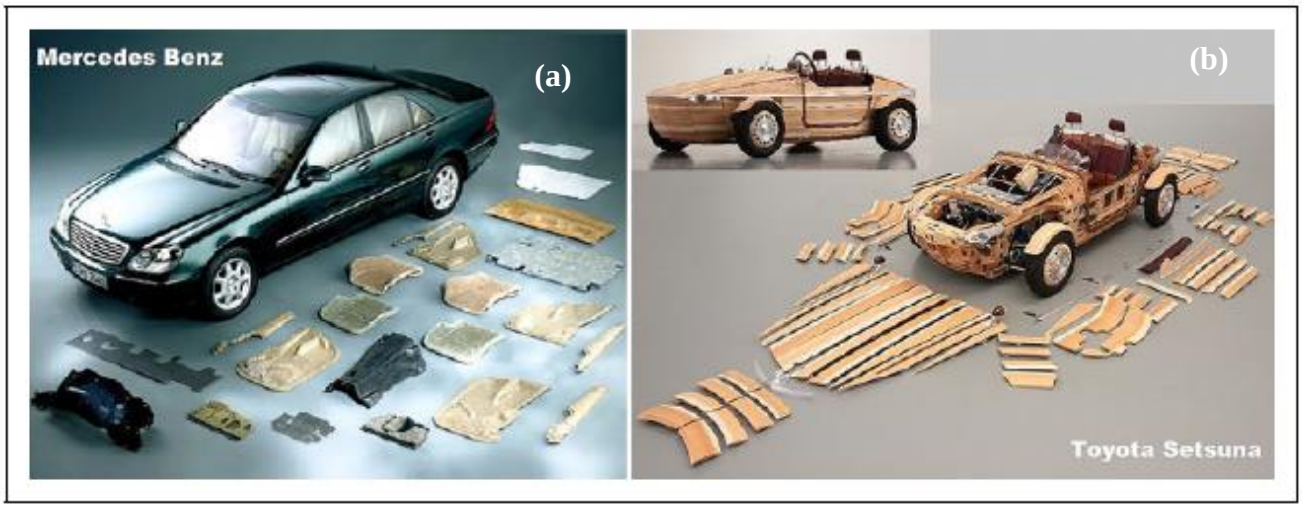

Figure I.9: Vehicle components manufactured using natural fiber composites: (a) Mercedes bens and (b) Toyota setsuna [57]

Figure I. 10:(a) Perfume containers shaped using wood flour-based composites; (b) Laptop casing constructed from hemp/PLA-based composites[7].

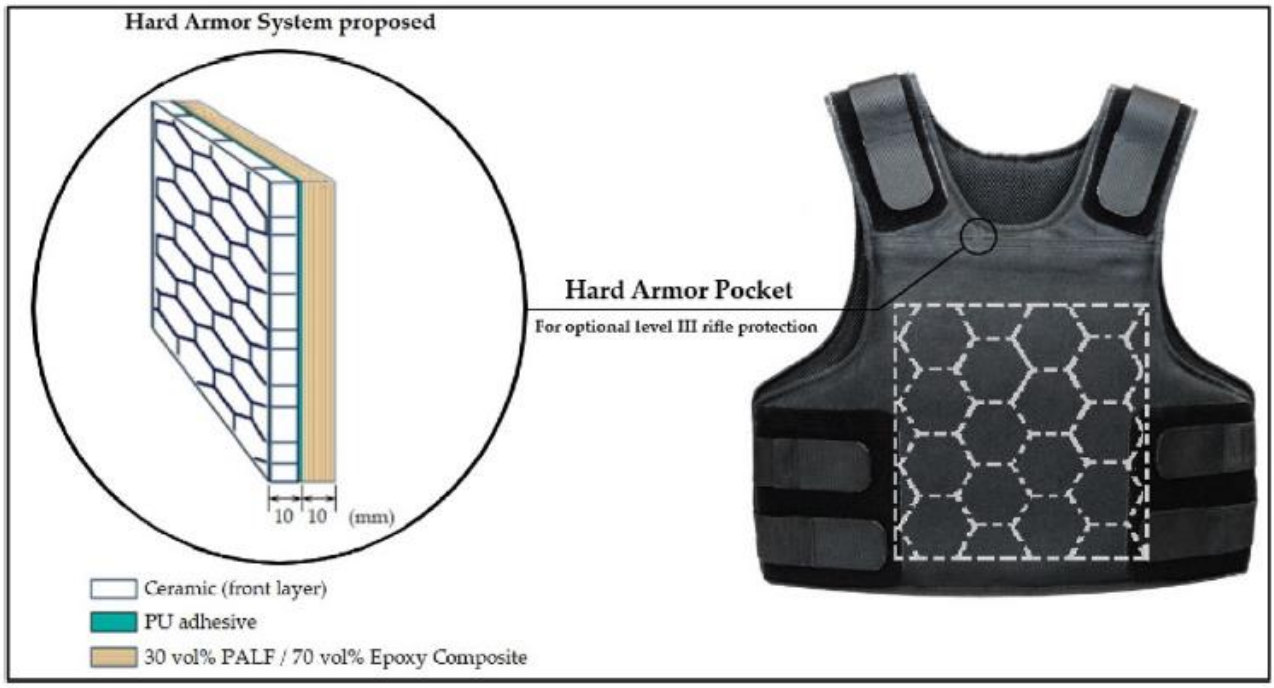

Figure I.11:A schematic diagram outlining the hard armor system designed to offer ballistics protection

[58].

In traditional civilizations, basketry and rugs serve practical purposes while also aiming to offer aesthetic satisfaction to both creators and users. Despite this dual role, it is noteworthy that, unlike several other African crafts like weaving and pottery, basketry has received minimal attention from art anthropologists or ethnologists in terms of research.as shows as **Figure I. 13.** In **Figure I.12**, the future outlook and utilization of natural fibers with biocomposites are illustrated.

Figure I. 12: Tangible Craft Product Derived from Fiber Art Material Created Throughout the Duration of this Study

[59].

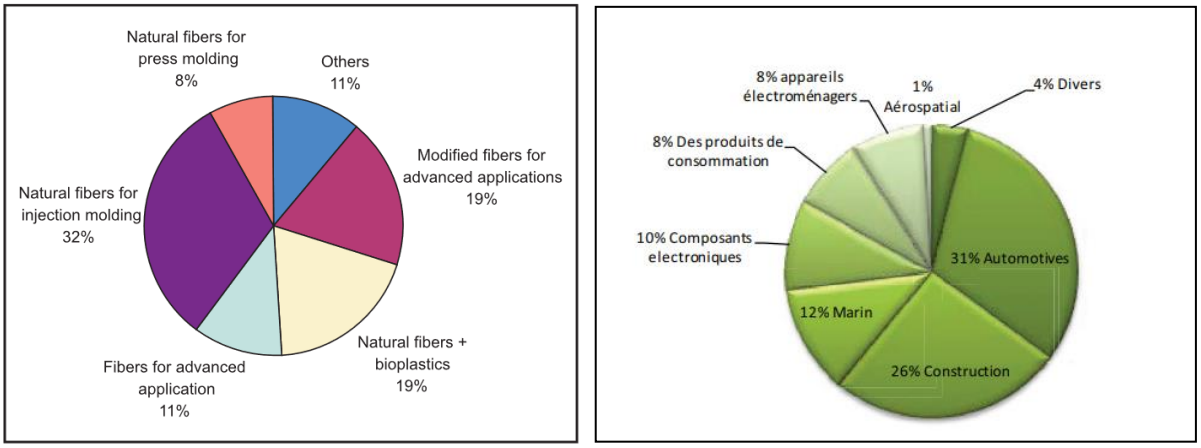

Figure I. 13: (a)Future Outlook,(b) Utilization of natural fibers and bio-composites [6]

I.7. Matrix

The choice of matrix stands as a pivotal factor in the classification of composites, and they can be grouped as follows:

➤ Organic matrix composites, presently dominating the realm of industrial composites, encompassing resins and fillers. Ceramic matrix composites, reserved for high-tech applications in extreme conditions, often involve nitride and carbide materials.

➤ Metal matrix composites, featuring lightweight and ultralight aluminum and magnesium alloys.

In numerous instances, the matrix can adopt various material forms. Polymeric matrices, being the most prevalent, constitute over 90% of composite materials [60]. These matrices are broadly categorized into two main types: thermosets and thermoplastics. The nature of the matrix dictates the applications of composites with polymeric matrices, with thermosets commonly used in structural materials and thermoplastics primarily employed in non-structural applications[61] .

1.7.1. Thermoplastics

These materials consist of long, linear, or branched macromolecules entwined with each other. When subjected to heat, intermolecular bonds can temporarily break, prompting a movement of molecules that strive to assume new positions. Upon cooling, the molecules solidify in their new positions, forming secondary bonds and establishing a new solid structure. The rigidity and strength of thermoplastics are closely tied to their high molecular weight and the intrinsic properties of the monomer units[11]. The thermo-reversibility and recyclability of thermoplastics are significant advantages. Key thermoplastic categories include polyvinyl chloride-based plastics, polyolefins like polyethylenes and polypropylenes, and polystyrenes and acrylics.

I.7. 2.Thermosetting

In contrast to thermoplastics, thermosets undergo irreversible hardening when heated. They cannot be reshaped or melted through heat and pressure. Chemically, molecules of a thermosetting polymer are linked by cross-links, forming a rigid three-dimensional network during composite formation. Compared to thermoplastic polymers, thermosets exhibit high chemical resistance and greater thermal stability. Additionally, they display increased resistance to relaxation and creep. The mechanical and thermal properties of thermosets depend on the molecular units creating the network, the length, and the density of the crosslinks [11].Commonly used matrices encompass unsaturated polyester, epoxy, and vinyl ester, providing a diverse range of chemicals and offering a wide array of mechanical and physical properties.

I.8.Optimization employing Response Surface Methodology (RSM) and Artificial Neural Networks (ANN)

The utilization of Response Surface Methodology (RSM) and Artificial Neural Networks (ANN) in modeling chemical processes holds significant importance due to its ability to establish meaningful connections between process variables, offering improved efficiency compared to traditional linear regression techniques. This becomes especially crucial when predicting complex processes, given the inherent uncertainties and intricacies involved in composites processing, characterized by numerous parameters and strong nonlinearity.

Response Surface Methodology relies on experimental designs to construct models that target optimal performance from a given set of parameters, as exemplified by the work of Igwegbe et

al.[62] . On the other hand, ANN, functioning as a soft-computational tool, makes biologically inspired decisions to address intricate engineering problems, as highlighted by Onu et al. [63].

Researchers have increasingly embraced both RSM and ANN to compare and predict various engineering processes. Instances include modeling lead adsorption from industrial sludge leachate on red mud (Geyikci et al.[64]), bio-coagulation-flocculation of municipal solid waste leachate using Picralima nitida extract (Igwegbe et al.[62]), extraction of antioxidants from Veronia cinerea leaves (Alara et al.[65]) and mild steel corrosion inhibition using Water Hyacinth as an inhibitor (Okewale et al.[66]).

Machine learning, particularly ANN, has found application in predicting the mechanical properties of engineering materials. Examples include evaluating self-consolidating concrete properties, residual flexural strength of fiber-reinforced concrete, cotton fibers properties, and polypropylene modified Marshall specimens in repeated creep tests, as conducted by Feng et al.[67], Congro et al.[68], Farooq et al.[69], and Tapkın et al.[70], respectively. These established prediction models not only guide performance design and predict changes in material properties in high-temperature environments but also contribute to reducing research and development costs. Additionally, they play a role in developing new failure criteria based on structural genomes and deep learning neural network models. Despite these advancements, there is currently a notable absence of reported literature on RSM/ANN modeling related to agro-waste modification for composite fabrication. Therefore, this study aims to fill this void by employing RSM and ANN techniques to model mechanical properties[71].

I.9. Numerical simulation in composite materials

I.9.1. Equations involving elements Fundamental Finite Element Method (FEM) Process and XFEM

The practical resolution of real-world challenges frequently involves the application of the finite element method (FEM) as a tool. Examples often hinge on packages, notably Abaqus, where computer programming is predominantly directed towards implementing material models and post-processing algorithms. A foundational understanding of the finite element method is crucial for proficiently utilizing any finite element software. Therefore, this chapter includes an introductory section designed to impart a formal understanding of the finite element method. Furthermore, it provides an overview of the Abaqus/CAE graphical user interface (GUI) to familiarize with typical procedures used in finite element modeling across various software platforms.For example, in tensile testing, consider the axial deformation of a rod, which is governed by an ordinary differential equation (ODE). This equation describes the rod's deformation in relation to its modulus (E), cross-sectional area (A), and the distributed force (f), with the weight function denoted as v. In the context of material modeling, it is standard to represent the actual rod mathematically as a line along the x-axis [72].

$$\int_{x_1}^{x_2}\left[-vf-\frac{d}{dx}\left(vEA\frac{du}{dx}\right)\right]dx=0 \quad \textbf{(I.4)}$$

This is referred to as a weak form because the solution u(x) is not required to satisfy the ODE (1) for every single value of x within the rod's length [0, L] in a strict sense. Instead, u(x) only needs to fulfill the ODE in (I.5) on an averaged basis, making it easier to find a weak solution compared to a strong one. Although the exact (strong) solution is known for the rod, most

problems in composite mechanics lack precise solutions. The governing equation is derived by integrating (2) through parts, as explained further.

$$-\left[vEA\frac{du}{dx} \right]_{x1}^{x2} - \int_{x1}^{x2} vf dx + \int_{x1}^{x2} EA\frac{du}{dx}\frac{dv}{dx} dx = 0 \quad \textbf{(I.5)}$$

In situations where v(x) is chosen as the weight function, typically equal to the primary variable u(x), insights drawn from the boundary term can be outlined as follows:

- Defining v(x) at either x_1 or x_2 is deemed an essential boundary condition.
- Specifying $EA\frac{du}{dx}$ at either end is characterized as the natural boundary condition
- While u(x) serves as the main variable, the secondary variable is $EA\frac{du}{dx} = A\sigma_x$ let.
- Then, the governing equation takes the form:

$$-\underbrace{\left(\underbrace{\left[vEA\frac{du}{dx} \right]^{x2}}_{Pv(x_2)} - \underbrace{\left[vEA\frac{du}{dx} \right]_{x1}}_{Pv(x_1)} + \int_{x1}^{x2} vf dx \right)}_{L(v)} + \underbrace{\int_{x1}^{x2} EA\frac{du}{dx}\frac{dv}{dx} dx}_{B(u,v)} = 0 \quad \textbf{(I.6)}$$

This expression can be denoted as either Equation(I. 7) or, expressed in matrix form, as Equation (I.8)

$$B(u,v) = L(v) \quad \textbf{(I.7)}$$

$$[K]\{u\} = \{F\} \quad \textbf{(I.8)}$$

In this context, where [73] denotes the nodal displacements, [K] represents the element stiffness matrix, and [74] is the element force vector, the relationship can be stated as:

$$[K] = EA\begin{bmatrix} \int_{x1}^{x2} \frac{dN_1}{dx}\frac{dN_1}{dx} & \int_{x1}^{x2} \frac{dN_1}{dx}\frac{dN_2}{dx} \\ \int_{x1}^{x2} \frac{dN_2}{dx}\frac{dN_1}{dx} & \int_{x1}^{x2} \frac{dN_2}{dx}\frac{dN_2}{dx} \end{bmatrix} \begin{Bmatrix} u_1 \\ u_2 \end{Bmatrix} = \begin{Bmatrix} \int_{x1}^{x2} fN_1 dx + P_1 \\ \int_{x1}^{x2} fN_2 dx + P_2 \end{Bmatrix}$$

(I.9)

I.9.2. Laws governing the behavior of a composite material

Generally, the constitutive equation governing a linear elastic solid is termed the generalized Hooke's Law. It establishes a connection between nine Cauchy stress components and nine deformation components, leading to a total of eighty-one constants[75, 76]. Equations (I.10) and (I.11) present the amalgamation of elasticity constants, where σ_{ji} denotes the stress component, ε_{kl} represents the strain components, G_{jikl} is the stiffness matrix, and S_{jikl} is the compliance matrix of the material. Notably, these matrices are inversely related, expressed as $[S]=[G]^{-1}$.

$$\sigma_{ji} = G_{jikl}\varepsilon_{kl} \qquad \textbf{(I.10)}$$

$$\varepsilon_{kl} = S_{jikl}\sigma_{ji} \qquad \textbf{(I.11)}$$

According to Bednarcyk, Aboudi, and Arnol[77], as well as Bauchau and Craig [78], the material constitutive laws are responsible for regulating physical phenomena such as heat conduction, diffusion, electric permittivity, magnetic permeability, and electric conductivity. These laws form mathematical representations that define the mechanical behavior of a material, comprising a set of idealizations derived from observed behavior[77].

I.9.3. Anisotropic Material

Due to the increasing importance of composite materials, a thorough understanding of the linearly elastic behavior of anisotropic materials is crucial. Anisotropic materials exhibit directional physical properties, wherein their material response is contingent upon the applied direction[78]. As explained by Soriano[79] and Daniel and Ishai [76], a linear anisotropic material is characterized by a matrix with independent elastic properties, adding complexity to the characterization process. In general, the stiffness matrix involves 36 independent coefficients, as per Equation (I.12). This reduction from 81 to 36 elastic constants is a result of the symmetry between σ_{ij} and σ_{ji}, as well as between ε_{gl} and ε_{lg} [80].

$$\begin{Bmatrix} \varepsilon_{11} \\ \varepsilon_{22} \\ \varepsilon_{33} \\ 2\varepsilon_{23} \\ 2\varepsilon_{13} \\ 2\varepsilon_{12} \end{Bmatrix} \begin{bmatrix} G_{11} & G_{12} & G_{13} & G_{14} & G_{15} & G_{16} \\ G_{21} & G_{22} & G_{23} & G_{24} & G_{25} & G_{26} \\ G_{31} & G_{32} & G_{33} & G_{34} & G_{35} & G_{36} \\ G_{41} & G_{42} & G_{43} & G_{44} & G_{45} & G_{46} \\ G_{51} & G_{52} & G_{53} & G_{54} & G_{55} & G_{56} \\ G_{61} & G_{62} & G_{63} & G_{64} & G_{65} & G_{66} \end{bmatrix} = \begin{Bmatrix} \sigma_{11} \\ \sigma_{22} \\ \sigma_{33} \\ \sigma_{23} \\ \sigma_{13} \\ \sigma_{12} \end{Bmatrix} \quad \textbf{(I.12)}$$

However, the demand for symmetry in anisotropic materials results in reducing the elastic components to 21, as expressed by the relation $G_{ij} = G_{ji}$ [75, 81] .Azevedo et al . [82] emphasized that the elastic properties essential for characterizing an anisotropic material can be conveyed through stress–strain ratios, with key coefficients including the longitudinal and transverse moduli of elasticity, as well as the Poisson's coefficient. Equation (I.13) presents the comprehensive mathematical representation of Hooke's law for anisotropic materials, where E represents the longitudinal elasticity modulus or Young's modulus, K signifies the transverse modulus of elasticity or shear modulus, ν denotes the Poisson's coefficient and ρ represents the angular/linear deformation.

$$\begin{Bmatrix} \varepsilon_{11} \\ \varepsilon_{22} \\ \varepsilon_{33} \\ 2\varepsilon_{23} \\ 2\varepsilon_{13} \\ 2\varepsilon_{12} \end{Bmatrix} = \begin{bmatrix} \frac{1}{E_1} & -\frac{\nu_{21}}{E_2} & -\frac{\nu_{31}}{E_3} & \frac{\rho_{2311}}{K_{23}} & \frac{\rho_{1311}}{K_{13}} & \frac{\rho_{1211}}{K_{12}} \\ -\frac{\nu_{21}}{E_1} & \frac{1}{E_2} & -\frac{\nu_{32}}{E_3} & \frac{\rho_{2322}}{K_{23}} & \frac{\rho_{1322}}{K_{13}} & \frac{\rho_{1222}}{K_{12}} \\ -\frac{\nu_{13}}{E_1} & -\frac{\nu_{23}}{E_2} & \frac{1}{E_3} & \frac{\rho_{2333}}{K_{23}} & \frac{\rho_{1333}}{K_{13}} & \frac{\rho_{1233}}{K_{12}} \\ \frac{\rho_{1123}}{E_1} & \frac{\rho_{2223}}{E_2} & \frac{\rho_{3323}}{E_3} & \frac{1}{K_{23}} & \frac{\rho_{1323}}{K_{13}} & \frac{\rho_{1223}}{K_{12}} \\ \frac{\rho_{1113}}{E_1} & \frac{\rho_{2213}}{E_2} & \frac{\rho_{3313}}{E_3} & \frac{\rho_{2313}}{K_{23}} & \frac{1}{K_{13}} & \frac{\rho_{1213}}{K_{12}} \\ \frac{\rho_{1112}}{E_1} & \frac{\rho_{2212}}{E_2} & \frac{\rho_{3312}}{E_3} & \frac{\rho_{2312}}{K_{23}} & \frac{\rho_{1312}}{K_{13}} & \frac{1}{K_{12}} \end{bmatrix} \begin{Bmatrix} \sigma_{11} \\ \sigma_{22} \\ \sigma_{33} \\ \sigma_{23} \\ \sigma_{13} \\ \sigma_{12} \end{Bmatrix} \quad \textbf{(I.13)}$$

The author stresses that in such situations, it is crucial to assume that failure is attributable to both normal and shear stresses, as failure might result from different sets of stresses acting on the element.

In the comparison of an orthotropic material with a generally isotropic theory, it becomes evident that the former incorporates three orthogonal symmetry planes—$x_1\ x_2$, $x_1\ x_3$ and x_2

x_3—leading to a reduction in the number of independent coefficients from 21 to [75, 76]. This reduction is justified by the following factors:

- Angular deformations are independent of normal stress.
- Linear deformations are independent of tangential stresses.
- Each tangential tension induces only angular deformation in the plane where it is exerted.

Equation (I.14) illustrates the generalized representation of Hooke's law for orthotropic materials, where E denotes the modulus of longitudinal elasticity or Young's modulus, K represents the cross modulus of elasticity or shear modulus, and ν indicates the Poisson coefficient [82].

$$\begin{Bmatrix} \varepsilon_{11} \\ \varepsilon_{22} \\ \varepsilon_{33} \\ 2\varepsilon_{23} \\ 2\varepsilon_{13} \\ 2\varepsilon_{12} \end{Bmatrix} = \begin{bmatrix} \frac{1}{E_1} & -\frac{\nu_{21}}{E_2} & -\frac{\nu_{31}}{E_3} & 0 & 0 & 0 \\ -\frac{\nu_{12}}{E_1} & \frac{1}{E_2} & -\frac{\nu_{32}}{E_3} & 0 & 0 & 0 \\ -\frac{\nu_{13}}{E_1} & -\frac{\nu_{23}}{E_2} & \frac{1}{E_3} & 0 & 0 & 0 \\ 0 & 0 & 0 & \frac{1}{K_{23}} & 0 & 0 \\ 0 & 0 & 0 & 0 & \frac{1}{K_{13}} & 0 \\ 0 & 0 & 0 & 0 & 0 & \frac{1}{K_{12}} \end{bmatrix} \begin{Bmatrix} \sigma_{11} \\ \sigma_{22} \\ \sigma_{33} \\ \sigma_{23} \\ \sigma_{13} \\ \sigma_{12} \end{Bmatrix} \quad \textbf{(I.14)}$$

When examining a composite reinforced with unidirectional fibers, it is automatically designated as an anisotropic material due to the lack of symmetry between planes. Analyzing the thickness further reveals its significantly smaller size compared to other plane dimensions. Consequently, many researchers consider unidirectional laminates as orthotropic materials,

accounting for the plane stress state based on the assumptions outlined in Equation (I.15)[75]

.

$$\sigma_3 = \tau_{23} = \tau_{31} = 0 \quad \textbf{(I.15)}$$

I.9.4. Transverse Isotropic Material

$$\begin{Bmatrix} \varepsilon_{11} \\ \varepsilon_{22} \\ \varepsilon_{33} \\ 2\varepsilon_{23} \\ 2\varepsilon_{13} \\ 2\varepsilon_{12} \end{Bmatrix} = \begin{bmatrix} \frac{1}{E_1} & -\frac{\nu_{21}}{E_2} & -\frac{\nu_{31}}{E_1} & 0 & 0 & 0 \\ -\frac{\nu_{12}}{E_1} & \frac{1}{E_2} & -\frac{\nu_{12}}{E_1} & 0 & 0 & 0 \\ -\frac{\nu_{13}}{E_1} & -\frac{\nu_{21}}{E_2} & \frac{1}{E_1} & 0 & 0 & 0 \\ 0 & 0 & 0 & \frac{1}{K_{12}} & 0 & 0 \\ 0 & 0 & 0 & 0 & \frac{1}{K_{13}} & 0 \\ 0 & 0 & 0 & 0 & 0 & \frac{1}{K_{12}} \end{bmatrix} \begin{Bmatrix} \sigma_{11} \\ \sigma_{22} \\ \sigma_{33} \\ \sigma_{23} \\ \sigma_{13} \\ \sigma_{12} \end{Bmatrix} \quad \textbf{(I.16)}$$

A material categorized as transversely isotropic can be chanaracterized as an orthotropic material displaying isotropy within one of its planes of symmetry, indicating consistent properties in all directions within that specific plane [80].

In comparing transversely isotropic material with a more general orthotropic material, it becomes evident that in transversely isotropic materials, there is symmetry between the planes x_1 x_3 and x_1 x_2, resulting in a reduction from nine to five independent coefficients. Azevedo et al[82] . Further notes specific considerations for transversely isotropic materials:

- Equality in linear deformations in the plane x_2 x_3 caused by the normal stress σ_{11}.
- Equality in linear deformations ε_{22} and ε_{33} caused by the normal stress σ_{22} to the deformations ε_{33} and ε_{22}, respectively, induced by tension $\sigma_{22} = \sigma_{33}$.
- Each tangential tension induces only angular deformation in the plane in which it operates.
- The angular strain γ_{23} caused by stress σ_{23} is equivalent to the angular strain γ_{13} caused by stress $\sigma_{13} = \sigma_{23}$.

Equation (7) provides the generalized representation of Hooke's law for transversely isotropic material, where E denotes the modulus of longitudinal elasticity or Young's modulus, K represents the transverse modulus of elasticity or shear modulus, and ν signifies the Poisson coefficient [80].

Minimum strain energy density criteria, [Sih1974] for method XFEM

Strain energy function

$$
\begin{aligned}
a_{11} &= \frac{\kappa+1}{16\mu\lambda\kappa^2 cos\theta}\left[2(1-2\nu)+\frac{\kappa-1}{\kappa}\right] \\
a_{12} &= \frac{(\kappa^2-1)^{1/2}}{8\mu\lambda\kappa^2 cos\theta}\left[\frac{1}{\kappa}-(1-2\nu)\right] \\
a_{22} &= \frac{1}{16\mu\lambda\kappa^2 cos\theta}\left[4(1-\nu)(\kappa-1)+\frac{1}{\kappa}(\kappa+1)(3-\kappa)\right] \\
a_{12} &= \frac{1}{4\mu\lambda\kappa cos\theta}
\end{aligned}
$$

$$
S = a_{11}K_I^2 + 2a_{12}K_IK_{II} + a_{22}K_{II}^2 + a_{33}K_{III}^2
$$

Assumptions 1) Crack initiates when the minimum S reaches to some critical value

2) Crack extends in a direction which strain energy density factor possess a minimum

I.10. Conclusion

From the review of relevant literature on natural fibers, with a specific focus on those sourced from plants (vegetables) and biocomposites, the key conclusions that can be drawn are:

Expansion: Cellulose is present in all plant fibers; however, the quantity varies depending on the specific type of fiber. Natural fibers demonstrate remarkable sensitivity to humidity, experiencing swift impacts from their environment. Generally, an increase in moisture content tends to diminish the mechanical properties of these fibers.

The interaction between the matrix and fibers significantly influences the mechanical properties of composite materials. Despite studies demonstrating that plant fibers possess mechanical qualities comparable to traditionally used glass fibers, the resulting composite materials still exhibit inferior characteristics. Consequently, numerous investigations have concentrated on enhancing these properties, particularly through the physical or chemical treatment of fibers.

For a more comprehensive characterization and understanding of our natural fiber reinforcement, a specific chapter thoroughly examines the structure, morphology, chemical composition, mechanical and physical characteristics, as well as the textile formatting of the vegetable fibers.

The second part of our work is dedicated to statistical studies employing the ANN and RSM methods, along with coefficients and analysis of variance. This is done to estimate the mechanical properties, specifically stress, strain at break, and Young's modulus of plant fibers. Additionally, we assess the impact of explanatory factors (independent variables) based on the input parameters.

CHAPTER II:

Methods and Experimental Procedures

II.1. Introduction

In this chapter, the focus was on the technique of extracting and preparing fibers from palm fronds, diss, sisal, luffa, and jute. Additionally, silicone molds were created for honeycomb samples, tensile samples, and bending samples. Bio-composites were manufactured through molding, incorporating additional fibers like reinforcing fibers, and using polyester resin as an epoxy matrix.

The chemical and mechanical characterization of the bio-composites were conducted using various well-known machines and devices. These included the Fourier transform infrared machine (FTIR), tensile, bending, and compression machines for assessing mechanical properties, as well as cyclic fatigue testing. It is crucial to highlight that a variety of devices were employed for drying both fibers and biocomposite samples. Furthermore, the chapter presents a detailed overview of the different experimental techniques and conditions used in Part 3.

II.2. Materials

II.2.1. Epoxy resins

Are thermosetting compounds that undergo curing reactions using a diverse range of curing agents. The characteristics of these resins are contingent upon the specific combination of epoxy types and curing agents employed[83-86].Due to their exceptional mechanical properties, strong adhesion to various substrates, and resistance to heat and chemicals, epoxy resins are extensively employed in diverse fields. They serve as fiber-reinforced materials, versatile adhesives, high-performance coatings, and encapsulation materials [87-89] in this work, epoxy was used, with an Algerian company based in the Bouira region fabricating LORN Chemicals' epoxy. The chemical formula for epoxy is $C_3H_{13}N_3$.

II.2.2. Polyester resins:

In this research, a resin known as commercial unsaturated polyester (UP) ISO is employed for stratification. Unsaturated polyester resins are favored in the realm of thermosetting systems due to their cost-effectiveness and their ability to be molded into large composite structures. The most commonly used reinforcement in this system is furnished by sized glass fibers available in a variety of orientations, shapes, and densities as fabric materials. More recently, there has been a growing interest in exploring the feasibility of incorporating plant-based fibers as reinforcements in composite materials, as evidenced by recent studies [90, 91].

II.2.3. Fibers

In this study, five types of natural fibers were utilized: palm fibers, sisal, diss, luffa, and jute. These fibers are depicted **in Figure II.10, 13and 15** it's noteworthy to mention that sisal, luffa, and jute fibers were procured directly from the local market, whereas date palm fibers and diss fibers were extracted from the date palm tree and the diss plant, respectively. These plants are among the most prominent species found in the M'sila region, located in the heart of Algeria [13].

II.2.3.1 Extraction and preparation of fibers used

II.2.3.1.1. Diss fibers Extraction:

The Diss plants were soaked in a hot water drum for one hour to separate the fibers from the plant's blade. The extraction process was conducted at a room temperature of approximately 25°C. Subsequently, manual extraction took place, involving the use of a blunt knife to crush the plant material, remove the outer shell, and free the fibers. After these steps were completed, the fibers were dried, cut into 1mm sections, and stored in plastic containers.as shows as **figure.II.14.**

II.2.3.1.2. Date palm fibers Extraction:

Originating from the fronds of date palm clusters in Algeria's M'sila region, these fibers were obtained through a manual extraction process. Subsequently, they were cleaned to remove impurities using a wire brush and cut into small pieces.

II.2.3.1.3.Processing and Treatment of Date Palm Fibers

The palm fibers were subsequently treated with a solution containing 10% (w/v) sodium bicarbonate ($NaHCO_3$), a method previously utilized by other researchers[92, 93] . Initially, we stirred the solution ten times after adding the fibers, with each stirring session lasting between 3 to 30 minutes, until achieving complete homogeneity. The fibers were withdrawn at different time intervals (24 and 96 hours), and then rinsed under running water to halt the reaction. Following this, they were air-dried for a day and subsequently underwent a 5-hour drying process at 50°C in a vacuum oven. **As figure II.12.**

II.3. Process for manufacturing silicone molds

In this research, the production of samples was accomplished through molding using silicone molds as follows:

II.3.1. Molds of the Honeycomb

To produce the molds for specimen casting, initial steps involved the generation of parts for 3D test structures within computer-aided design CATIA (CAD) software. These structures, shaped as either Honeycomb, Star-Fish and RE-entrant, as shown in **Figure II.1.**Were meticulously crafted based on dimensions derived from previous literature. Following the design phase, the resultant samples were saved in STL format and subsequently processed in a file. This file underwent conversion to G-code through the utilization of a 3D cutting simplification program Ultimaker cura, facilitating the subsequent printing of the molds.

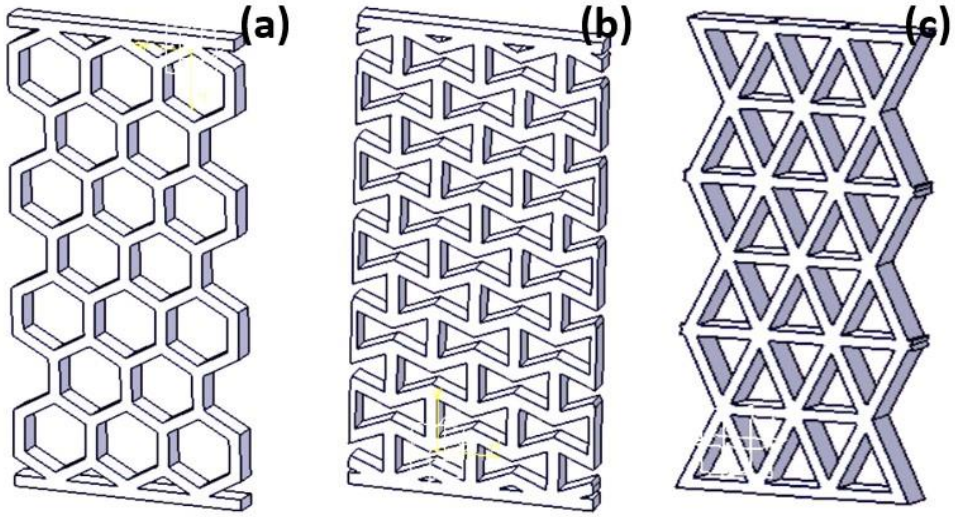

Figure II.1: Structures in CATIA: (a) Honeycomb, (b) RE-entrant and (c) Star-Fish

The construction of beehive structures, incorporating designs like honeycomb and Star-Fish, RE-entrant was carried out through the utilization of a 3D printer as shows in **Figure II.2.** 3D printing (3DP), recognized as a rapid prototyping (RP) technique rooted in computer-aided 3D modeling [94], stands out for its ability to initiate an efficient design process, contributing to the success of end products [95]. It plays a pivotal role in material savings during the production phase [96]. Acknowledged for its transformative potential across various industries[97], 3DP has gained popularity due to its capacity to reduce both time and material consumption in manufacturing processes [98]. RP, functional part production, and free-form production all stand to benefit from advancements in 3DP technology[99]. Among 3DP technologies, Fused Deposition Modeling (FDM) has become commercially prevalent [100]. Illustrated in **Figure II.3**, the FDM process involves the layer-by-layer addition of plastic filament material[101, 102]. In our study, we utilized polylactic acid (PLA) filaments, chosen for their simplicity in use within FDM-based 3D printers[103]. PLA was selected for its common use in recycling practices compared to other filament types, as well as its status as a biodegradable thermoplastic

polyester derived from cleaner sources. It possesses lower hazardous components and 3DP temperatures, contributing to energy conservation[104]. The characteristics of the PLA used are detailed in **Table II.1,** while **Table II.2** provides information on the parameters and features of the 3D printer (2A2N) employed in the study (Laboratories' Constantine).

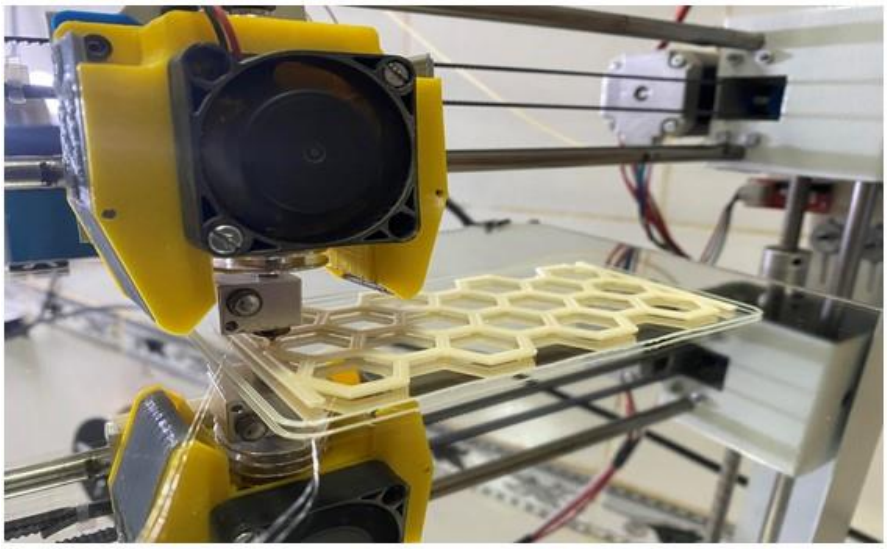

Figure II.2: Three-dimensional printer used for our work

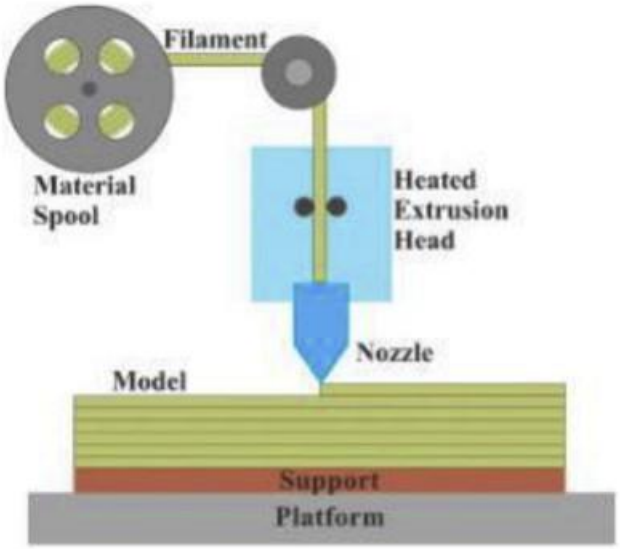

Figure II.3: Schematic illustration of FDM method[105]

Table Ⅱ.1: Properties of filament materials and test results

Properties	Values
Material	PLA.
Filament Colour	Beige
Diameter of Filament (mm)	1.75
Temperature of Bed (C°)	60-75
Extruding Temperature of PLA (C)	200-220
Tensile Strength of PLA (MPa)	56

Table Ⅱ.2: FDM system parameters and properties.

Properties	Values
Printing Method	**Fused Deposition Modeling (FDM)**
Printing Size (mm)	**220 × 220 x 250**
Machine Size (mm)	**440 ×410 x 465**
Filament Diameter (mm)	**1.75**
Filament Type	**LPA**
Diameter of Nozzle (mm)	**0.4**
Tolerance (mm)	**±0.1**
Temperature of Nozzle (C)	**200**
Temperature of Bed (C)	**60**
Printing speed (mm/min)	**50**
Model	**ANYCUBIC**
Slicer Program	**Ultimaker cura**
CAD Program	**CATIA**

Figure II.4: Position the printed samples securely within a wooden mold

The process of preparing the silicone material for this research involves two key components: the transparent hardener (Part A) and the white silicone (Part B), both integral for initiating the curing reaction. To ensure precise die types with minimal discrepancies, the following steps were meticulously followed for each die:

- Part A and Part B were accurately measured and poured into a designated measuring cup, adhering to the specified proportions for the chosen durometer. For example, in a specific ratio, such as 2 grams of Part A for every 20 grams of Part B, precise measurements were maintained. After pouring, both components were thoroughly mixed by stirring with a plastic spoon for two minutes.
- To prevent the entrapment of air and air bubbles within the mold, it is recommended to stir the mixture with a spoon, moving from the bottom to the top. This stirring technique

aids in achieving a homogenous mixture, reducing the likelihood of undesirable air pockets in the silicone material. The stages are in **Figure II.6.**

Figure II.5: Equipment used for vacuum degassing of the silicone before pouring into the cast

After the 3D-printed honeycomb samples (honeycomb, Stra-Fish-RE-entrant) were prepared on a 3D printer, they were carefully placed within a wooden mold and securely fixed to prevent any movement during the silicone pouring process ,as shows **Figure II.4.** Subsequently, the stage of pouring liquid silicone into the wooden mold, housing the beehive samples, ensued. To ensure a level surface for the mold containing the 3D-printed samples, a level tool was employed. The liquid silicone was then poured slowly into the mold until the samples submerged by 3 mm. At this point, the pouring of silicone liquid ceased. as depicted in **Figure II.6.**To mitigate the risk of air and bubbles getting trapped in the mold, it is advisable to expel the gas using a hairdryer, elevating any trapped bubbles within the mold.

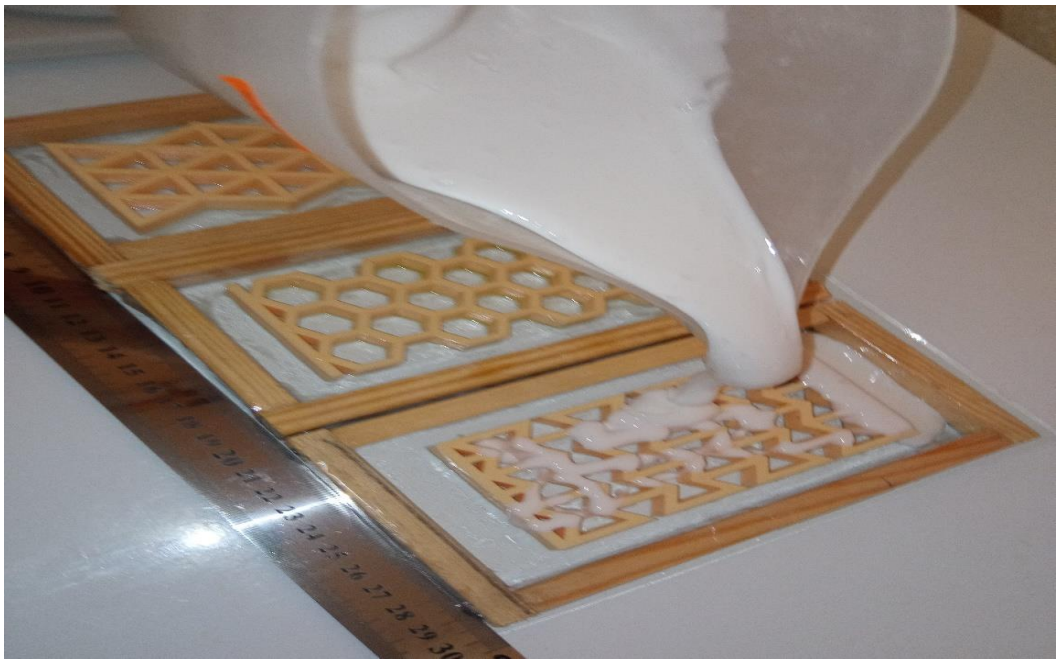

Figure II.6: Pouring the liquid silicone into the cast

After pouring the silicone into the mold and ensuring the release of any trapped air bubbles, the mold is left at room temperature for 24 hours to allow the silicone to crystallize with the hardener. After this period, the printed samples (such as honeycomb and Stra-Fish-RE-entrant) are extracted from the silicone mold using a 3D printer, making the mold ready for use as shows in **Figure II.7.**

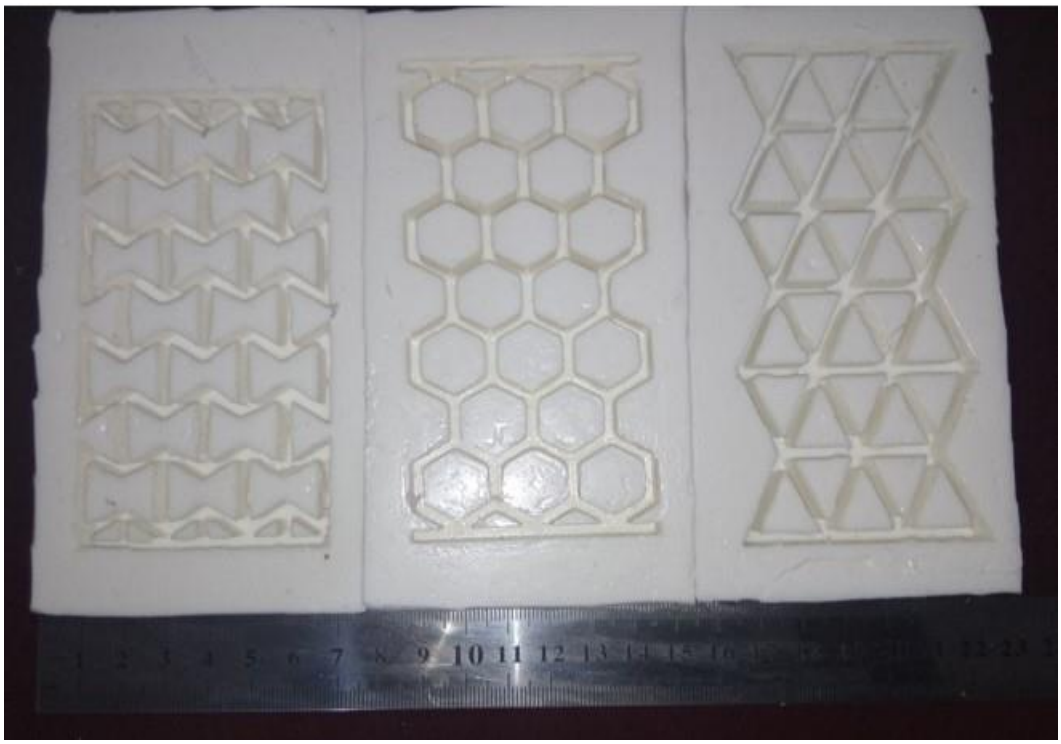

Figure II.7: Final shape of the mold after curing

II.3.2. Tensile specimen mold

To obtain a template for molding tensile samples following ASTM D638-03 specifications, one sample was designed with dimensions of 165 × 19 × 7 mm^3 using CATIA. Subsequently, five tensile samples were 3D printed using PLA filament after saving them in an STP document. After the printing stage, the samples were placed in a wooden mold and securely fixed to prevent any movement during the pouring of the silicone mixture, which included a hardener. Two percent of hardener was added for every 20% of silicone. The mixture was thoroughly shaken to ensure even distribution within the mold, using a plastic spoon for this purpose. The mold was then left to dry for 24 hours at room temperature. Afterward, the 3D printed samples were removed from the 3D printer to finally obtain a silicone mold for molding the tensile samples, as shown in **Figure II.8**.

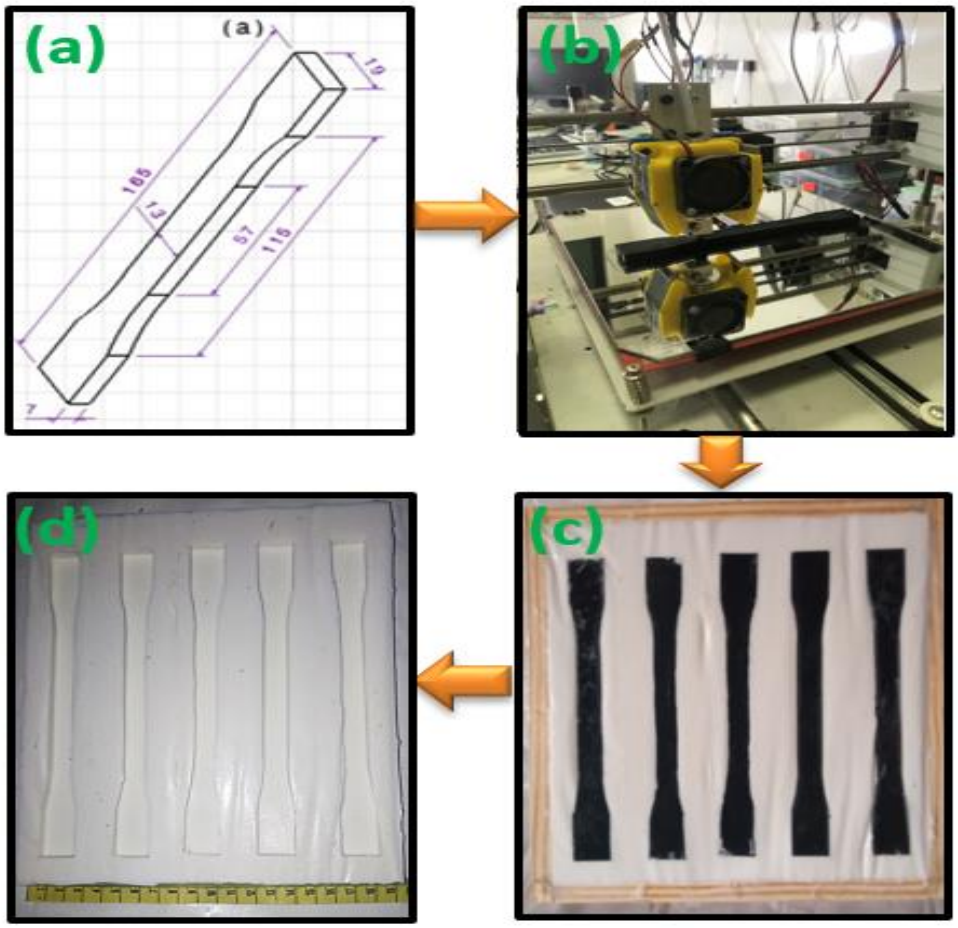

Figure II.8: Process flow of making a silicone mold tool:(a) sampling design in CATIA,(b): printing samples in a 3DP, (c):Silicone molding and casting process and (d): silicone mold for samples

II.3.3. Mold of specimen to manufacture bending

Samples according to ASTM D 790 standard, five wooden pieces with dimensions of 150 x 12.7 x 10 mm^3 were crafted in the carpentry workshop. These wooden pieces were then placed in a wooden mold, ensuring a secure fit to prevent any movement when casting silicone. Prior to pouring the silicone, the silicone was mixed thoroughly with the hardener using a plastic spoon. After pouring the silicone-hardener mixture into the mold, it was left to dry for 24 hours at room temperature. Finally, the silicone mold was obtained by separating it from the wooden samples, as depicted in **Figure II.9.**

Figure II.9: Process flow of making a silicone mold tool

II.4. Samples preparation

II.4.1. Honeycomb samples.

Bio-composites of honeycomb samples (hexagonal, RE-entrant, and starfish) were manufactured using a molding process in pre-made silicone molds, following the outlined steps:

1. **Fiber Preparation:** Palm, jute, and luffa fibers were obtained and cut into small 1 mm pieces. The fiber content was set at 20% for each type, in accordance with prior research [106].
2. **Mixing:** The cut fibers were combined with epoxy resin at a ratio of 3.75 grams of resin to 1.25 grams of hardener. The mixture was thoroughly mixed with a plastic spoon to ensure homogeneity.
3. **Molding:** The homogeneous mixture was then poured into silicone molds, creating pressure specimens corresponding to the hexagonal, RE-entrant, and starfish designs.
4. **Drying:** The specimens were allowed to dry for 24 hours at room temperature.
5. **Electrophoresis:** Subsequently, the specimens were transferred to an electrophoresis oven to facilitate the crystallization of the resin. The temperature was maintained at 60°C for 5 hours.

The entire process is illustrated in **Figures II.10, 11,** and **12**.

Figure II.10: The fibers used for the honeycomb samples.

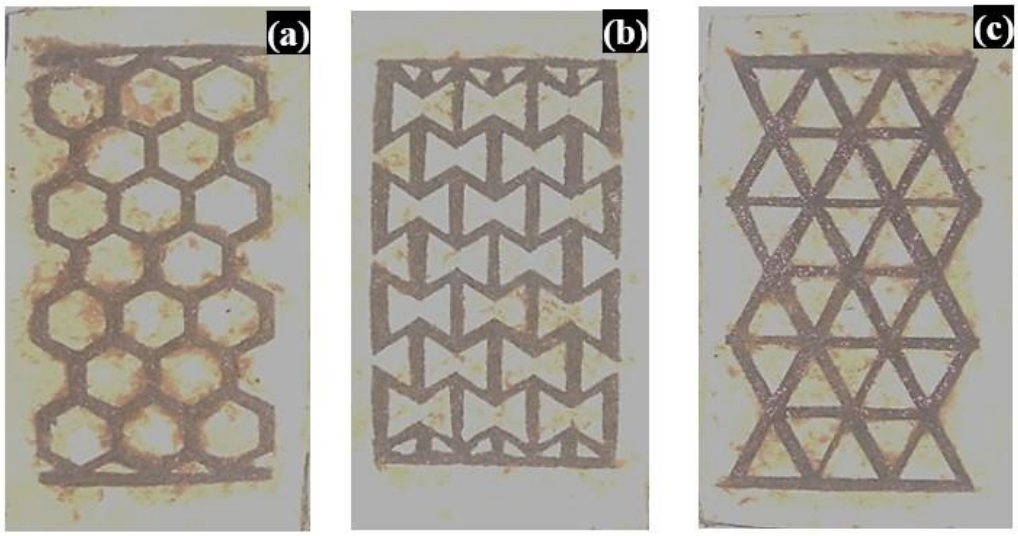

Figure II.11: Molding bio composite samples in a silicone mold :(a) hexagonal,(b) re-entrant and (c) star-fish

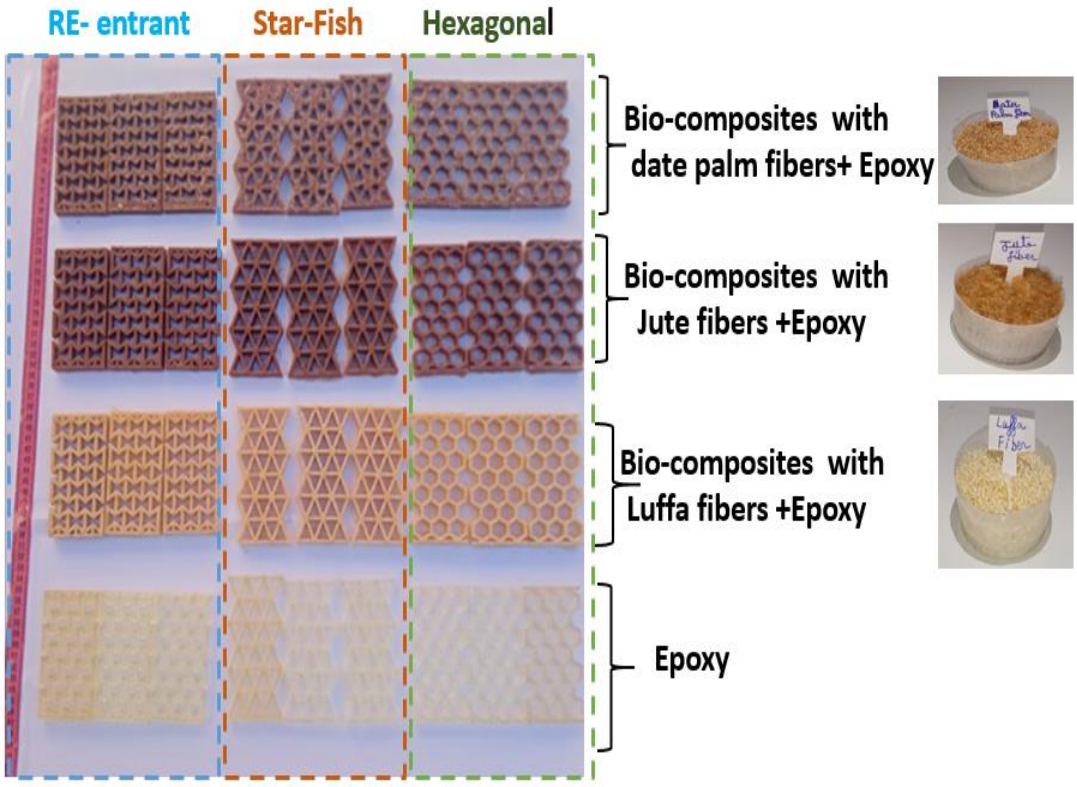

Figure II.12: Honeycomb samples of bio composites

II.4.2. Tensile specimen for bio composite (Epoxy/Palm)

After obtaining palm fibers extracted from the arm of the date palm tree cluster, the subsequent stage involves manual extraction, followed by shearing. During the shearing stage, the fibers are cut into short pieces approximately 1 mm long. The fibers then undergo a curing phase, involving immersion in a 10% (w/v) solution of sodium carbonate ($NaHCO_3$) for durations ranging from 24 to 96 hours. Following the curing phase, biocomposites are formed, comprising a mixture of fibers and epoxy, with fiber percentages of 15%, 20%, 25% and 30%. This process is applied to both treated and untreated fibers. Next is the molding stage, where the fibers are placed in a silicone mold prepared previously to create tensile samples, as depicted in **Figure II. 13**. The samples are left to dry for 24 hours at room

temperature, after which they are transferred to an electric oven to ensure resin crystallization, maintaining a temperature of 60°C for 5 hours.

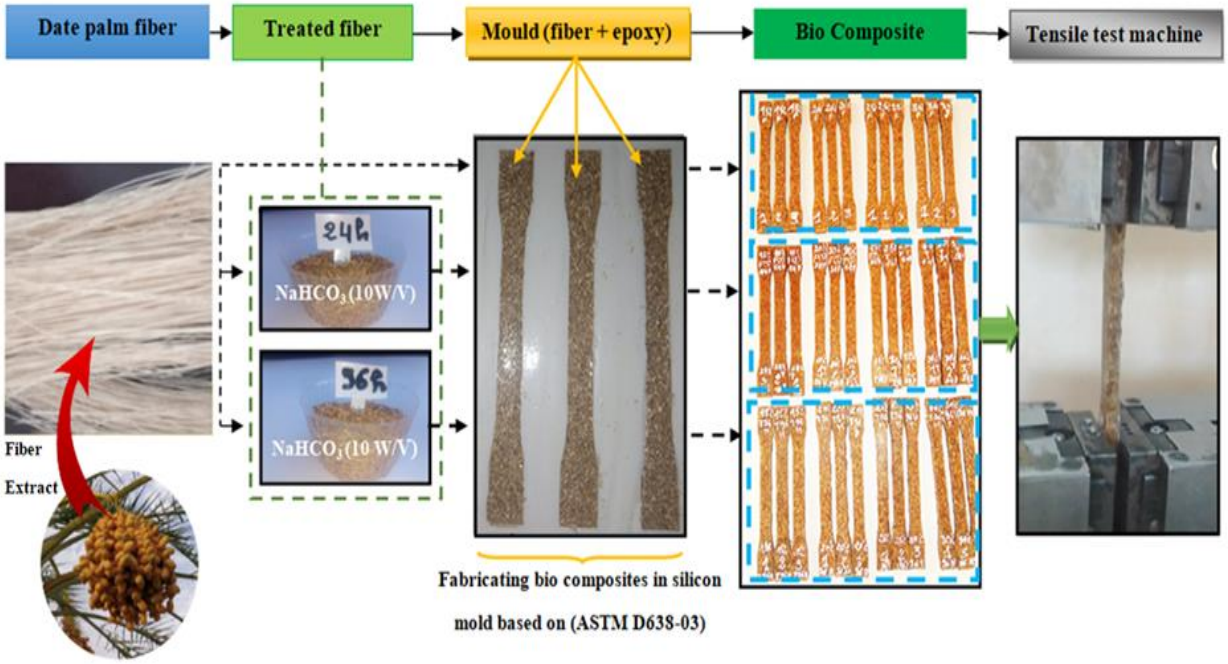

Figure II.13: Process for developing and characterizing tensile specimens

II.4.3. Tensile specimen of epoxy

In our study, we employed three distinct epoxy engineering designs (Undamaged Specimen, Specimen with Hole, and Specimen with Elliptical Notch) in accordance with ASTM D638-14, featuring consistent dimensions of 165 × 12 mm² and a thickness of 7 mm. Each design comprised five samples. The resin, mixed with a hardener in a ratio of 65% by weight to 35% by weight, was then poured into a pre-prepared silicone mold.

Subsequently, the samples were left to dry within the mold for 24 hours and underwent a heat treatment at 70°C for 5 hours, resulting in a total of 15 samples. Following the heat treatment, five samples remained unchanged, five were drilled with a 6 mm diameter, and the last five were drilled with an

oval hole measuring 6 by 3 mm. These dimensions align with those commonly used by researchers, as evidenced by references [107, 108] . The sample casting process is depicted in **Figure II.14**

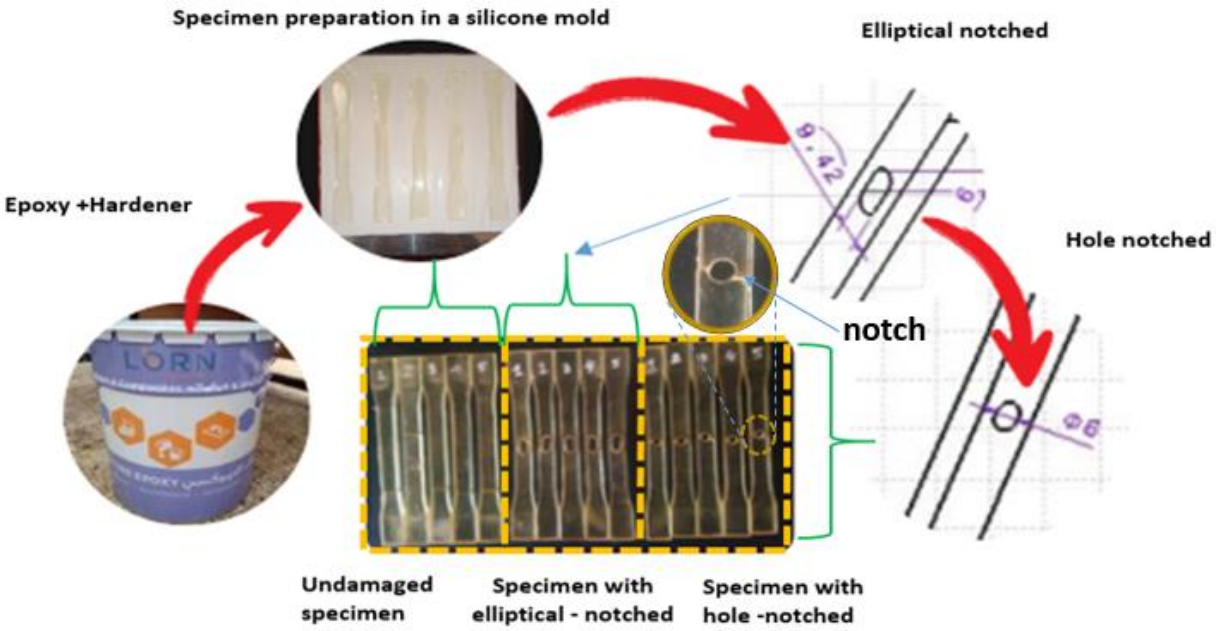

Figure II.14: Epoxy samples preparation steps

.

II.4.4. Bending specimens

In our research, we employed loofah, sisal, and desse fibers. The manual extraction of fibers included acquiring loofah and sisal from local markets. Moving on to the cutting stage, the fibers were meticulously cut into small pieces measuring around 1 mm, and these were then stored in plastic containers. Bending models were specifically crafted for each fiber type: Luffa-Polymer, Sisal-Polymer, and Disp-Polymer. Each model incorporated varying fiber percentages (10%, 15%, 25%), with the fibers seamlessly integrated into the polymer. Prior to pouring the mixture into a silicone mold prepared in advance—a method endorsed by previous researchers [109]

—the components were thoroughly stirred.

Following this, the samples were left undisturbed for 24 hours for the drying process and subsequently exposed to room conditions for a week to ensure effective crystallization of the resin. Post-crystallization, the bending specimens underwent a curing phase lasting 5 hours in an oven set at 60 °C. After this thermal treatment, a bending test was conducted. The entire sequence of sample preparation steps is visually presented in **Figure II.15**

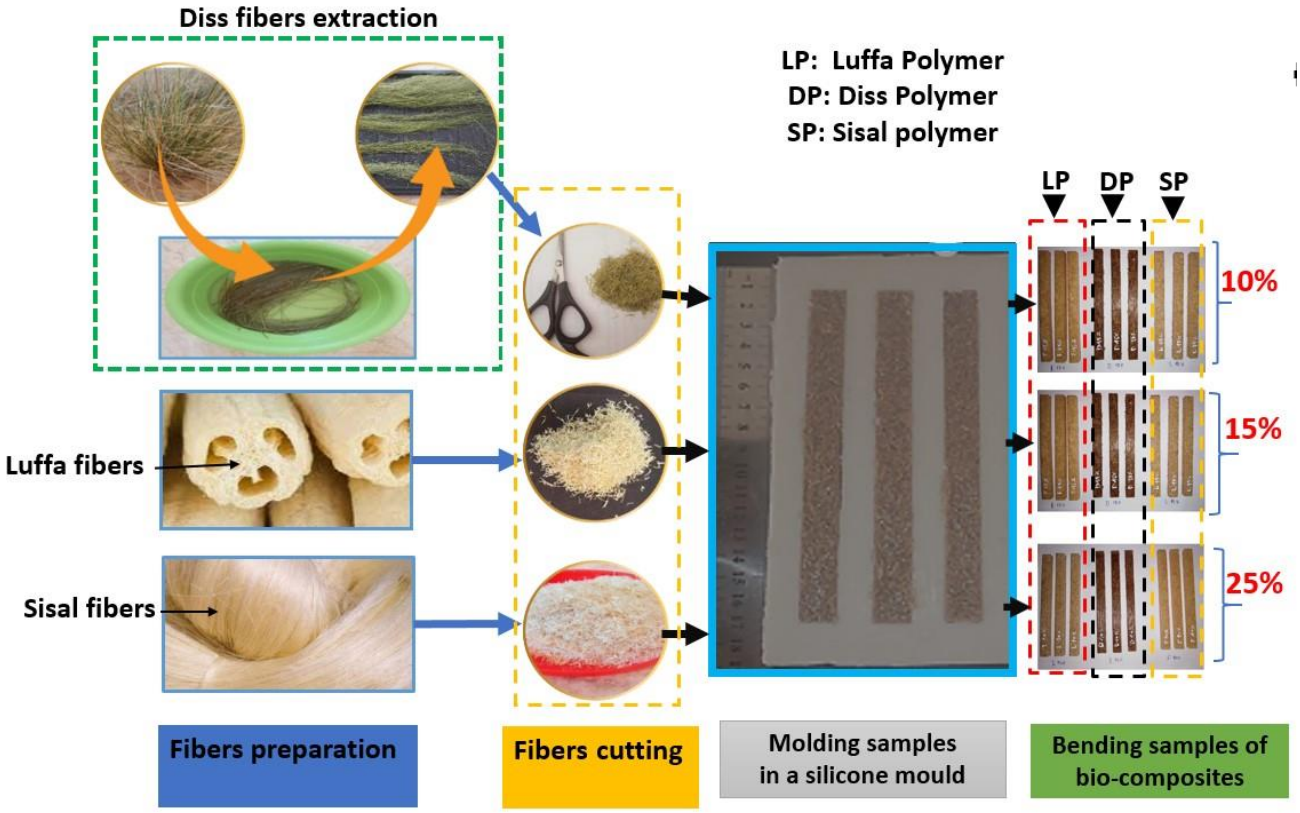

Figure II.15: Process for developing and characterizing bending specimens

II.5. Water absorption

The assessment of water absorption in Diss/Sisal/Luffa composites adhered to the ASTM 5229[110].protocols for all samples. These composites were immersed in distilled water at room

temperature for a duration of 44 days. Prior to testing, a pre-conditioning step in an oven at 50-60°C for 5 hours was conducted to eliminate residual moisture from the composites. Subsequently, the 27 specimens underwent precise weighing using a precision balance with an accuracy of 1/1000 g and were then placed in 40 ml of distilled water.

Following the initial weighing and at 24-hour intervals thereafter, the composite specimens were removed from the water bath. Their surfaces were delicately dried with tissue paper, and the specimens were reweighed to determine the absorbed water amount. This weighing process continued until the water absorption percentage reached saturation. In our study, all composites reached saturation after 44 days of immersion, with no further increase in the water absorption percentage beyond this period. Hence, our analysis is centered on the water absorption percentage over the 44-day period, equivalent to 1056 hours, as illustrated in **Figure II.16**. The percentage of water absorption is calculated using the following formula (Eq. II.1 [111, 112]).

$$Water\_absorption(\%) = ((W - W_0)/W_0) \times 100 \qquad \text{(II.1)}$$

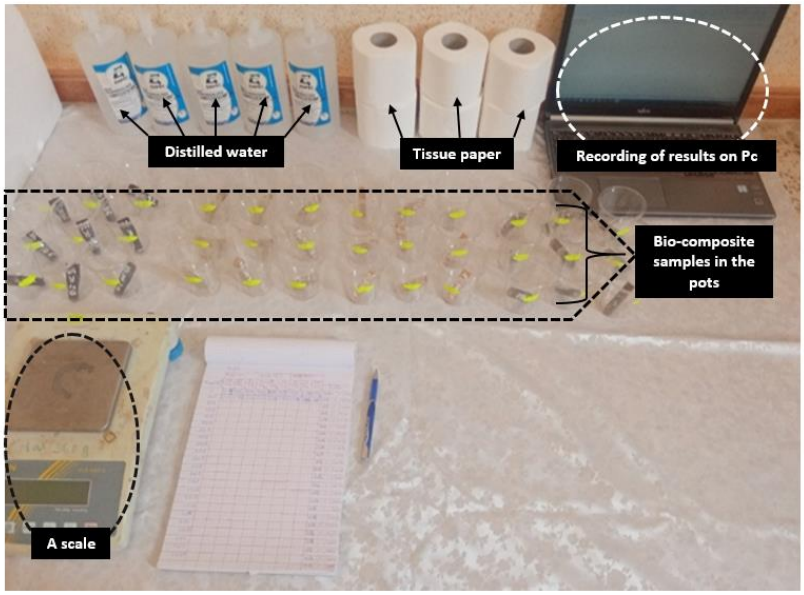

Figure II.16: Water absorption tests by samples of bio-composites for samples of bending

II.6. Tools Used in the Experiments

II.6.1. Digitally oven

Before to conducting mechanical tests, including traction and 3-point bending, the prepared specimens were subjected to a 5-hour heat treatment in an oven at 60°C to ensure the thorough polymerization of the samples [113, 114].

II.6.2. Struers Dry box-2 (samples dryer)

Struers Dry Box-2 is employed to dry the samples for an hour before the absorption of distilled water, a crucial step to promote proper crystallization and prevent the formation of dew drops on the samples. This process was carried out in the laboratories of M'sila, Algeria, as illustrated in **Figure II.17.** Struers Dry Box-2 is a cold drying apparatus that generates a powerful airflow, adjustable in temperature from 40°C to 90°C. It is also effective in reducing the processing time required for cooling-based applications, as it helps maintain a consistent temperature within the processing medium

Figure II.17: Struers Dry Box-2

II.6.3. The Infrared Spectrometer

Infrared spectrometry is a technique that enables the identification of a product's chemical composition by detecting specific absorption bands present in its spectrum. Each absorption band corresponds to the vibration mode of a chemical bond between two atoms, providing valuable insights into the molecular structure of the compound. In our study, we utilized a spectrometer from Agilent Technologies, located at the University of Msila in Algeria, as shown **in Figure II.18.** This spectrometer came equipped with its dedicated quantitative analysis software. The fiber samples collected from the [provide specific source or location] were analyzed using this instrument, with a scanning speed of 32 acquisitions ranging from 500 to 4000 cm^{-1} and a resolution of 2 cm^{-1}.

Figure II.18: The Infrared Spectrometer Series

II.6.4. Tensile tests

After preparing epoxy samples, including an undamaged specimen, a specimen with a hole-notch, and a specimen with an elliptical notch, along with specimens for tensile testing of biocomposites conforming to ASTM D638-14, with dimensions of 165×19×7 mm³ as depicted **in Figure II.19-a**, the tensile test was conducted at the laboratory of the University of Boumerdes in Algeria. In this process, both ends of the samples were affixed to a length of 25 mm each on a traction clamp to enhance grip and prevent slippage, while the transmission speed control rate was set to 1 mm/min for samples of epoxy and 2mm/min for samples of bio composite. The samples were stretched until failure, as illustrated **in Figure II.19-b**, to obtain tensile results, including the stress-strain curve and Young's Modulus.

The values of force and displacement of the crosspiece facilitate the estimation of stresses at break, strains, and Young's modulus, utilizing the relationships provided by RDM (equations II.2, II.3, and II.4), in accordance with the ASTM standard.

$$\sigma = \frac{F}{s} \qquad \text{(II.2)}$$

$$\varepsilon = \frac{\Delta l}{l_0} \qquad \text{(II.3)}$$

$$E = \frac{\sigma}{\varepsilon} \qquad \text{(II.4)}$$

Where:F: the force at (N); S: section in (mm^2); Δl : the value obtained by the machine in (mm);

l_0: the initial length (mm); σ: the breaking stress in (MPa); Ɛ: Stress in (%); E: Young's modulus in (GPa)

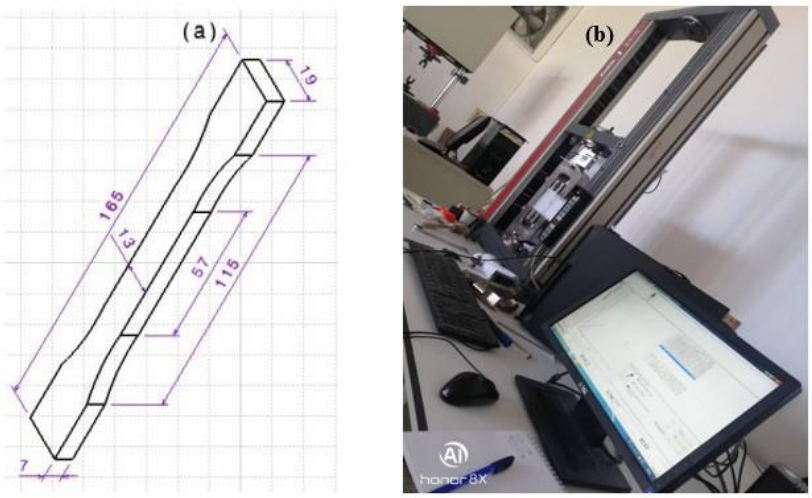

Figure II.19: Tensile test: (a) specimen of tensile and (b) Machine of tensile test (lab of Boumerdes)

II.6.5. Bending tests

A Universal (YL) testing machine was utilized in our work, conducting tests at a speed of 2.5 mm/min with three samples each for fiber contents of 10%, 15%, and 25% for Diss, Sisal, and Luffa. The machine, equipped with a 25kN load cell, subjected each sample to a bending test at three points, as shows **Figure II. 20-b.** Moreover, accurately prepared samples measuring 100 x 20 x 6 mm³ were tested in accordance with the ASTM D7264 standard, specifically designed for fiber-strengthened plastic compounds, as shown in **Figure II.20-a.**Using the Winkler formula [115], as follows:

$$\sigma = \frac{FD}{2E_s(h+E_a)b}(MPa) \qquad (\text{II.5})$$

Where: F: Breaking load of the soles, measured in (N), for the three-point bending test, D: Distance between supports during the three-point bending test, expressed in (mm), E_s: Thickness of the soles, measured in (mm).

h: Total thickness of the sandwich structure, expressed in (mm),E_a: Thickness of the core within the sandwich structure, measured in (mm).b: Width of the test samples, expressed in (mm).

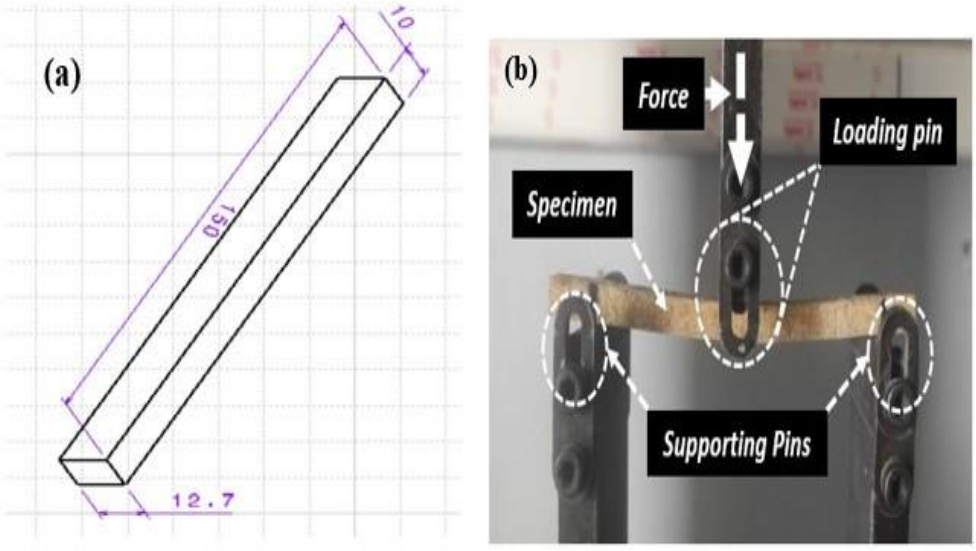

Figure II.20: Bending test: (a) specimen of bending, (b) machine of bending test (lab of Maghreb Pipe)

II.6.6. Compression test for samples hexagonal

Numerous artificial honeycombs are available, and in this study, we focused on three specific types of honeycomb structures (Hexagonal, RE-entrant, and Starfish). These designs were chosen based on their prevalence in existing research, including references [116-118]. **Figure.II.21** illustrates the starfish cells, with a total of 30 cells arranged in a pattern of 3×4 (width × height), resulting in a unit size of 121 mm×57 mm×10mm. The honeycomb structures were designed using CATIA software, with each cell having dimensions of 127×20×10mm³. The manufactured dimensions for each cell were 18×21×10mm³. Various dimensions for the honeycomb structures are detailed **in Figure.II.21**.

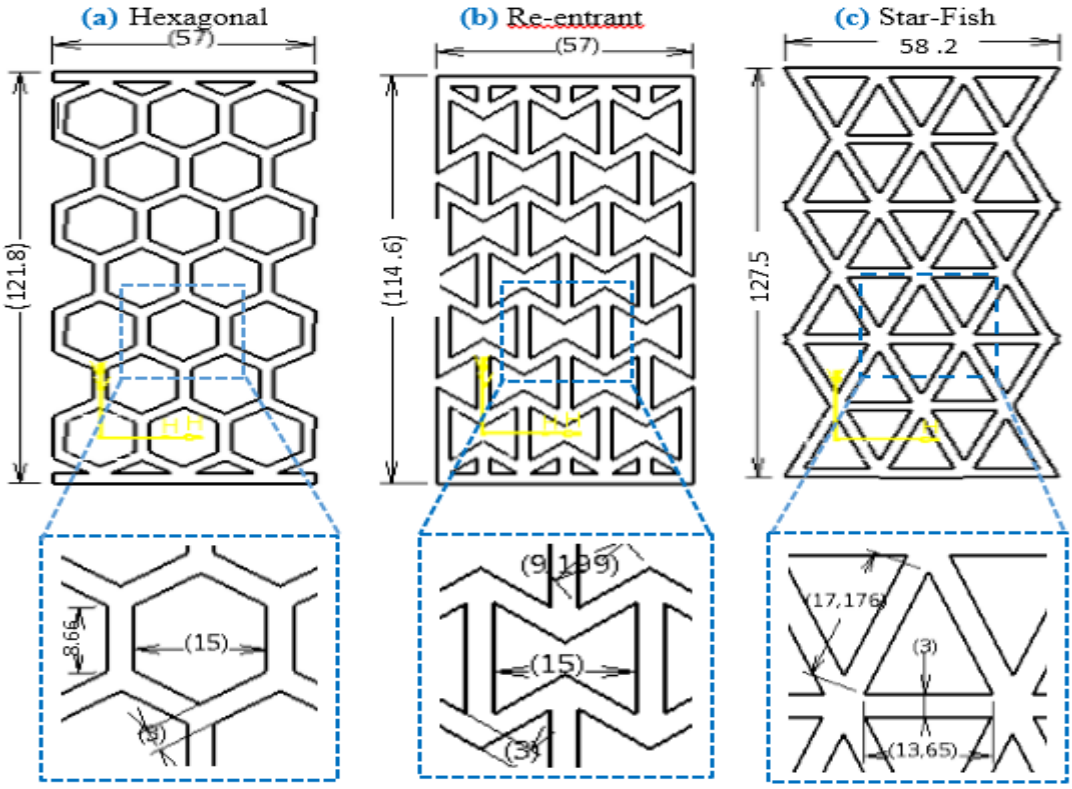

Figure II.21: Dimensions of samples for : (a) hexagonal,(b) Re-entrant,(c) Star_fish

Through-thickness compression testing of the honeycomb was carried out on all core samples (Hexagonal, RE-entrant, and Starfish) using a testing machine with load cells of 10 kN. The test crosshead speed was set at 0.2 mm/min. Damage modes were monitored through the force-displacement curve, as displayed by the testing machine **(Figure II.22)**

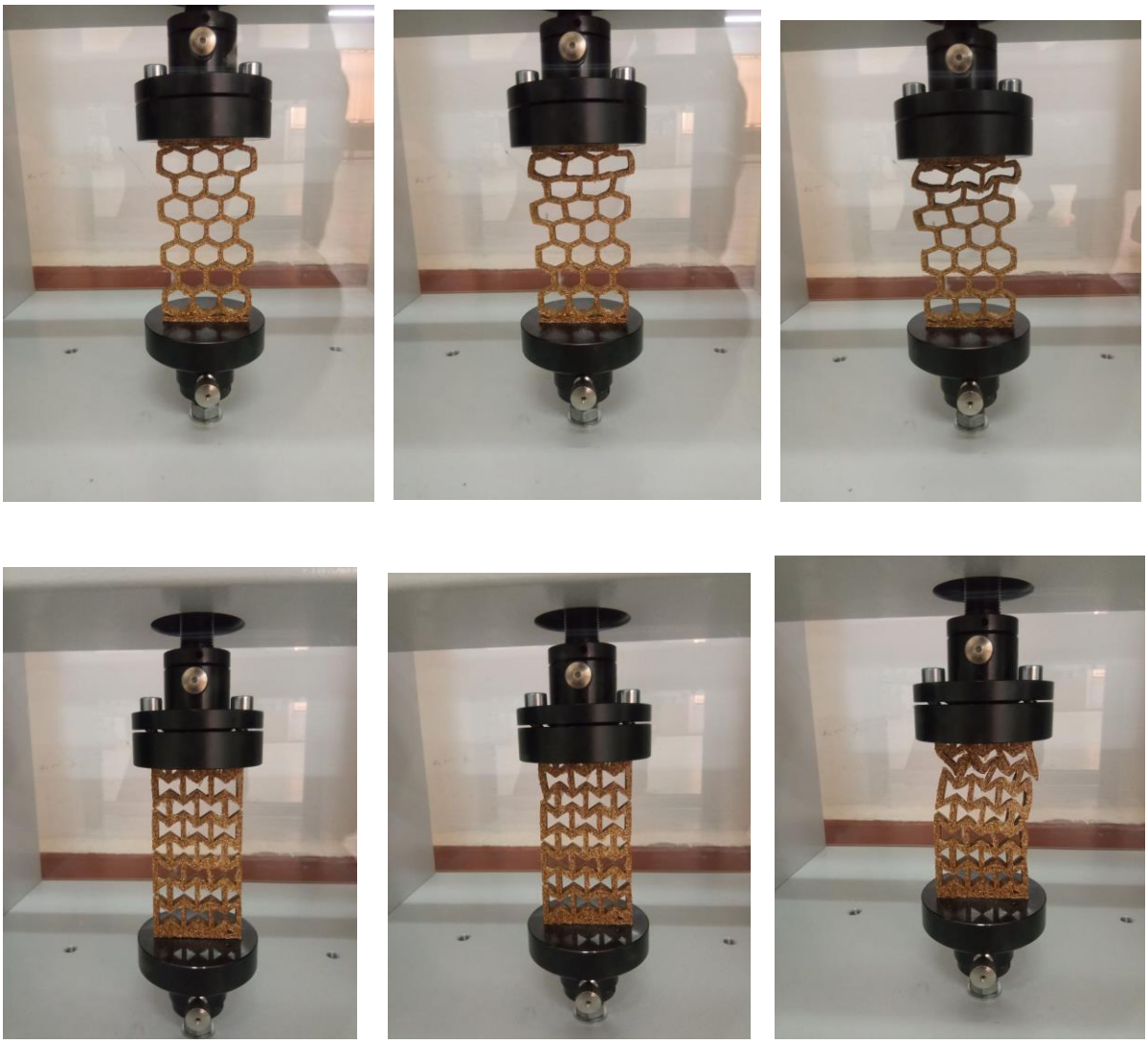

Figure II.22: Cell wall deformation behavior under compression at three different instants (Lab of msila)

II.7.Conclusion

This chapter is dedicated to the extraction of fibers and the fabrication of biocomposites, including a detailed description of the various devices and machines utilized. The primary conclusions drawn from this chapter are as follows:

Extracting fiber from it is challenging. The detailed presentation of the adopted technique enables the obtaining of fibers up to one meter in length for date palm fibers.

The silicone molding method produces samples with a precise and consistent final shape, offering advantages in comparison to shearing methods, as indicated by international measurements.

The preparation of bio composite necessitates 24 hours for drying, or more depending on the air temperature. In addition, bio-composites are manufactured through molding.

Examining Absorption Characteristics: This discourse explores the porosity of natural fibers and its impact on water absorption within bio-composites. Emphasis is placed on the pivotal role of porosity in shaping water absorption capacity and the mechanical properties observed in bending tests.

Lastly, this chapter describes the experimental technique and parameters employed in static.

CHAPTER III:

Results and discussions

III.1. Introduction

In this chapter, a comparative evaluation of the mechanical performance of biocomposites is provided. This analysis includes tensile properties for tensile specimens, three-point bending for bending specimens, and compression for honeycomb, re-entrant, and star-fish structures, along with an examination of absorption in bending samples. The introduction of fibers in biocomposites, with varying proportions, is linked to increased load resistance. The study delves into the deformations and damage patterns of various cells, exploring their overall performance. Additionally, the obtained results are presented and discussed in conjunction with relevant findings from previous research.

III.2. Experimental analysis

III.2.1.Analysis of tensile test specimens of epoxy

Conducting a tensile test on three epoxy specimens—undamaged, with hole-notch, and with elliptical-notch, provided the mechanical properties. These values were subsequently employed for numerical analysis using the Abaqus program, and the outcomes are detailed in **Table III.1.**

Table III.1: Mechanical properties of Epoxy specimen under tensile test

Features	Young's modulus (MPa)	ε-Fmax (%)	εBreak (%)	σBreak (MPa)	Maximal stress (MPa)
Undamaged specimen	1,793.80	4.12	5.19	34.74	39.58
Hole-notched specimen	1,423.36	2.11	2.30	19.15	21.06
Elliptical-notched specimen	547.59	3.30	3.86	10.36	11.21

III.2.1.1. Mechanical test results

Figure III.1 depicts the standard deviation results for three epoxy samples: the intact specimen, hole-notched specimen, and elliptical-notched specimen, across Young's modulus, stresses, and strains. The impact of hole diameter and shape on mechanical properties is evident in **Figure III.1-a**, where the average Young's modulus for five tensile tests on the epoxy samples is presented. The undamaged specimen exhibited a higher average Young's modulus at 1812.2±61.05 MPa, in contrast to the specimen with a hole (1450.41±162.51) MPa and the specimen with elliptical-notch (750.77±198.53)MPa.

Figure III.1-b illustrates the mean stress values for the three epoxy samples, showcasing the influence of sample geometry on stress. Larger hole diameters correspond to lower stress values, with mean stress values of 41±2.45, 21±2.17%, and 11.89±4.3% for undamaged, hole-notched, and elliptical-notched specimens, respectively.

In **Figure III.1-c,** the results of parametric deviation of deformation are presented. The undamaged specimen exhibited a mean deformation value of 3.90±0.47%, while the hole-notched specimen showed a mean deformation value of 2.16±0.13%. The mean strain value for the elliptical-notched specimen was 2.77±0.64%. These results align with previous studies highlighting the influence of hole diameter on mechanical properties[119, 120].

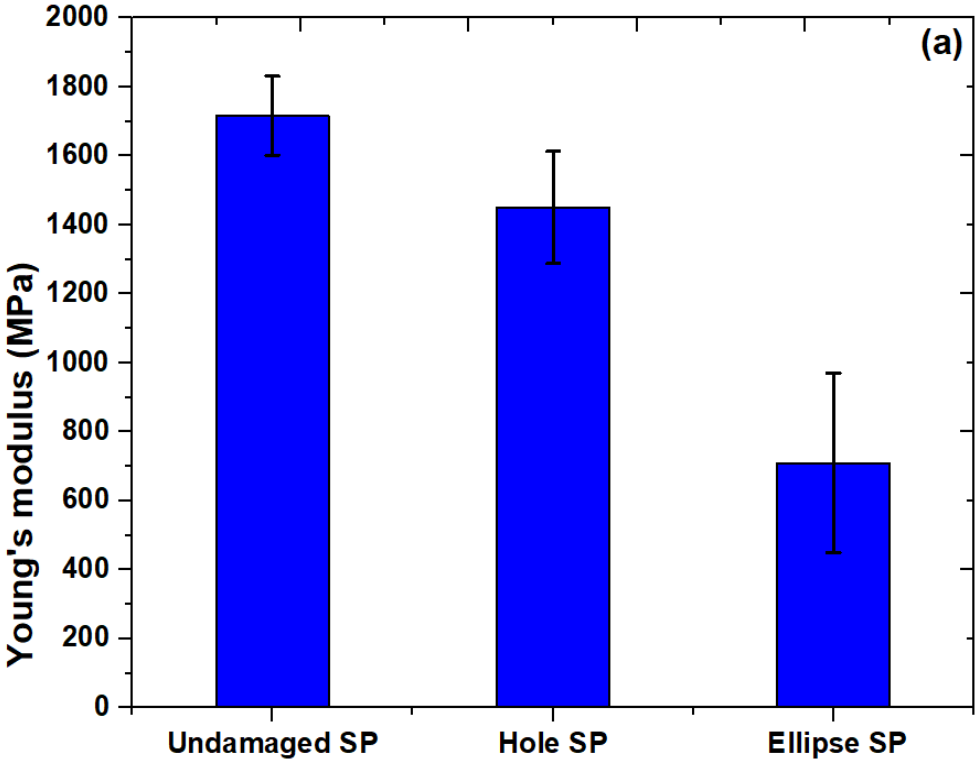
(a)
Young's modulus (MPa)
2000
1800
1600
1400
1200
1000
800
600
400
200
0
Undamaged SP
Hole SP
Ellipse SP

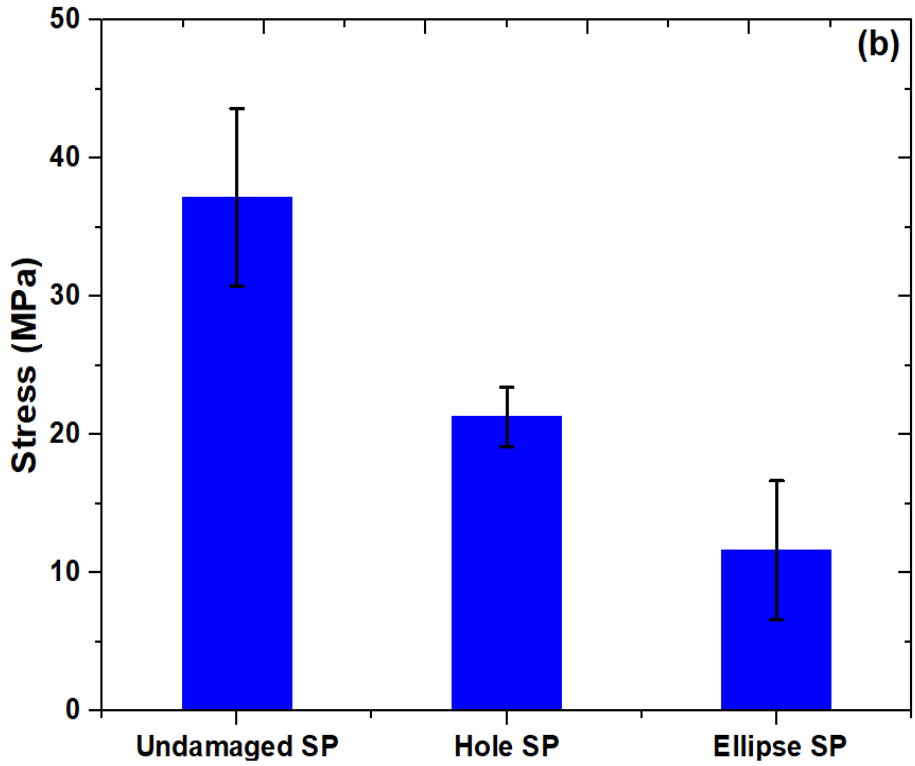
(b)
Stress (MPa)
50
40
30
20
10
0
Undamaged SP
Hole SP
Ellipse SP

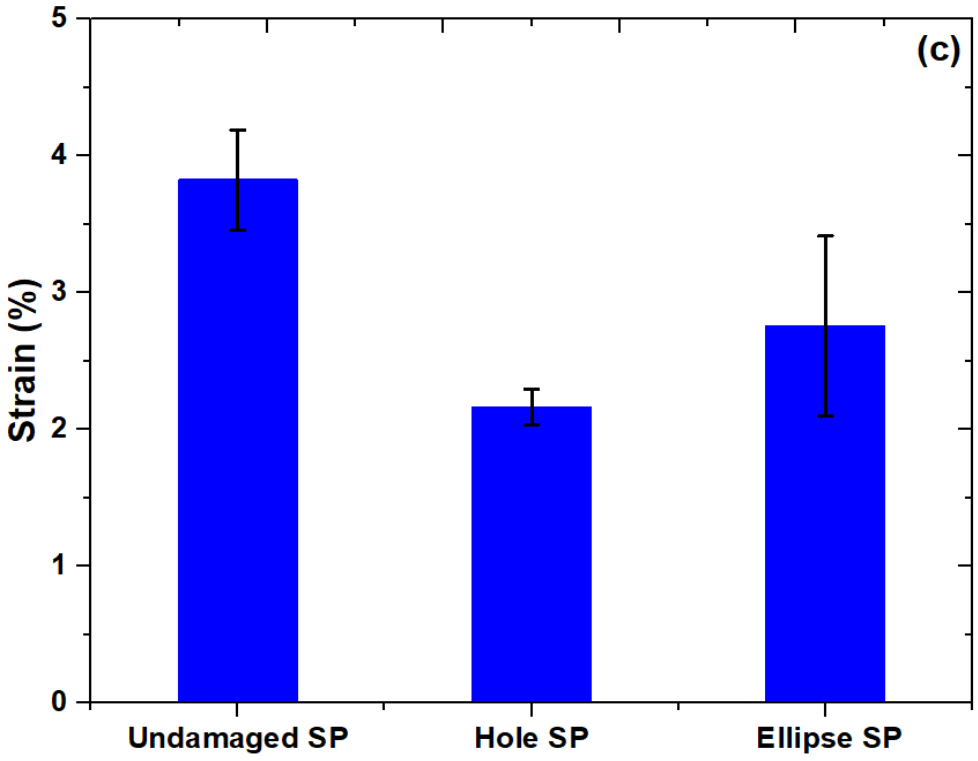

Figure III.1: Mechanical test results: (a) Young's Modulus, (b) stress and (c) strain

The experimental results were obtained from five samples for each specimen, illustrated in **Figure III 2 - (a)** for the undamaged specimen, **Figure III 2-(b)** for the hole-notched specimen, and **Figure III.2-(c)** for the elliptical-notched specimen. Achieving reproducibility of results was somewhat challenging, especially for samples with elliptical notches due to the difficulty in machining this shape. Nevertheless, for the other specimens, the curves exhibited similar shapes.

There was a noticeable variation in the tensile curves for all three specimens, indicating that the mechanical properties of resistance (stress and Young's modulus) as well as deformation were influenced by the presence of notches.

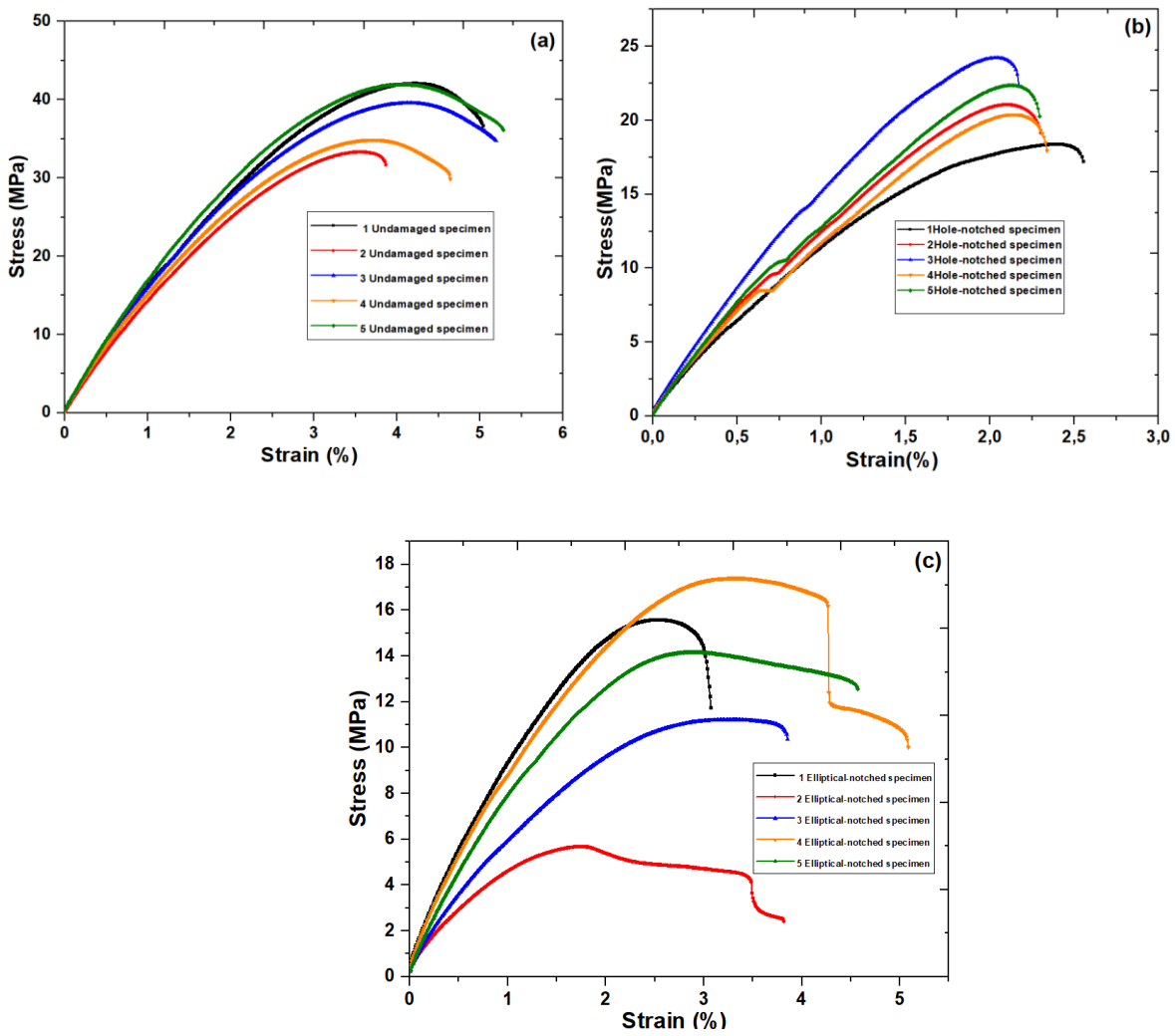

Figure III.2: All experimental results for:(a) undamaged specimen, (b) specimen with hole-notched and (c) specimen with elliptical –notched.

In Figure III.3, experimental results for the undamaged specimen, specimen with hole-notch, and specimen with elliptical-notch are depicted. The curve represents mean values for the three samples (undamaged, hole-notched, and elliptical-notched) in terms of stress-strain during tensile tests, highlighting the influence of sample geometry on mechanical properties. Notably, the undamaged specimen exhibited the highest maximum stress value at 41.95 MPa, accompanied by a strain of 4.05%. In contrast, the maximum stress value for the hole-notched specimen was 21.06 MPa, with a corresponding strain of 2.10%. The specimen with elliptical-

notch displayed a maximum stress of 14.17 MPa and a deformation of 2.89%. These results underscore the impact of aperture length on tensile test outcomes and stress, consistent with previous research.[121]

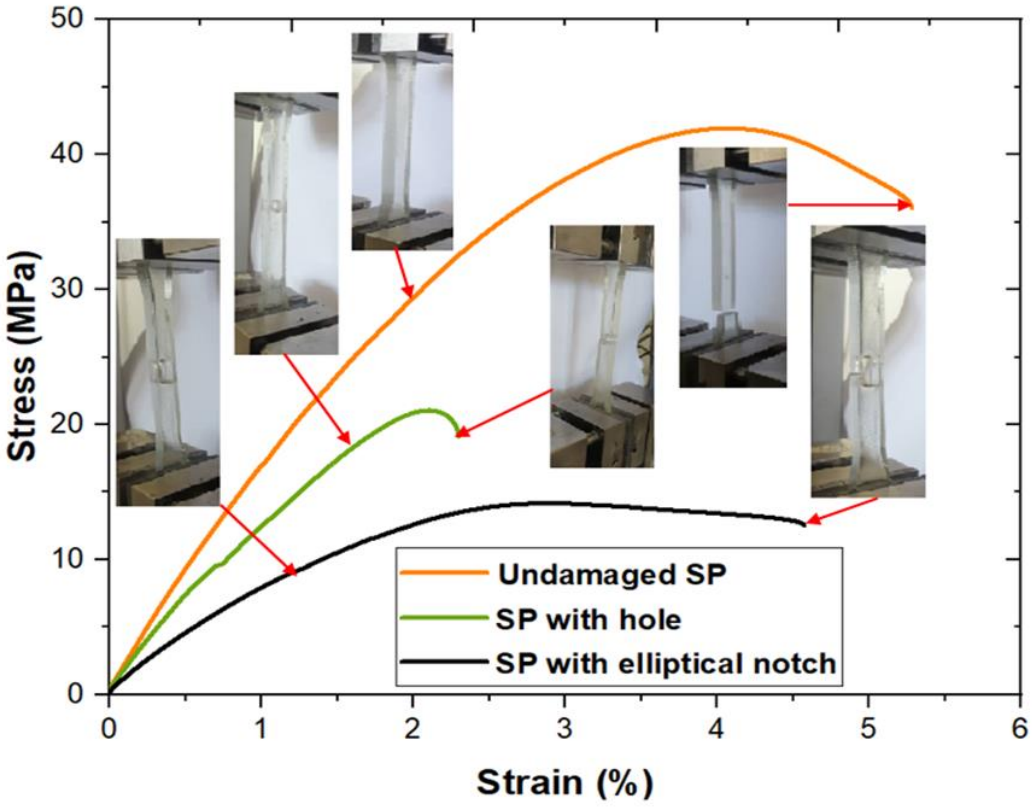

Figure III.3: Experimental results for: undamaged specimen, specimen with hole-notched and specimen with elliptical –notched

In **Table III.2:** experimental results are listed with models according to two inputs, reflecting sample geometry and sample cross-sections, with either Young‘s Modulus or constraint as output.

Table III.2: Experimental results of stress and Young's Modulus

N°	Input variables			Output variables (EXP)	
	Geometry		Specimen section (mm^2)	Maximum Stress (MPa)	Young's Modulus (MPa)
1	Hole-notched specimen	-1	102.555	18.404	1261.79
2		-1	97.524	21.060	1423.36
3		-1	83.913	24.221	1684.47
4		-1	102.684	20.391	1356.42
5		-1	90.2979	22.366	1526.02
6	Elliptical -n-notched specimen	0	88.33	11.008	545.09
7		0	86.7162	5.6846	967.12
8		0	84.6945	11.213	547.59
9		0	86.296	17.404	899.84
10		0	90.5692	14.171	794.25
11	Undamaged specimen	1	86.31	45.767	1858.00
12		1	85.4642	41.950	1836.78
13		1	87.4324	42.132	1713.70
14		1	87.318	40.133	1858.79
15		1	85.1332	39.576	1793.80

Figure III. 4 illustrates that cracks propagated directly from the hole's edge to the nearest edge of the samples, attributed to the quasi-isotropic characteristic of the epoxy composite specimens. This phenomenon is evident in the optical images provided in Figure III. 4, show casing tensile specimens after fractures for all three types (undamaged, circular, and elliptical). In notched specimens, the

damage extended across the width of the specimen on either side of the hole, while different damage patterns were observed at various locations on solid specimens. The fracture of the damaged specimen occurred along the plane perpendicular to the direction of maximum tensile stress.

Figure III.4: Tensile specimens after fractures

III.2.2. Results For bio composite (epoxy/Palm)

III.2.2.1. Tensile specimen analysis for experimental results

- The samples exhibited the maximum stress (20.82 MPa) after undergoing a 24-hour treatment with sodium bicarbonate at a fiber content of 20%.
- Conversely, the minimum stress (9.52 MPa) was observed with a 24-hour treatment with sodium bicarbonate at a fiber content of 15%.
- Both the percentage of fiber and the duration of sodium carbonate treatment had a discernible impact on the stress levels of the samples, as illustrated in **Figure III.6-a**.

- Regarding deformation, the maximum value (3.01%) occurred at a fiber content of 25% with a 96-hour treatment with sodium bicarbonate. In contrast, the minimum deformation (1.21%) was noted for a fiber content of 30% with no treatment, as shown in **Figure III.5-b.**
- **Figure III.5-c** presents the average Young's modulus for the samples, with the highest value (1838.16 MPa) achieved at a fiber content of 20% after a 24-hour treatment with sodium bicarbonate. The lowest Young's modulus value (846 MPa) was recorded for a fiber content of 15% with a 24-hour treatment.

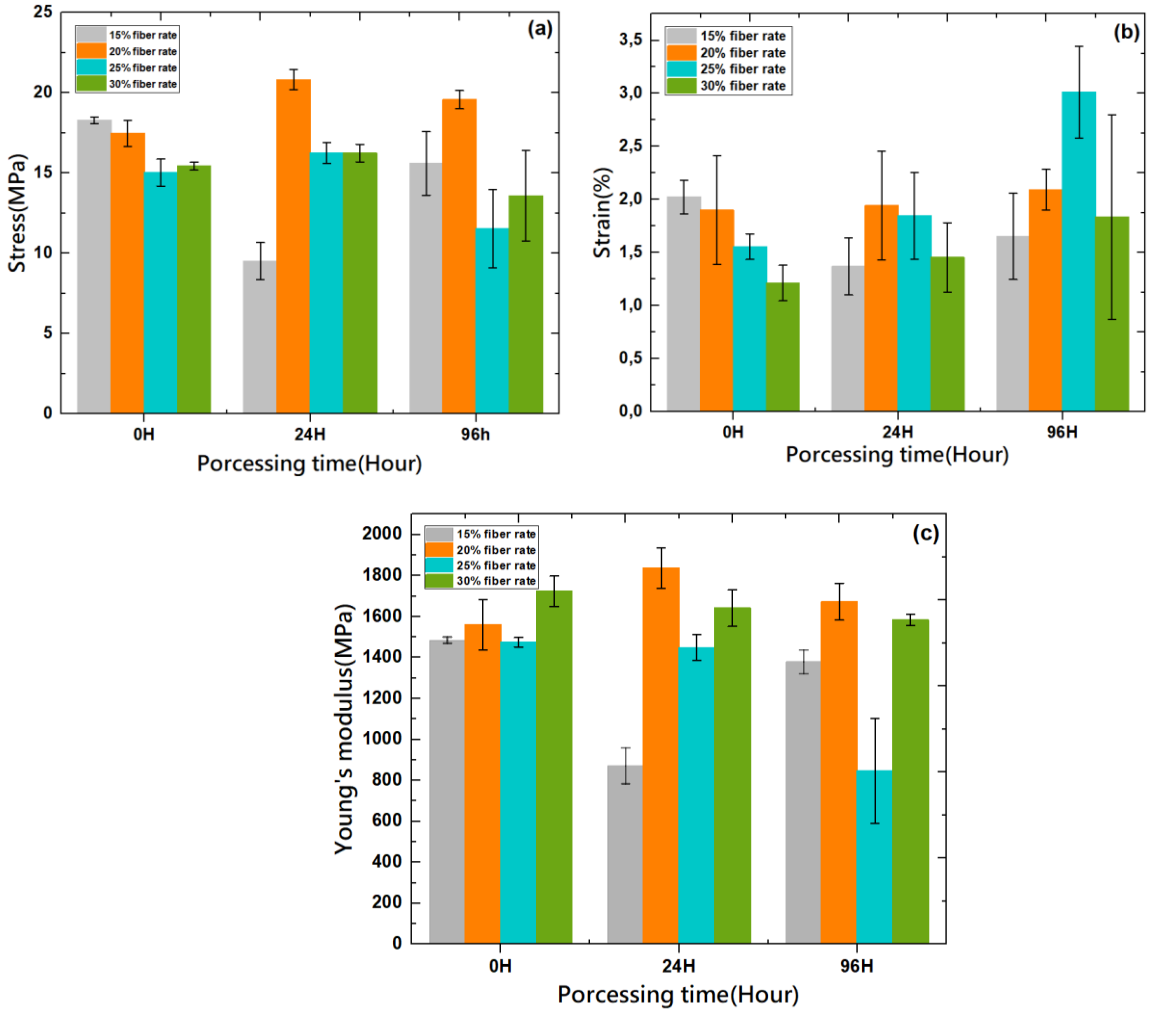

Figure III.5: Evolution of the mechanical properties of bio-composites (a) stress (b) strain (c) Young modulus

III.2.2.2. Results for tensile test

The experimental findings shown in Figure III.5 underscore the substantial influence of fiber content on both stress levels and Young's modulus in the samples. Notably, the highest stress values are achieved with a fiber content rate of 20% and a processing time of 24 hours. This specific condition demonstrates the best performance for the sample, as illustrated in the stress curve presented in Figure III.6.

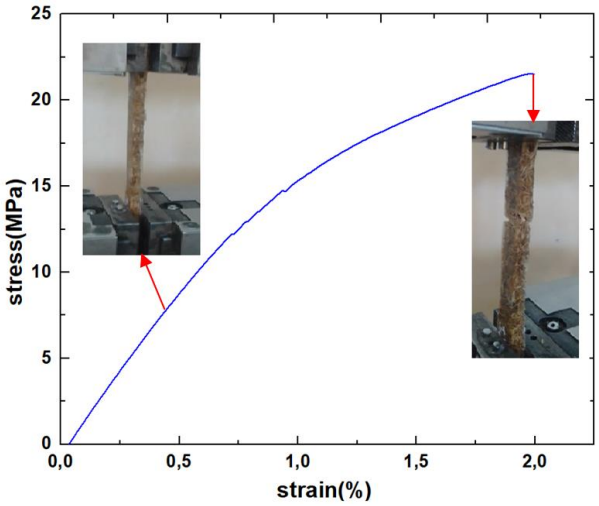

Figure III.6: Curve type Stress/strain 24h/20%

Figure III.7.depicts the specimens after they were broken during tensile testing, revealing extensive cracks in the date palm specimens across various areas. Different damages were evident at distinct locations on the solid specimens, and the fracture occurred along the plane perpendicular to the direction of the maximum tensile stress. Most fractures are located at the top or bottom of the samples.

Figure III.7: Samples after tensile test

III.2.3. Experimental results for bending

III.2.3.1. Experimental results for the bending test

The objective of this section is to assess the performance of reinforced biocomposites with varying compositional patterns (Diss, Sisal and Luffa) under three-point bending stress conditions. In **Figure III.8**, the results of tests conducted according to ASTM D790 are presented. **Figure III.8.** Provides insights into the bending properties of biocomposites featuring different texture structures.

Specifically, sisal fabric composites exhibited the highest stress values, with $\sigma = 31.151 \pm 1.8243$ MPa for 10% sisal fiber content, 26.43833 ± 5.31547 MPa for 15% sisal fiber content, and 23.14767 ± 5.29338 MPa for 25% sisal fiber content, as depicted in **Figure III.8-a**. Furthermore, concerning strain outcomes, fiber composites containing 25% Luffa fiber (1.17933±0.25898%) demonstrated significantly higher values compared to other biocomposites (Diss and sisal biocomposites), as illustrated in **Figure III.8 - b.**

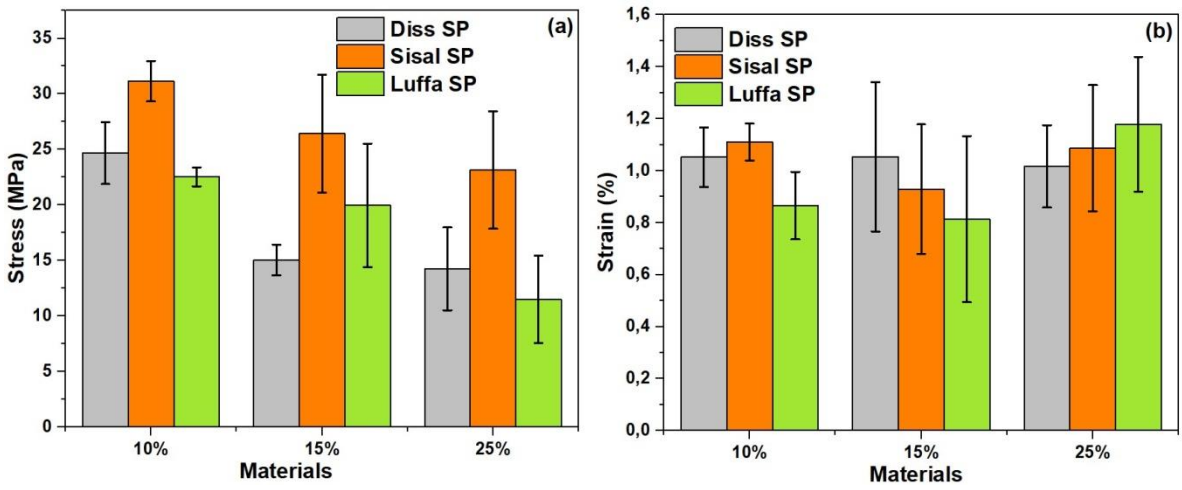

Figure III.8: The effect of the bending test on bio-composites: (a) Stress, and (b) Strain

III.2.3.2. Experimental results for water absorption

The inherent water-attracting characteristics of most bio-polymeric substances emphasize the need to investigate the water absorption capacity of the bio-composites developed in this study. As illustrated in **Figure III.9**, the graph visually demonstrates the weight increase due to water absorption observed over a 44-day period, with temperatures ranging from 32°C to 38°C. This study systematically analyzes the water absorption behavior of bio-composites, crafted with varying quantities and types of fibers.

Figure III.9 provides insights into the water absorption characteristics of the bio-composites in two distinct phases. In the initial 20 days, the first phase reveals a rapid and linear absorption trend. At a 10% fiber rate, water absorption ratios exceed 2%, 2.5%, and 3% for Sisal, Diss, and Luffa samples, respectively. Similarly, at a 15% fiber rate, the ratios are 3%, 9%, and 5% for Sisal, Diss, and Luffa samples, while at a 25% fiber rate, they reach 5%, 12.5%, and 17% for Sisal, Diss, and Luffa samples.

Following the initial phase, the rate of water absorption undergoes an irregular and slower increase over time, distinctly slower than the initial phase, ultimately reaching a plateau indicative of water uptake equilibrium. In contrast, as shown in **Figure III.9-d,** the water uptake rate of composites with the specified filler loading consistently reaches values of 2.77%, 4.93%, and 8.08% for Sisal samples at fiber rates of 10%, 15%, and 25%, respectively. For Diss samples, the corresponding values are 3.94%, 11.58%, and 15.71% at fiber rates of 10%, 15%, and 25%, respectively. Finally, for Luffa samples, the values are 4.28%, 6.9%, and 20.77% at fiber rates of 10%, 15%, and 25%, respectively, after reaching saturation on the 44th day.

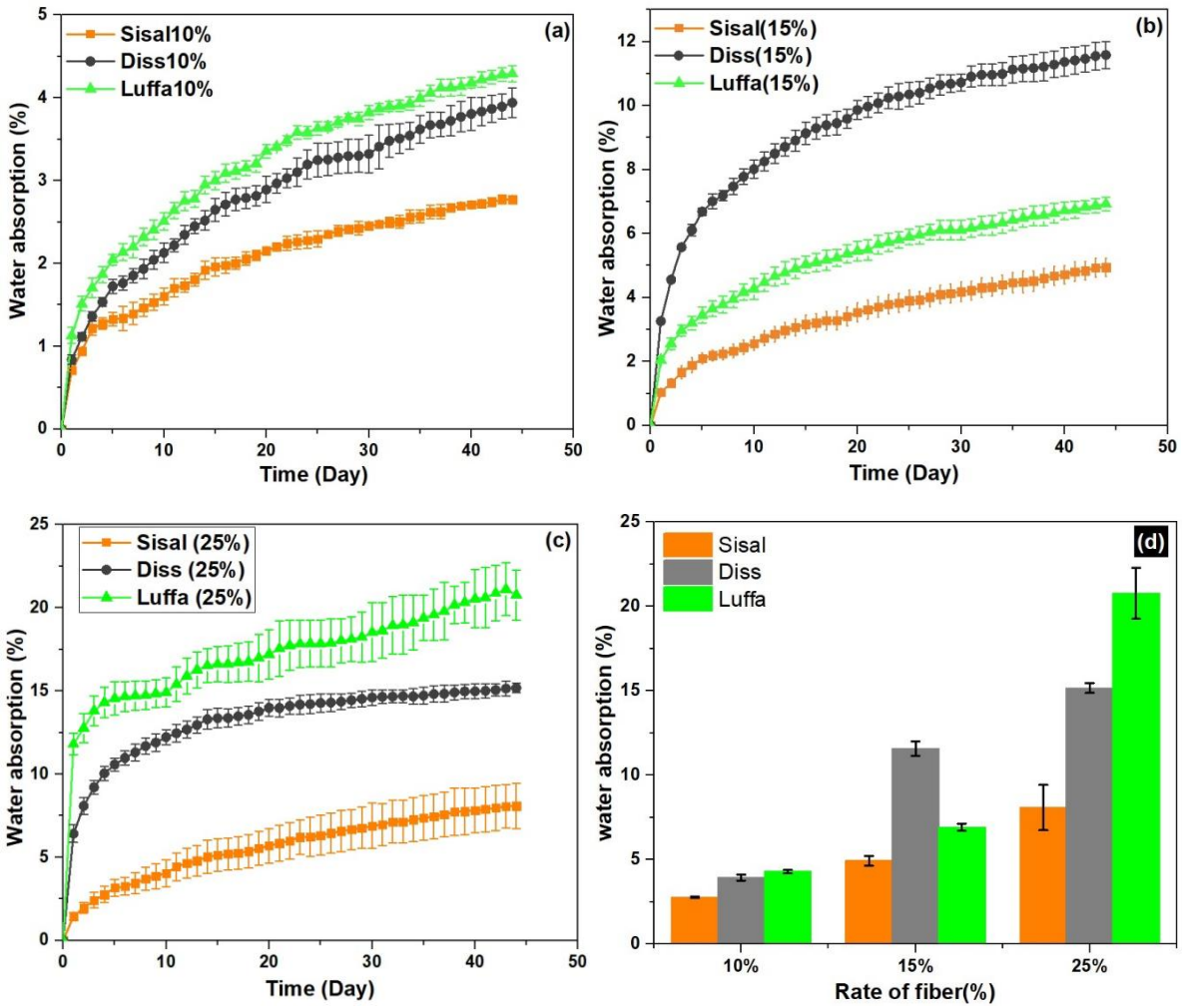

Figure III.9: Illustrates the water absorption of distinct bio-composites featuring various fiber types at different fiber rates: a) 10%, b) 15% (D), c) 25%, and d) a histogram that depicts the water absorption

III.2.4. Resultant For samples of honeycomb

The objective of this section of the study is to assess the performance of beehive bio composite reinforced with different fiber tissues (sisal, Luffa, date palm, and epoxy). Epoxy samples are included as controls and subjected to a compression test with a transmission speed of 0.2 mm/min.

Figure III.10 illustrates the results of compression tests conducted on honeycomb samples with various geometries, including hexagonal, RE-entrant, and star-fish, each integrated with different bio composites with a fiber ratio of 20. The graphical representation reveals the mechanical properties of each type of bio-composites. The average encapsulated force results for all samples under compression are depicted.

Among the tested compounds, Luffa fabric compounds (Luffa biocomplex) exhibited the highest force values, measuring 868.04087 ± 87.27 N. For hexagonal honeycomb engineering, the force was 199.68 ± 253.27 N, while for RE-entrant honeycomb engineering, it was 2975.49 ± 188.96 N. In the case of star-fish honeycomb engineering, the force was shown to be considerably higher.

As depicted in **Figures III.10-a**, **III.10-b** and **III.10-c**, the texture compounds for bees in engineering showed honeycomb structures resembling star-fish, demonstrating significantly greater force values compared to hexagonal and RE-entrant forms.

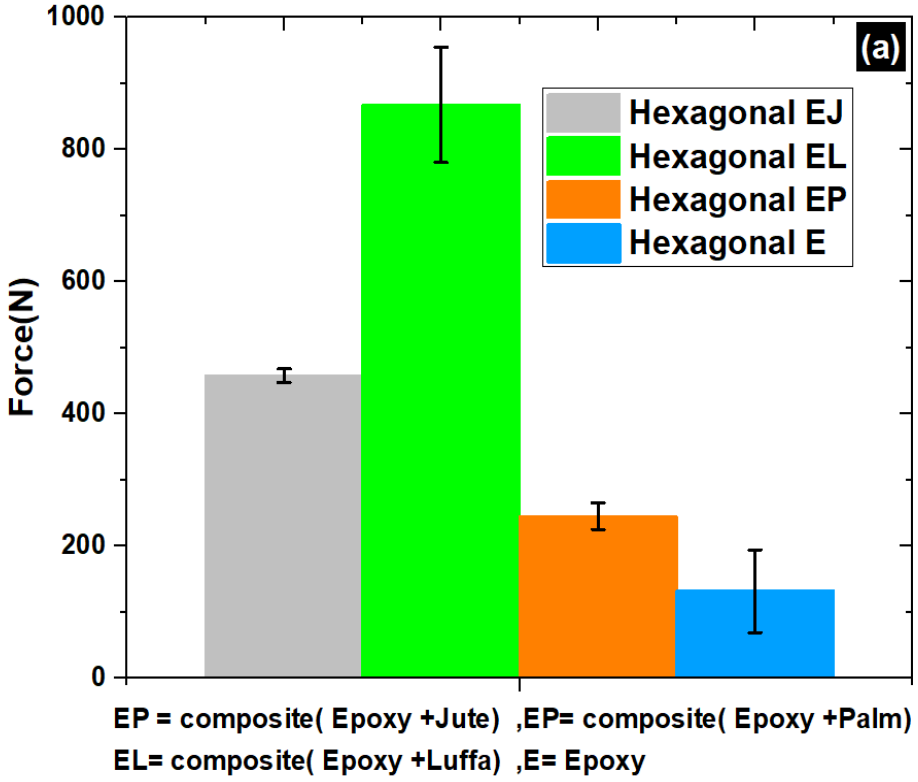
(a)
Hexagonal EJ
Hexagonal EL
Hexagonal EP
Hexagonal E
Force(N)
1000
800
600
400
200
0
EP = composite(Epoxy +Jute) ,EP= composite(Epoxy +Palm)
EL= composite(Epoxy +Luffa) ,E= Epoxy

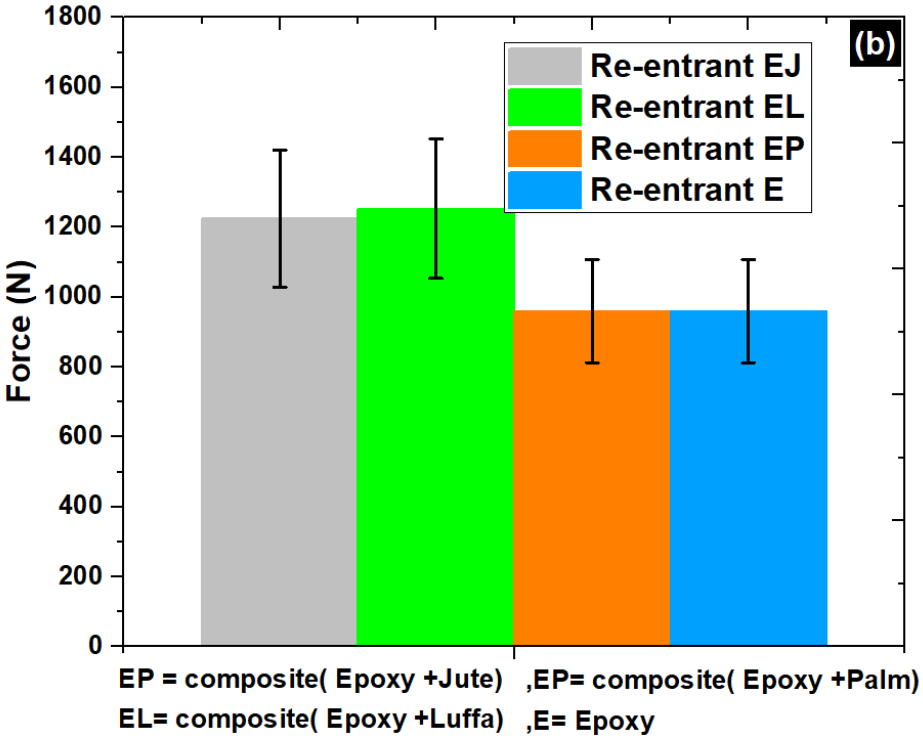
(b)
Re-entrant EJ
Re-entrant EL
Re-entrant EP
Re-entrant E
Force (N)
1800
1600
1400
1200
1000
800
600
400
200
0
EP = composite(Epoxy +Jute) ,EP= composite(Epoxy +Palm)
EL= composite(Epoxy +Luffa) ,E= Epoxy

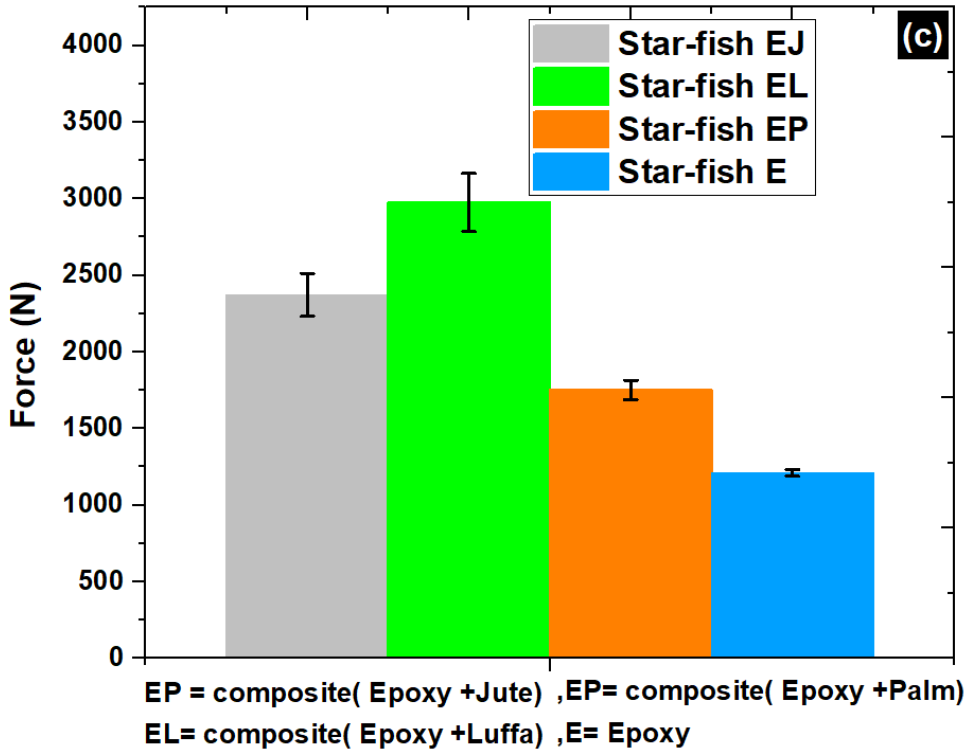

Figure III.10: Evolution of the mechanical properties of bio-composites for force: (a) Hexagonal, (b) Re-entrant and (c) Star-fish

In **figure III.11**, experimental results are presented for the honeycomb in three different geometries: hexagonal, RE-entrant, and star-fish, using fiber-reinforced epoxy compounds such as sisal, Luffa, and date palm. The curves representing the average values for these three samples (hexagonal, RE-entrant, and star-fish) are depicted, showcasing the results of compression tests for force and transmission.

The outcomes highlight the influence of the honeycomb 's varying geometry on mechanical properties during compression tests. Notably, maximum strength values were observed for the star-fish sample, reaching 2220.75416 N for the epoxy sample, 3107.74593 N for date palm fiber samples, and 3352.20426 N for sisal fiber samples. The luffa fiber sample exhibited the highest force value at 4338.33585 N, while lower force values were recorded for hexagonal and RE-entrant geometries, particularly for the honeycomb with date palm fibers.

In the case of the RE-entrant shape, the highest force value was 989.19154 N for the epoxy sample, 1016.89746 N for date palm fiber samples, and 1171.35904 N for sisal fiber samples. The luffa fiber sample again showed the highest force value at 1327.47595 N. For the hexagonal honeycomb geometry, the force values were 219.33198 N for the epoxy sample, 550.32435 N for date palm fiber samples, and 893.8752 N for sisal fiber samples. The highest force value recorded was 951.2786 N for the luffa fiber sample, aligning with findings from previous research [122].

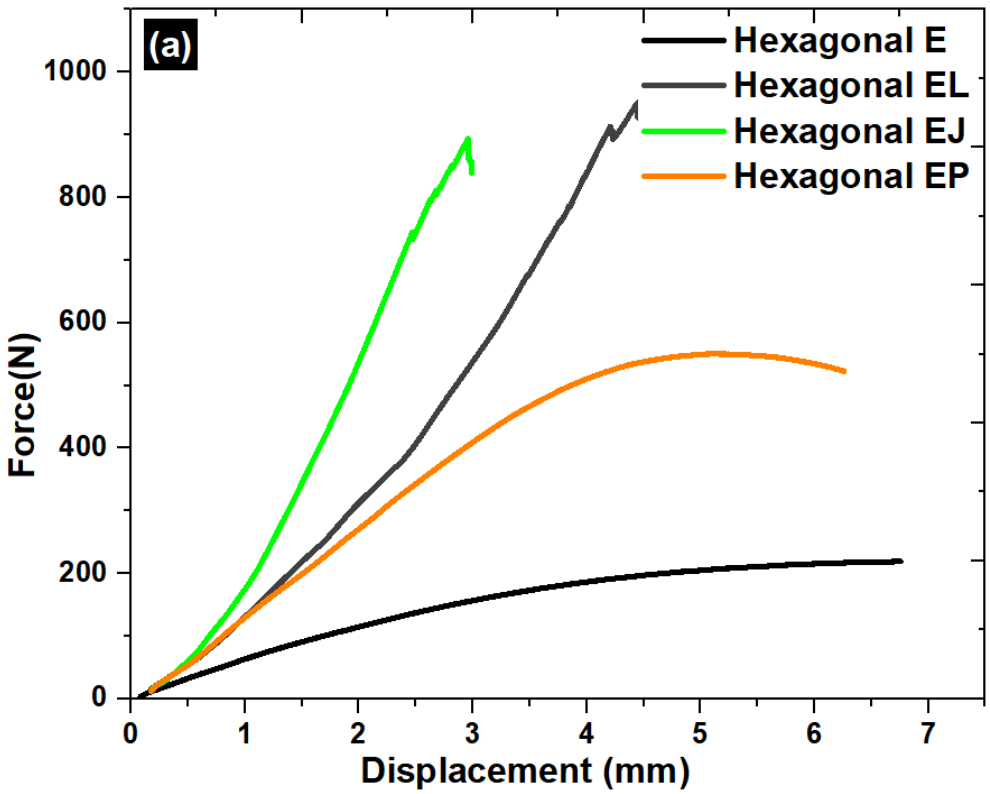

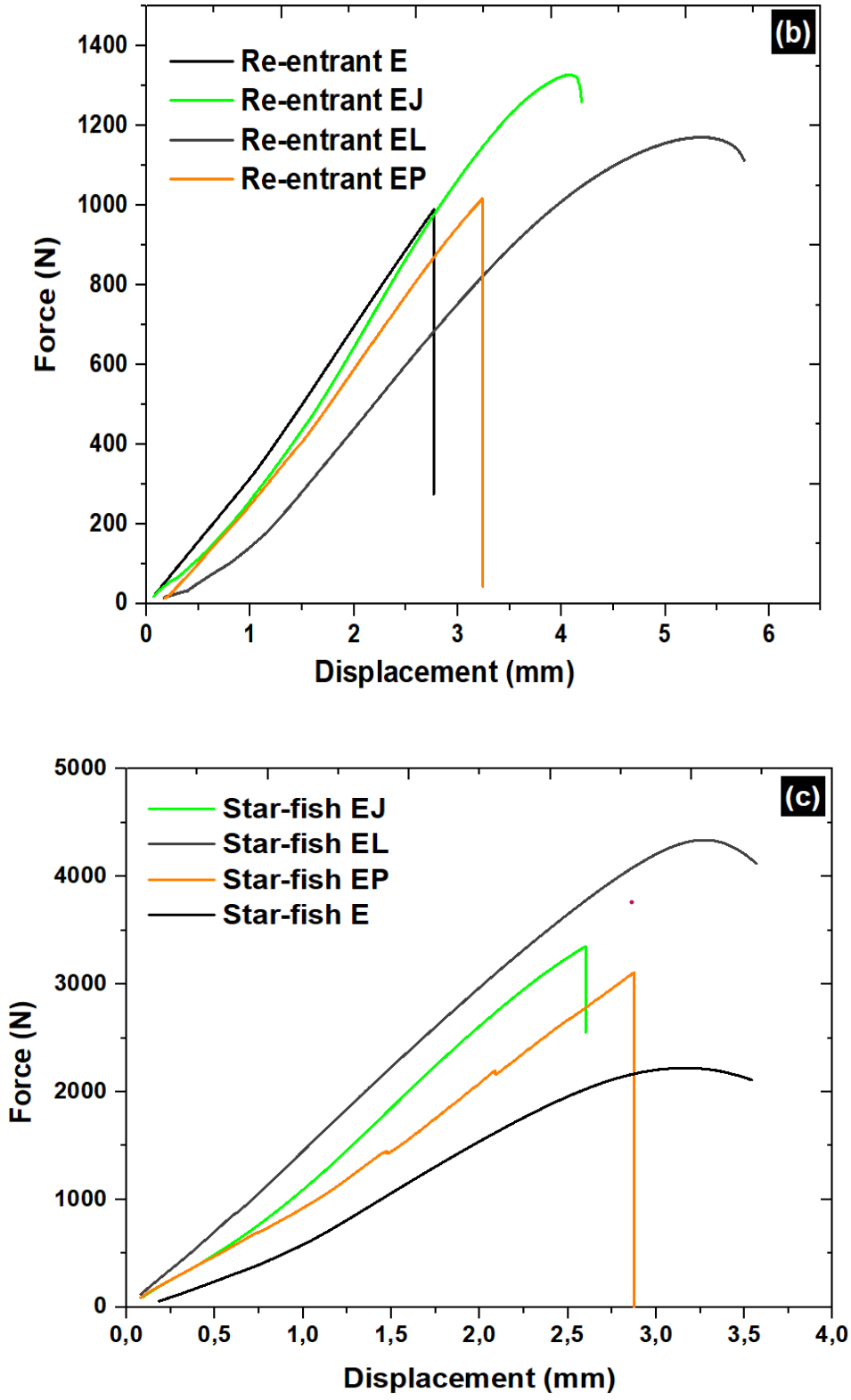

Figure III.11. Force- displacement for bio-composite: (a) hexagonal, (b) re-entrant and (c) Star-fish

The compression test behavior of beehive structures investigated in this study is influenced by rupture mechanisms. Unlike stem cell flame-induced unstable rupture observed in some materials, natural fiber/epoxy structures do not exhibit such behavior. Additionally, they show reduced damage resulting from failure mechanisms commonly observed in fiber composites, such as fiber retreat, fiber rupture, and axial rupture, as illustrated **in Figure III.12.** On the contrary, the heterogeneity present in natural/epoxy composite fibers, arising from local variations in properties and fiber orientation, may act as preferential sites for damage. The damage after breaking occurred within the cell structure of the Honeycomb, which varied depending on the shape of the honeycomb and the type of fiber it, is used.

Figure III.12: Samples of honeycomb after compression test

III.2.5. FTIR studies

FTIR analysis of the spectra revealed differences in the compositions of sisal fibers, diss, loofah, and date palm fibers, whether treated or untreated with sodium bicarbonate. The spectra of these compounds (**Figure III.13** and **Figure III.14**). Clearly show the presence of lignin, cellulose, hemicellulose, and an inorganic component. Analyzing the vibration peaks for Diss, Sisal, Luffa, and

date palm fiber composites, the stretching of Si-O-Si groups is evident at 1043.95 cm^{-1}. Notably, expansion occurs at COH -1239.3 cm^{-1} for date palm fiber compounds, and the C-H stretch of date palm fibers treated with sodium bicarbonate for 24 hours is observed at 1321.01 cm^{-1}.

Furthermore, a broad absorption band at 3011.68 cm^{-1}, 3306.14cm^{-1}, and 3078.78 cm^{-1} is noticeable in composite of palm, composite of Sisal, and composite of Luffa fibers, respectively. This band is attributed to the expansion of OH groups in hemicellulose, cellulose, and lignin, indicating OH vibrations in these components.

IR region	*Wave number (cm^{-1})*	*Functional group*	*References*
1000–1100	*1043.65 for com-sisal*	*C-H sym. deformation vibration*	*[123]*
1225-1265	*1239.3 for com-Palm T96*	*-COH stretching vibration*	*[124]*
2100–2200	*2181.42 for com-Palme T96*	*C–C stretching vibration*	*[125]*
2915–2950	*2948.32for com-Diss*	*C-H stretching vibration-asym (hemicellulose)*	*[126]*
3125-3575	*3306.14 for com-sisal*	*O-H stretching vibration, broad Cellulose ,hemicelluloses and lignin*	*[127]*

Table III. 3: IR region and vibration of FTIR spectra of bio composites of Diss , sisal ,Luffa and palm fiber.

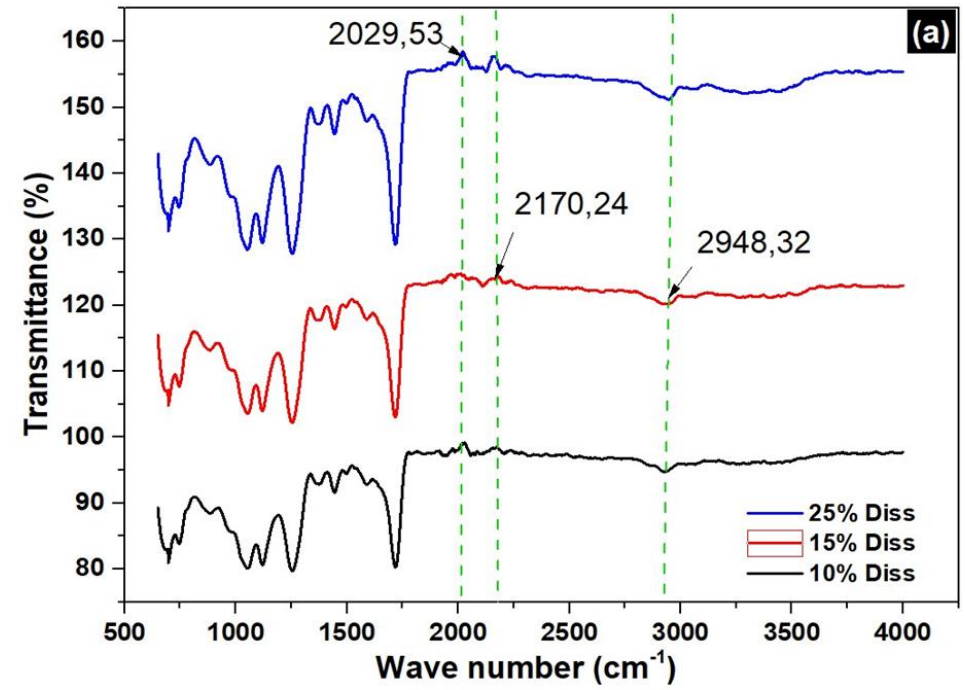
(a)
2029,53
2170,24
2948,32
Transmittance (%)
Wave number (cm-1)
25% Diss
15% Diss
10% Diss

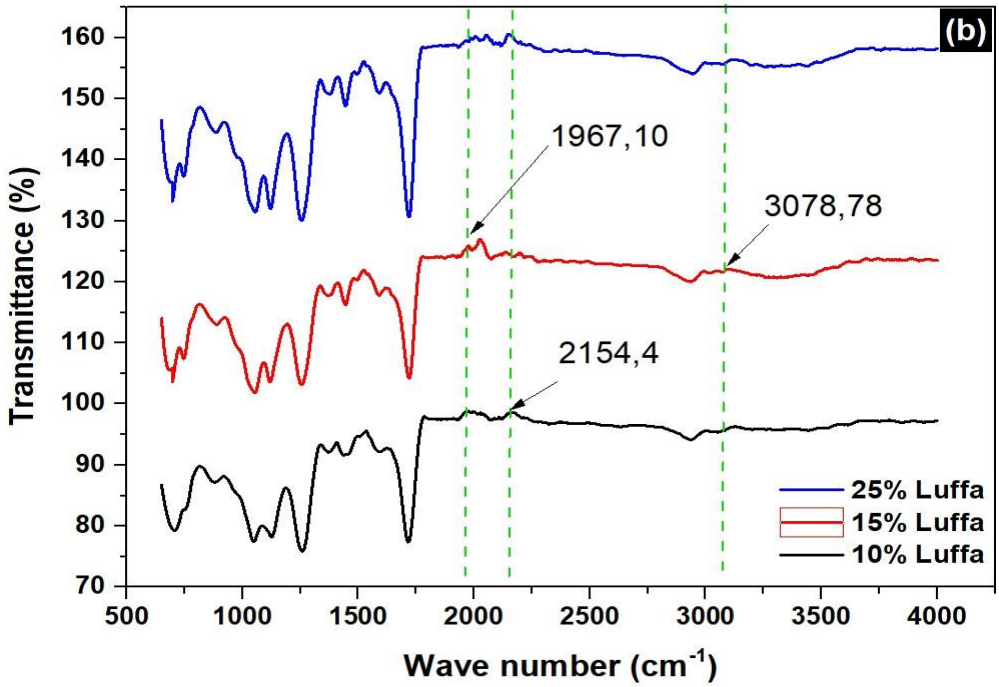
(b)
1967,10
3078,78
2154,4
Transmittance (%)
Wave number (cm-1)
25% Luffa
15% Luffa
10% Luffa

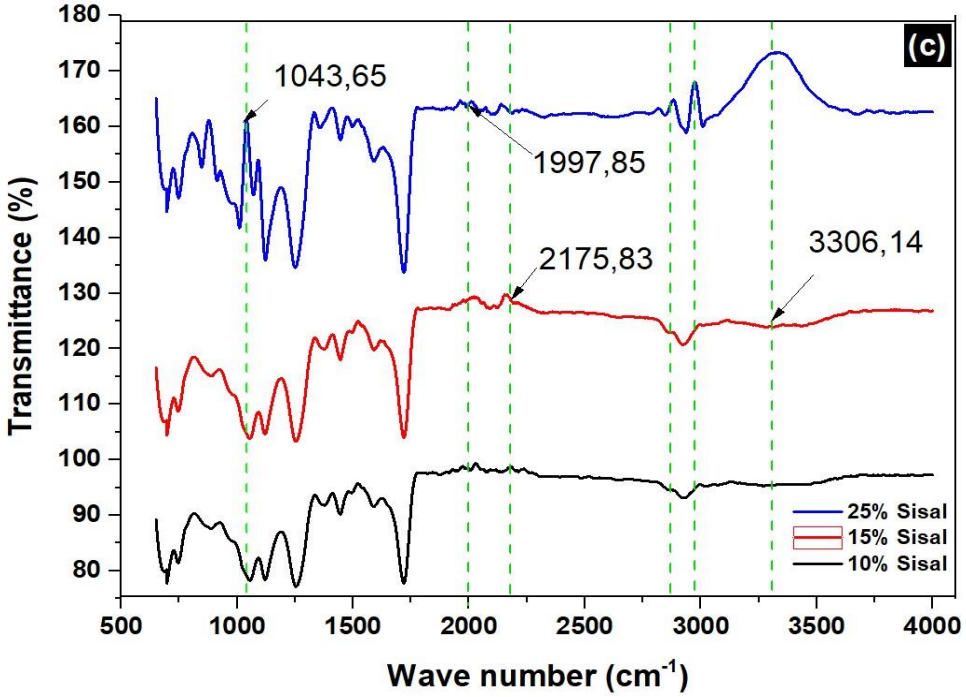

Figure III.13.FTIR spectra for samples of fiber :(a) Diss,(b)Sisal and (c) Luffa

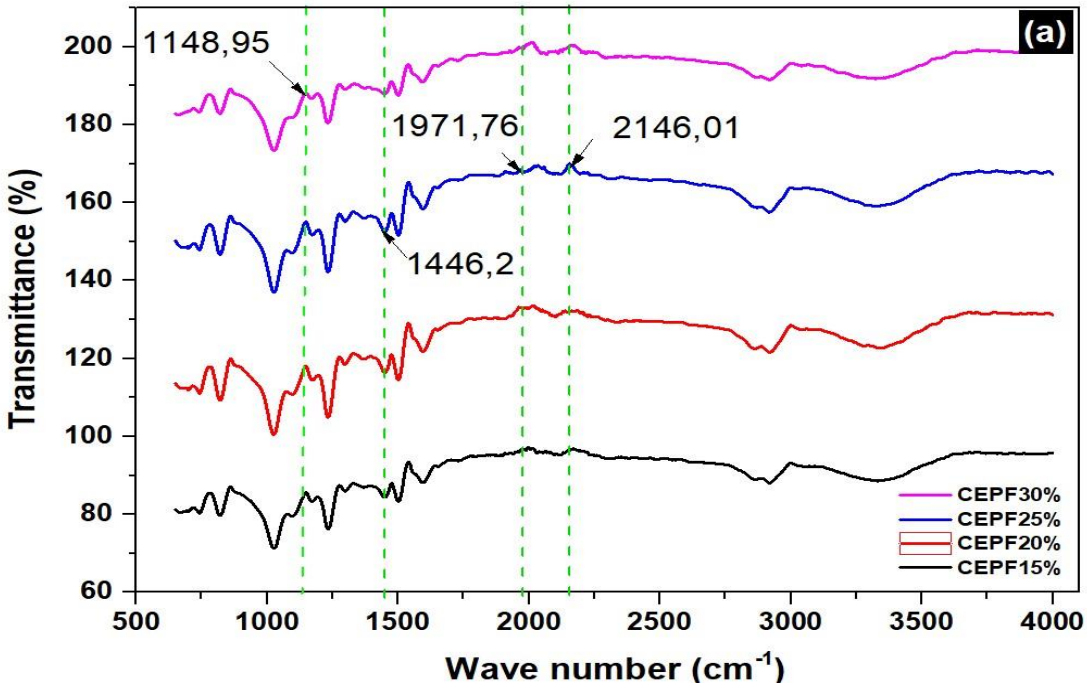

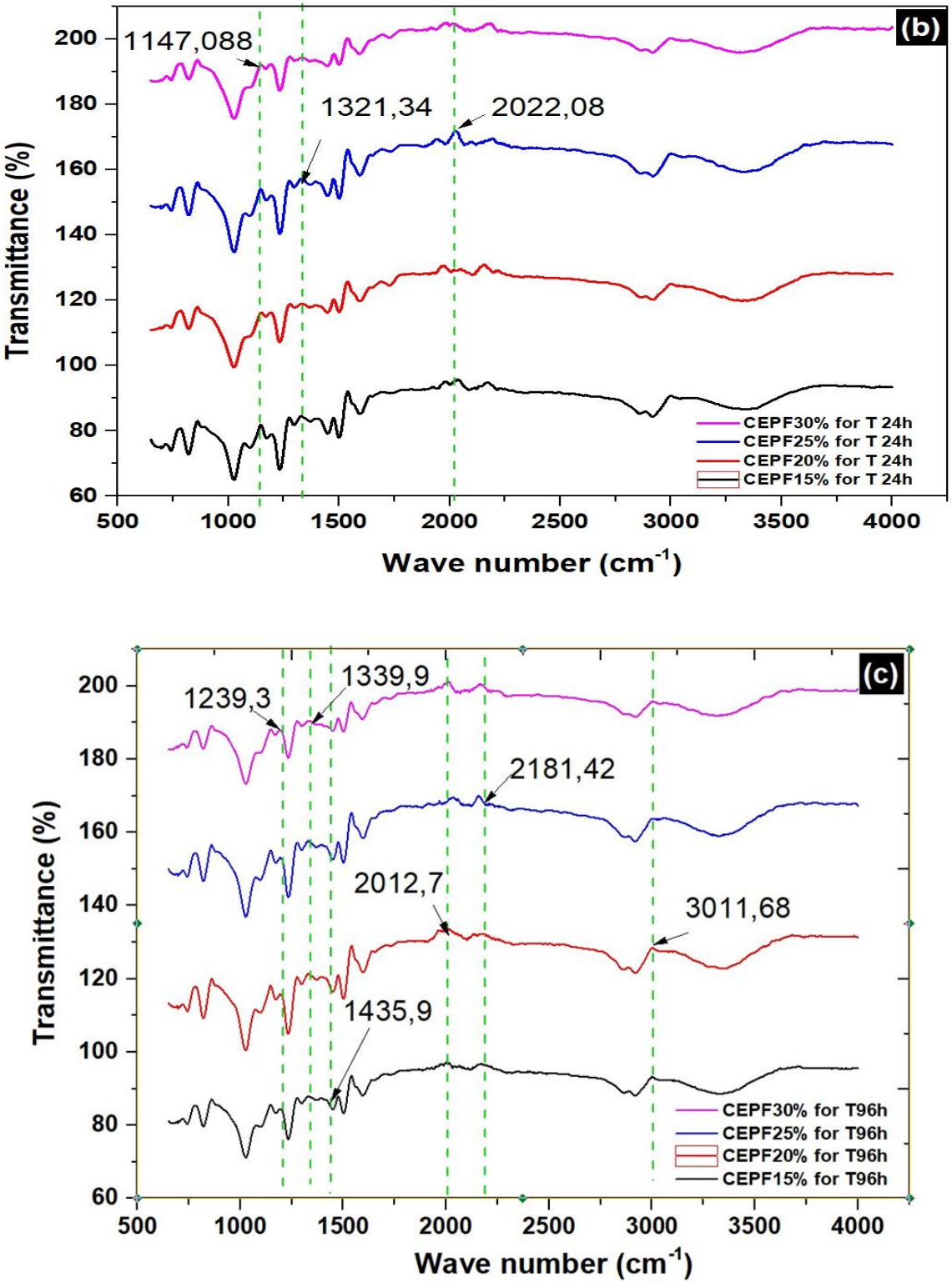

Figure III.14: FTIR spectra for samples of fiber Palme treated for :(a) 0h, (b)24h and (c) 96h

III.3.Conclusion

This chapter III leads to the following main conclusions:

- The obtained experi-mental results indicate that undamaged specimen has ultimate stress of 41.22MPa and young's modulus of 1793.80 MPa which are the strongest part among the studied specimens. Comparison of the ultimate stress indicates that an increase in hole diameter leads to a decrease in the strength of the part. The ultimate maximum stress is decreased of of 11.21 MPa and a Young's modulus of 547.59 MPa for elliptical-notched specimen. The weakest examined is elliptical-notched specimen. The standard deviations of The three test samples for the undamaged specimen, the hole-notched specimen and the elliptical-notched specimen in the range 6–37%.
- Strengthening the fibers by up to 20% over a 24-hour processing period significantly enhances the mechanical properties of the composite laminates. This is evidenced by the experimental results of palm fiber-reinforced bio-composites.
- Flexural properties decrease as the water absorption content increases in samples with high fiber content.
- Water absorption tests reveal that the absorption rate increases with an augmentation in fiber content within the compound.
- The results of chemical analysis on FTIR spectra reveal variations among compounds of the same fibers at different percentages, ranging from 10% to 30%.

CHAPTER IV

Numerical Methods in ABAQUS

IV.1. Introduction

The primary objective of this chapter is to present a Extended Finite Element Method (XFEM) formulation for the elasto-plastic analysis of stress and strain. The focus is on understanding how the presence of geometric discontinuities influences the tensile strength of epoxy-type polymers, particularly examining how mechanical properties evolve concerning notch shapes. Additionally, the chapter aims to utilize the extended finite element method to analyze stress variation with deformation. Tensile tests were conducted on specimens featuring different geometric discontinuities, including holes and elliptical notches. The investigation delves into the effects of these geometric shapes on the mechanical properties of the polymer, comparing them with undamaged specimens. Experimental results were then compared with those obtained through finite element numerical analysis, utilizing ABAQUS software and incorporating XFEM. The assessment focused on the influence of the geometric notch shape on maximum stress and maximum deformation.

Furthermore, the study highlights the calculation of the stress concentration factor (K_t) in various epoxy specimens. By integrating XFEM into the analysis, the research provides a comprehensive understanding of how the geometric shape of the notch affects both the mechanical properties of the polymer and stress concentration factors. This work contributes valuable insights into the complex relationship between geometric discontinuities and material behavior, offering a more holistic perspective for designing materials with enhanced mechanical performance and durability.

IV.2. Numerical techniques in Abaqus

Numerical methods refer to mathematical techniques used to solve problems through approximation and computation. These methods are employed to obtain numerical solutions to various scientific and engineering challenges.

Abaqus, on the other hand, is a software suite designed for finite element analysis (FEA). Finite element analysis is a numerical method used to find approximate solutions to boundary value problems

for partial differential equations. Abaqus specifically focuses on simulating and analyzing mechanical and structural behaviors, such as stress, deformation, and thermal effects.

The relationship between numerical methods and Abaqus lies in the fact that Abaqus utilizes numerical techniques, particularly finite element analysis, to model and analyze complex physical systems. Users employ numerical methods within the Abaqus framework to simulate and understand the behavior of structures and materials under various conditions. In essence, Abaqus is a tool that applies numerical methods to provide practical solutions for engineering and scientific simulations.

IV.2.1. Geometry transformation

The scaled boundary finite element method SBFEM formulates geometric transformation by combining boundary discretization and a scaling operation on the boundary. **Figure IV.1.a** illustrates the scaling procedure for a quadrilateral surface element, where a volume sector V_e is represented by continuously scaling the surface element S_e to the scaling center. In each volume sector, a three-dimensional scaled boundary coordinate system is established, incorporating circumferential coordinates η, ζ on the surface element and the radial coordinate ζ.

Surface elements along the boundary adopt isoparametric elements, a concept from standard FEM [123]. **Figure IV.1.b** showcases commonly used triangular and quadrilateral elements in their natural coordinates η, ζ with red-marked nodes exclusive to quadratic elements. The surface element's shape functions are denoted by N(η,ζ). The radial coordinate ξ is dimensionless, originating from the scaling center and extending towards the boundary. At the scaling center, ζ = 0, and on the boundary, ζ = 1 is maintained.

The representation of a point $(\hat{x}, \hat{y}, \hat{z})$ within the volume sector Ve can be defined through scaled boundary coordinates (η, ζ, ξ).

$$\hat{x}(\xi,\eta,\zeta) = \xi\,\hat{x}(\eta,\zeta) = \xi N(\eta,\zeta)\,\hat{x} \qquad \textbf{(IV.1)}$$

$$\hat{y}(\xi,\eta,\zeta)=\xi\hat{y}(\eta,\zeta)=\xi N(\eta,\zeta)\hat{y} \qquad \textbf{(IV.2)}$$

$$\hat{z}(\xi,\eta,\zeta)=\xi\hat{z}(\eta,\zeta)=\xi N(\eta,\zeta)\hat{z} \qquad \textbf{(IV.3)}$$

The nodal coordinate vectors of the surface element Se in Cartesian coordinates, denoted as $\hat{x}$, $\hat{y}$, and $\hat{z}$, are used to represent a point in the equation. It is essential to note that all coordinates in Eq. **(IV.1)** are relative coordinates with respect to the scaling center. Here, the scaling center serves as the origin of the local coordinate system, and the hat symbol on variables indicates their connection to this specific local coordinate system.

The relationship between partial derivatives with respect to scaled boundary coordinates and those in Cartesian coordinates can be expressed through the following equation:

$$\begin{Bmatrix} \frac{\partial}{\partial\xi} \\ \frac{\partial}{\partial\eta} \\ \frac{\partial}{\partial\zeta} \end{Bmatrix} = \begin{bmatrix} 1 & 0 & 0 \\ 0 & \xi & 0 \\ 0 & 0 & \xi \end{bmatrix} J_b(\eta,\zeta) \begin{Bmatrix} \frac{\partial}{\partial x} \\ \frac{\partial}{\partial y} \\ \frac{\partial}{\partial z} \end{Bmatrix} \qquad \textbf{(IV.4)}$$

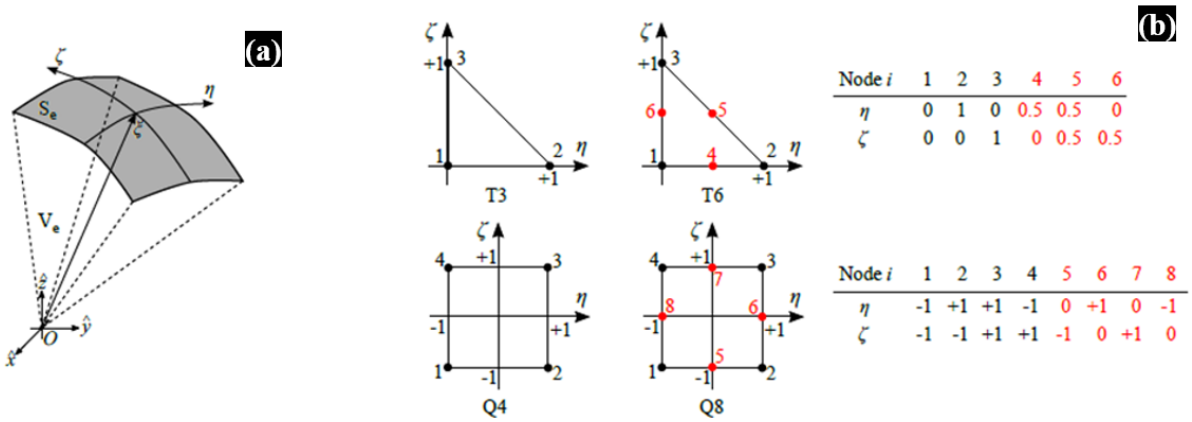

Figure IV.1: Three-dimensional scaled boundary coordinate system: (a) Scaling of the surface element using radial coordinate ξ (ξ = 0 at the scaling center and ξ = 1 on the boundary) and (b) Triangular and quadrilateral reference elements in natural coor

[124]

where $J_b(\eta, \zeta)$ denotes the Jacobian matrix on the boundary ($\xi = 1$), which is defined as

$$J_b J_b(\eta,\ \zeta) = \begin{bmatrix} \hat{x}(\eta,\zeta) & \hat{y}(\eta,\zeta) & \hat{z}(\eta,\zeta) \\ \hat{x}(\eta,\zeta)\eta & \hat{y}(\eta,\zeta)\eta & \hat{z}(\eta,\zeta)\eta \\ \hat{x}(\eta,\zeta)\zeta & \hat{y}(\eta,\zeta)\zeta & \hat{z}(\eta,\zeta)\zeta \end{bmatrix} \qquad \textbf{(IV.5)}$$

The determinant of $J_b(\eta, \zeta)$ is given as

$$|J_b| = \hat{x}(\hat{y}_{,\eta}\ \hat{z}_{,\zeta} - \hat{z}_{,\eta}\ \hat{y}_{,\zeta}) + \hat{y}(\hat{z}_{,\eta}\ \hat{x}_{,\zeta} - \hat{x}_{,\eta}\ \hat{z}_{,\zeta}) + \hat{z}(\hat{x}_{,\eta}\ \hat{y}_{,\zeta} - \hat{y}_{,\eta}\ \hat{x}_{,\zeta}) \qquad \textbf{(IV.6)}$$

Where, for the sake of clarity, the argument (η, ζ) has been omitted.

IV.2.1.1. Strain field

Within scaled boundary coordinates, the strain field ε(ζ; η; ξ) is derived from the displacement field

L

$$\varepsilon(\zeta,\eta,\xi) = Lu(\zeta,\eta,\xi) \qquad \textbf{(IV.7)}$$

Which is defined by

$$L = b_1(\eta,\zeta)\frac{\partial}{\partial\xi} + \frac{1}{\xi}\left(b_2(\eta,\zeta)\frac{\partial}{\partial\eta} + b_3(\eta,\zeta)\frac{\partial}{\partial\zeta} \right) \qquad \textbf{(IV.8)}$$

where the matrices $b_1(\eta; \zeta)$, $b_2(\eta; \zeta)$, $b_3(\eta; \zeta)$ can be found in Reference [125]

IV.2.1.2. Stress field

In cases involving linear elasticity, the connection between the stress field (σ, τ, η) and the strain field is established by

$$\sigma(\xi,\eta,\zeta) = D\varepsilon(\xi,\eta,\zeta) \qquad \textbf{(IV.9)}$$

where D is the elasticity matrix, which is expressed as follows for linear isotropic material:

$$D = \frac{E}{(1+\nu)(1-2\nu)}\begin{bmatrix} 1-\nu & \nu & \nu & 0 & 0 & 0 \\ & 1-\nu & \nu & 0 & 0 & 0 \\ & & 1-\nu & 0 & 0 & 0 \\ & & & \frac{1-2\nu}{2} & 0 & 0 \\ & \textit{symmetric} & & & \frac{1-2\nu}{2} & 0 \\ & & & & & \frac{1-2\nu}{2} \end{bmatrix} \qquad \textbf{(IV.10)}$$

IV.3. Numerical analysis

IV.3.1. Mesh view

The numerical model was implemented using the finite element method in Abaqus, employing a fine mesh for various models. The mesh consisted of two types: one around the hole and another as a uniform 3×3 mesh, as illustrated in **Figure IV.2.** Notably, the mesh around the circular and elliptical holes underwent refinement to optimize accuracy compared to a standard mesh in the finite element method. This refinement aimed to improve convergence between experimental and numerical results. Efforts were made to model all three specimens with an equal number of mesh elements, as shown in **Figure IV.2.**

Table IV.1: Input parameters of numerical simulation

Specimen	Total number of nodes	Displacement speed	Mesh type	Young's modulus (MPa)
Undamaged	1008	1	Hexagon (C3D8R)	1793.80
Hole-notched	1050	1	Hexagon (C3D8R)	1423.36
Elliptical-notched	1050	1	Hexagon (C3D8R)	547.59

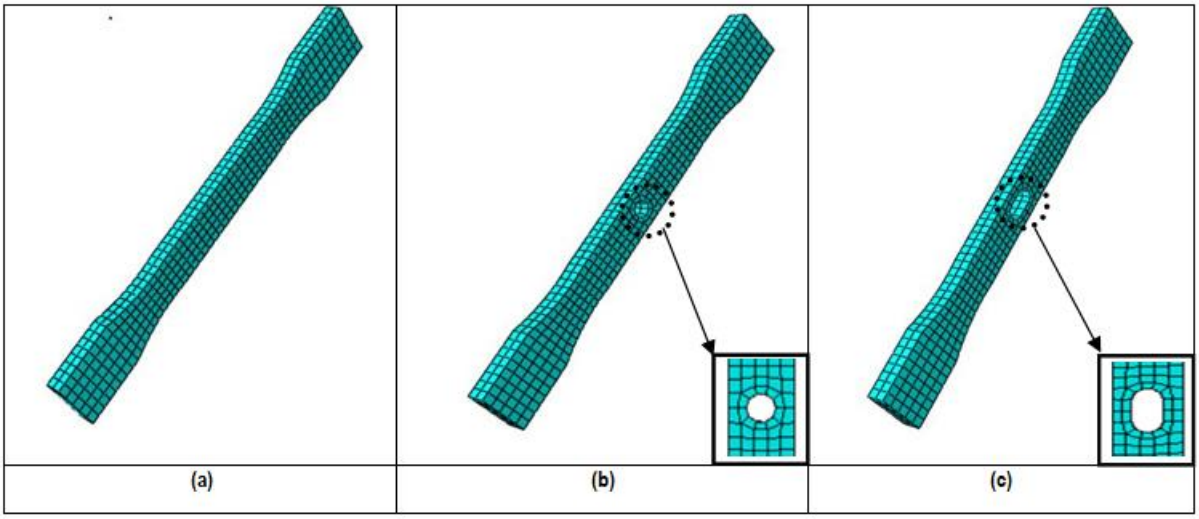

Figure IV.2: Mesh view. (a) The undamaged specimen, (b) The hole-notched specimen and (c) The elliptical-notched specimen.

To simulate realistic loading conditions in the tensile machine, the assumed boundary conditions were as follows: one end of the specimen was embedded, while the other end was subjected to an applied stress. A perpendicular force (F) was applied to the tensile samples at a rate of 1 mm/min, as depicted in **Figure IV.3.**

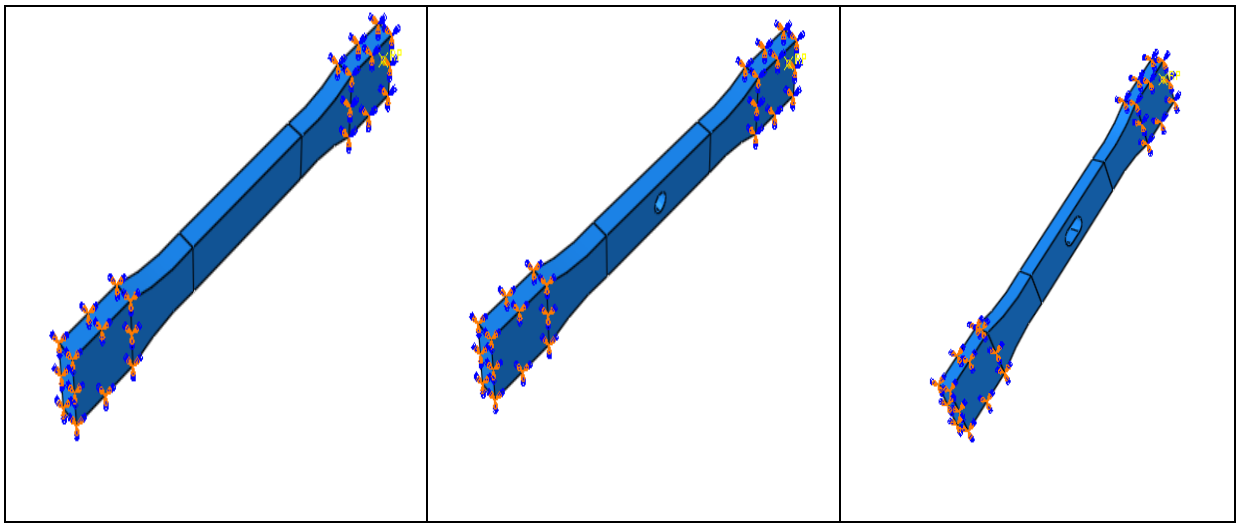

Figure IV.3: Application of force to specimens in ABAQUS program.

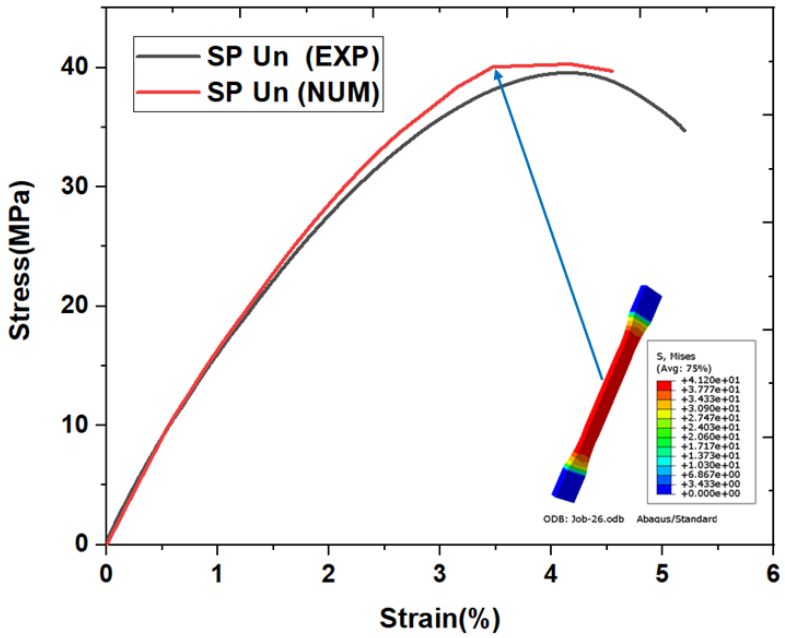

Figure IV.4: Comparison between the experimental results and the numerical for the undamaged specimen

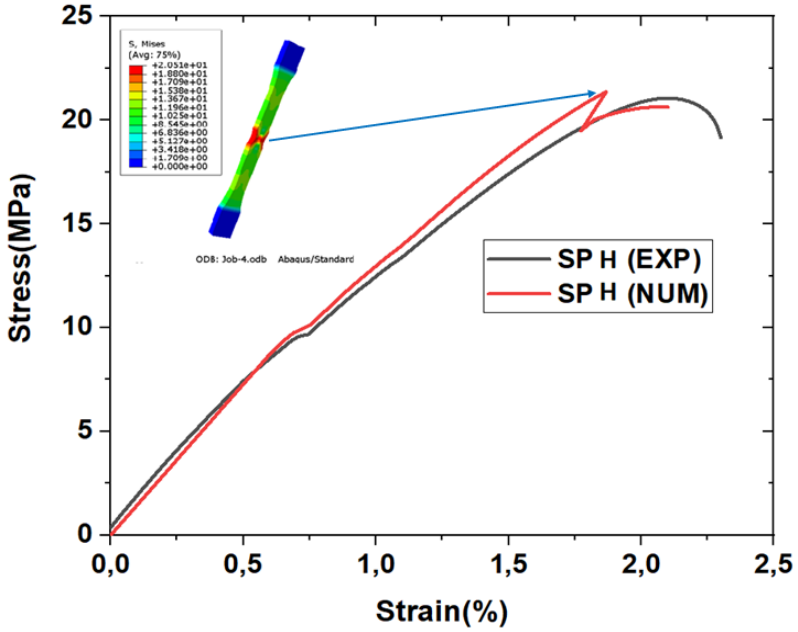

Figure IV.5: Comparison between the experimental results and the numerical for hole-notched specimen

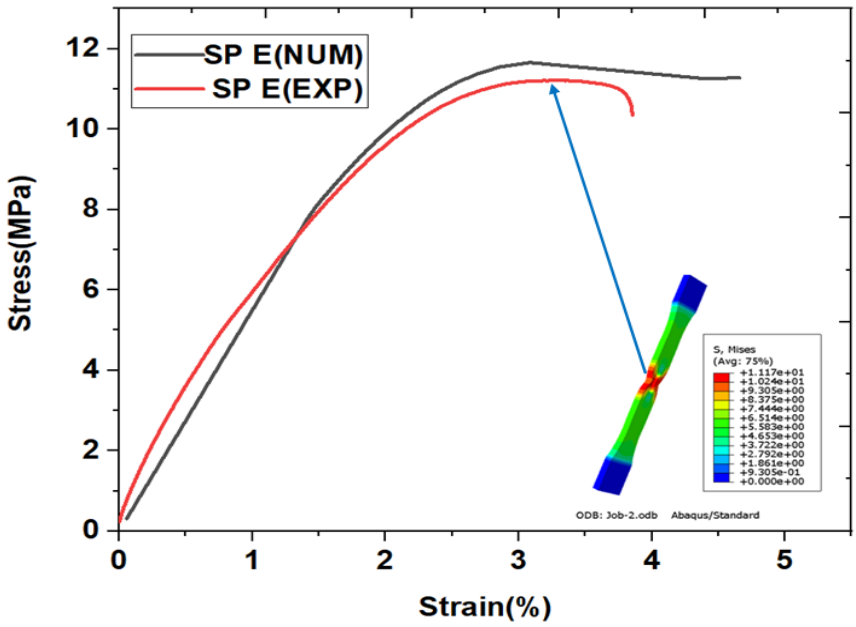

Figure IV.6: Comparison between the experimental results and the numerical for elliptical-notched specimen.

The tensile test of the specimens was conducted numerically, and their behavior was analyzed in relation to the presence of notches. The numerical analysis in ABAQUS software demonstrated convergence between experimental results and numerical analysis for three specimens (**Figures IV. 4, 5,** and **6**). Notably, the undamaged specimen exhibited a maximum stress value (in red) of 41.20 MPa, with a minimum stress (in blue) around 0 MPa **(Figures IV. 4)**. The hole-notched specimen (**Figures IV. 5**) showed a maximum stress value of 20.51 MPa (in red) and a minimum stress (in blue) around 0 MPa. Similarly, the elliptical-notched specimen (**Figures IV. 6**) had a maximum stress value (in red) of 11.17 MPa and a minimum stress (in blue) around 0 MPa.

A concentrated stress area near the notch was observed, diminishing the specimen's resistance. Conversely, the specimen without a notch displayed uniformly distributed stresses along its useful length. The elliptical notch resulted in a higher stress concentration compared to a circular notch. Stresses in the complete sample exceeded those in other samples. A comparative analysis of Young's modulus, maximum stress, and deformation between experimental and numerical results was performed (**refer to Table IV.2**). A slight discrepancy was evident in different properties between simulation and experimental results.

Table IV.2: Experimental and simulation result with error for the stress

Specimen	**Experimental**	**ABAQUS**	**Error (%)**
	Stress (MPa)	**Stress (MPa)**	**Error (%)**
Undamaged	41.20	41.22	0.04
Hole-notched	20.51	21.06	2 .61
Elliptical-notched	11.17	11.21	0.35

Table IV.3: Experimental and simulation result with error for the Young's modulus

Specimen	**Experimental**	**ABAQUS**	**Error (%)**
	Young's modulus (MPa)	**Young's modulus (MPa)**	**Error (%)**
Undamaged	1793.80	1650.01	8.08%
Hole-notched	1423.36	1185.92	16.89%
Eliptical-notched	547.59	474.47	13.35%

It can be seen in **Table IV.3.** That the effect of stresses is higher in the undamaged specimen and lower in the elliptical-notched specimen. Stresses in the undamaged specimen 41.20 MPa and Stresses in

the elliptical-notched specimen 11.17 MPa in the elliptical-notched specimen. While the results of PEMAG (the magnitude of equivalent plastic strains) and PEEQ (equivalent plastic strain) In the Abaqus software, the results were close and similar in the perforated and elliptical-notched specimen and slightly higher in the undamaged specimen.

Table IV.4. Shows, comparing the results of the reactions generated in the three specimens along the steepest region, that the highest value of RF Magnitude is 310.7 N in the undamaged specimen, 83.49 N in the hole-notched specimen and 55.26 N in the elliptical-notched specimen. The displacement is close for the hole-notched specimen and the undamaged specimen of 5.993 mm and 4.580 mm respectively, and it is lower for the elliptical-notched specimen of 1.421 mm.

Table IV.4: Comparison between numerical results for the three specimens on ABAQUS

Specimen	STRESS MAX (MPa)	E MAX(%) principal	PEMAG MAX (%)	PEEQ MAX	RF Magnitude MAX(N)	U Magnitude MAX(mm)	STATUSXFEM MAX
Undamaged	41.20	0.05828	0.03739	0.03740	310.7	4.580	1.000
Hole-notched	20.51	0.04016	0.02635	0.02640	83.49	5.993	1.000
Elliptical-notched	11.17	0.04185	0.02660	0.02660	55.26	1.421	0.4001
	STRESS min (MPa)	**E MIN (%) principal**	**PEMAG min (%)**	**PEEQ min**	**RF Magnitude min(N)**	**U Magnitude min(mm)**	**STATUSXFEM min**
Undamaged	3.333	4.86	0.003116	0.003116	25.89	0.3816	0.0800
Hole-notched	1.709	0.003347	0.002.196	0.002200	6.958	0.499	0.0833

Elliptical-notched	0.9305	0.003488	0.002261	0.0002217	4.602	0.1184	0.03334

IV.4. Results numerical for compression test of honeycomb

The honeycomb structure is constructed from 3mm thick Al 2024-T3 aluminum, and its mechanical properties can be found in Table 2. Aluminum alloy 2024-T3 is highly regarded for its exceptional mechanical traits. With a density of 2.52g.cm^{-3}, it is classified as a lightweight material, making it particularly appealing for applications in the aerospace sector. The material's interface has also piqued the interest of many researchers. [126, 127]

Table IV.5: Presents the mechanical properties of Aluminum alloy 2024-T3

Material	σ_R(MPa)	$\sigma_{0.2}$(MPa)	E(MPa)	A(%)	ϑ
Al 2024-T3	452	230	73800	2.4	0.33

IV.4.1. Numerical analysis

IV.4.1.1. Finite element (FE) modeling

The digital analysis was conducted using the ABAQUS v16.14 general-purpose finite element software. A consistent mesh layout was applied to each honeycomb type (Hexagonal, RE-entrant, and Starfish) utilizing Continuum 3D hexahedral elements (ABAQUS type C3D8R) across all volumes sized at 57 × 120 × 10mm³, showcasing the autonomy of the models. Ultimately, a grid with an approximate overall size of 1mm resulted from dividing each element, leading to a total of 29,840 nodes and 37,570 elements. This information is summarized in **Table IV.6.**

Table IV.6: Which details the mesh-related input parameters.

Type of honeycomb	Type of mesh	Approximate	Number of nodes	Nombre of elements.
Hexagonales	Continuum-3D hexagonal C3D8R	1	29 840	37 570
RE-entrant	Continuum-3D hexagonal C3D8R	1	29 840	37 570
Star fish	Continuum-3D hexagonale C3D8R	1	29 840	37 570

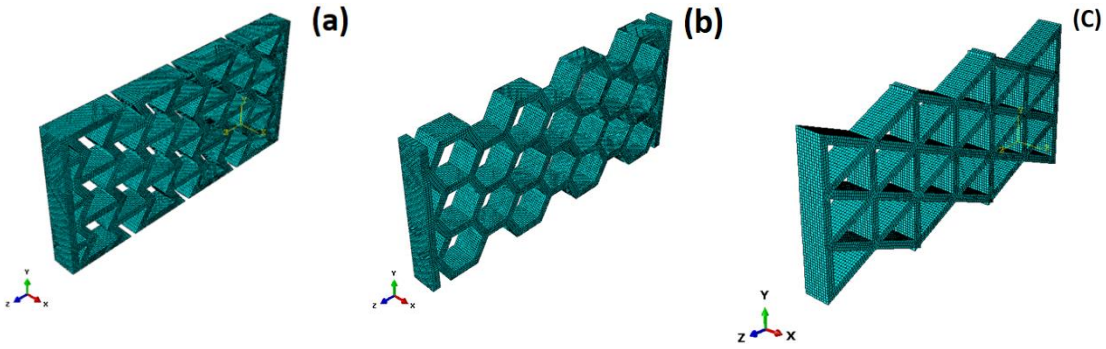

Figure IV.7: Three models of honeycombs (3D) in structured mesh form (a) RE- entrant (b) hexagonal (c) star-fish.

IV.4.1.2. Numerical results and discussion

IV.4.1.2.1.Traction

IV.4.1.2.1.1.Stress analysis

In the scenario of traction along the (z) direction as shown in **Figure IV.8,** stress localization is evident in distinct regions, with stress concentration particularly noticeable at the angle of inclination of cell walls in the RE-entrant, hexagonal, and star-Fish setups. The tensile test (A) highlights the highest stress in a hexagonal cell, reaching 485.6MPa, while for RE-entrant and star-Fish, stress values are 367.4MPa and 212.6MPa, respectively. Notably, the constraint at the top of the star-Fish surpasses that at the lower portion.

Consistent strain patterns across all models are depicted **in Figure IV.9.** During traction, the hexagonal dam undergoes a displacement of 1.056mm, which is higher compared to the displacements of RE-entrant and star-Fish at 0.08335mm and 0.2311mm, respectively. The maximum displacement is observed in the hexagonal configuration.

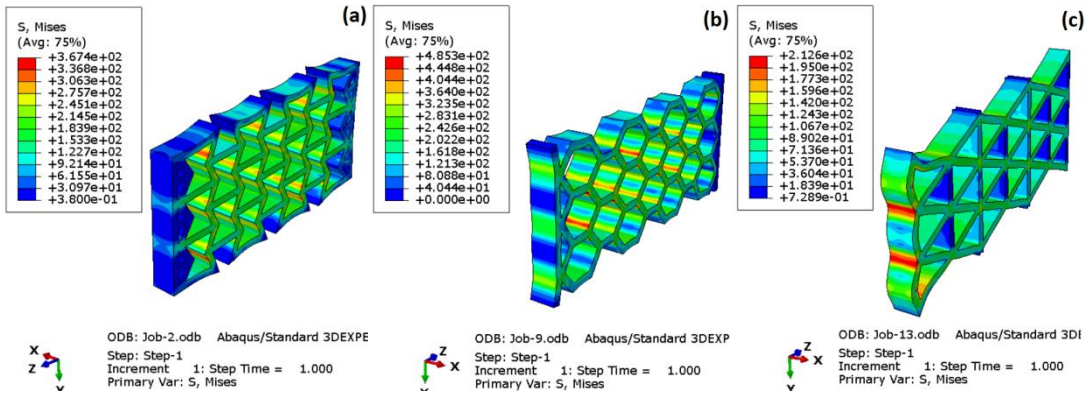

Figure IV.8: Distribution of stresses after traction: a) RE-entrant

b) Hexagonal and c) Star-fish.

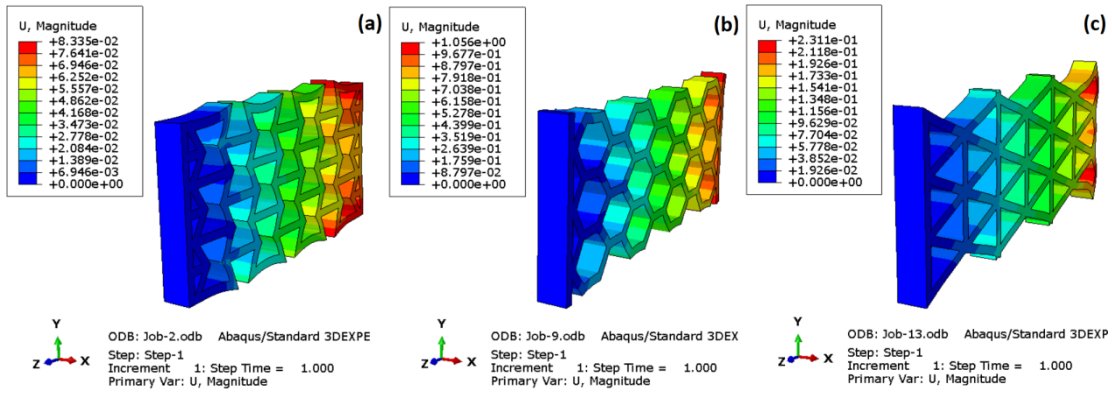

Figure IV.9: Displacement values [mm] for the three models with the applied voltage pressure of50MPa: a) RE-entrant, b) hexagonal and c) star-Fish.

In this study, numerical predictions of bee nib and force-displacement relationships are juxtaposed with the experimental data in **Figure IV.10.** The curves can be delineated into two distinct steps: an initial linear phase where the curves ascend steadily, signifying the specimens' presence in the elastic domain. Subsequently, there is a gradual decrease in the stiffness of the bees, indicating the onset of the plateau stage. The bees eventually reach their peak load, marking the transition into the plastic domain.

Notably, we observe a maximum force of approximately 10^5N for a displacement of approximately 5mm in the honeycomb sandwich (RE-entrant), contrasting with a minimum load of approximately 4×10^4N for a displacement of approximately 3.4mm in the hexagonal honeycomb sandwich. The results show a significant improvement for the honeycomb with a RE-entrant structure, attributed to the structural differences among the honeycomb configurations explored in this article.

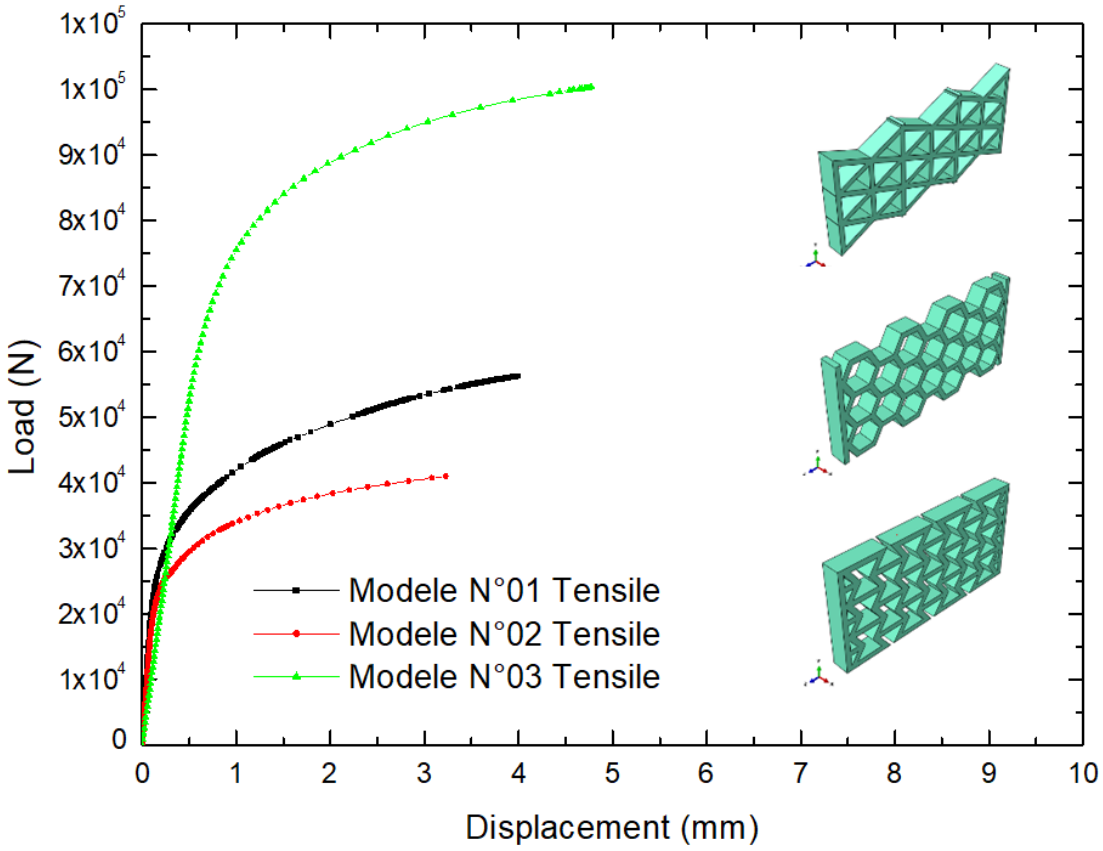

Figure IV.10: Load-displacement curves of the tensile test for the three honeycomb models studied

Table IV.7. Presents the outcomes of the numerical tensile comparison, delineating stresses, displacements, and strains along the three axes (xx, yy and zz) for the hexagonal, RE-entrant, and star-Fish honeycomb structures. Notably, the hexagonal honeycomb exhibited a higher strain rate, while the RE-entrant honeycomb displayed a lower strain rate. Furthermore, stress values were higher for the hexagonal honeycomb and lower for the star-Fish honeycomb. Regarding displacement along the three axes, distinctions were observed among the three honeycomb types.

Table IV.7: Comparison between numerical results for the three specimens on ABAQUS for traction

		Hexagonale	RE-entrant	Star fish
Magnitude (MAX) (mm)	**U_{11}**	7.965E-3	6.515E-4	4.609E-3
	U_{22}	2.253E-1	2.285E-2	4.359E-2
	U_{33}	4.875E-3	1.321E-3	2.377E-4
STRESS (MAX) (MPa)	**S_{11}**	1.41E2	1.448E2	6.680E 1
	S_{22}	3.566E2	4.227E2	1.455E2
	S_{33}	3.377E2	2.651E2	2.086E2
Strain (MAX) (%)	**E_{11}**	2.058E-3	1.389E-4	8.094E-4
	E_{22}	3.927E-3	4.543E-4	1.860E-3
	E_{33}	3.711E-3	3.321E-4	2.376E-3

IV.4.1.2.2. Compression

IV.4.1.2.2.1. Stress analysis

Owing to its robust tensile strength, the stress behavior of all three models—RE-entrant, hexagonal, and star-Fish—under varying loads is depicted in **Figure IV.11.** A detailed comparison of stress results was carried out through digital resolution during compression loading. The numerical analysis showcased that the hexagonal mechanical models led to structural stiffening in the impact region.

Further exploration and understanding of this intricate topic necessitate additional studies employing more sophisticated models to capture realistic constraints. The numerical simulation results,

encompassing load-displacement profiles and damage mapping using ABAQUS, are illustrated in Figure IV.11 for RE-entrant, hexagonal, and star-Fish models.

The performance of these structures was significantly influenced by the structural section. Hexagonal structures (NH) exhibited the most favorable stress performance, recording 488.4MPa, representing a 24.77% increase compared to the lowest stress value observed in RE-entrant (RE-NH) structures (367.4MPa). Conversely, the star-fish sandwich (S-F) demonstrated the lowest impact resistance performance due to minimal deformations and the emergence of buckling phenomena.

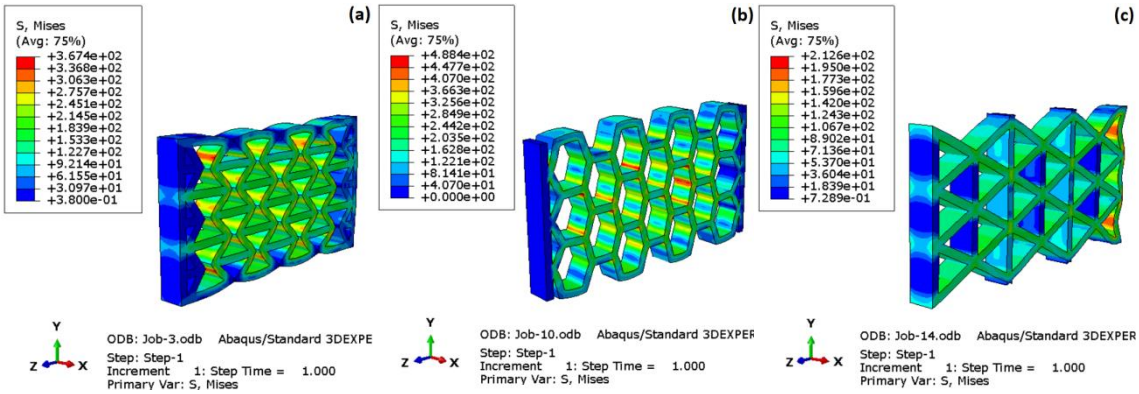

Figure IV.11: Stress distribution after compression :(a) RE-entrant, (b) hexagonal and (c) star-fish.

The deformation phenomenon is evident in Figure IV.12, depicting the simulation results obtained using ABAQUS/CAE software for a sandwich structure model damaged under compression. In Figure IV.12-a, the deformation is shown for the RE-entrant configuration, while Figure IV.12-b illustrates the deformation for the hexagonal model, and Figure IV.12-c presents the deformation for the star-Fish configuration.

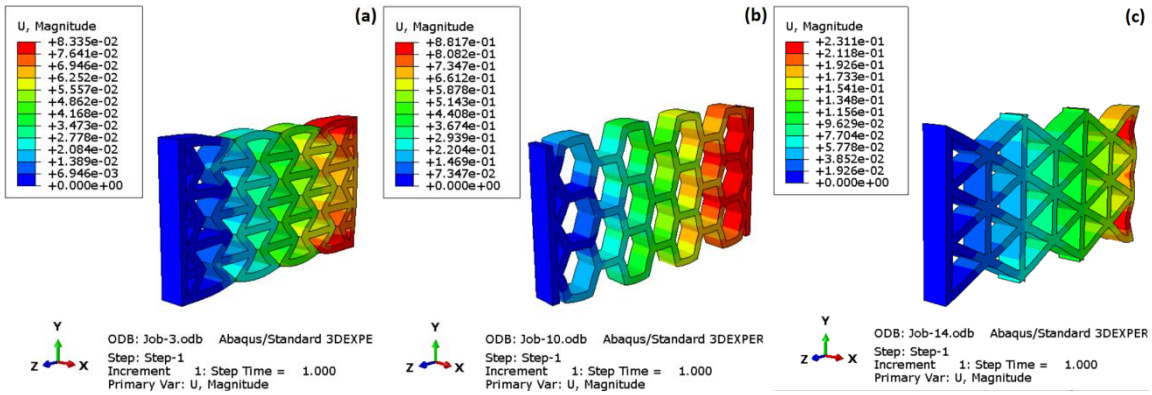

Figure IV.12: The displacement values [mm] for the three models with the applied voltage pressure of50MPa: (a) RE-entrant, (b) hexagonal and (c) star-Fish.

Compression tests were conducted under position control at a travel speed of 23mm/min. The load-displacement curves and strain trajectories for the three honeycomb sandwich models are presented in **Figure IV.13.** Load values are normalized to honeycomb cells in the respective samples. The results indicate that the compressive load can be quantified, and it is associated with the honeycomb shape. For instance, in this study, the honeycomb structure (RE-entrant) recorded a maximum force of approximately 10^5N for a displacement of 6mm. Conversely, the other two honeycomb sandwiches (hexagonal and star-fish) exhibited nearly identical strength levels with similar displacements.

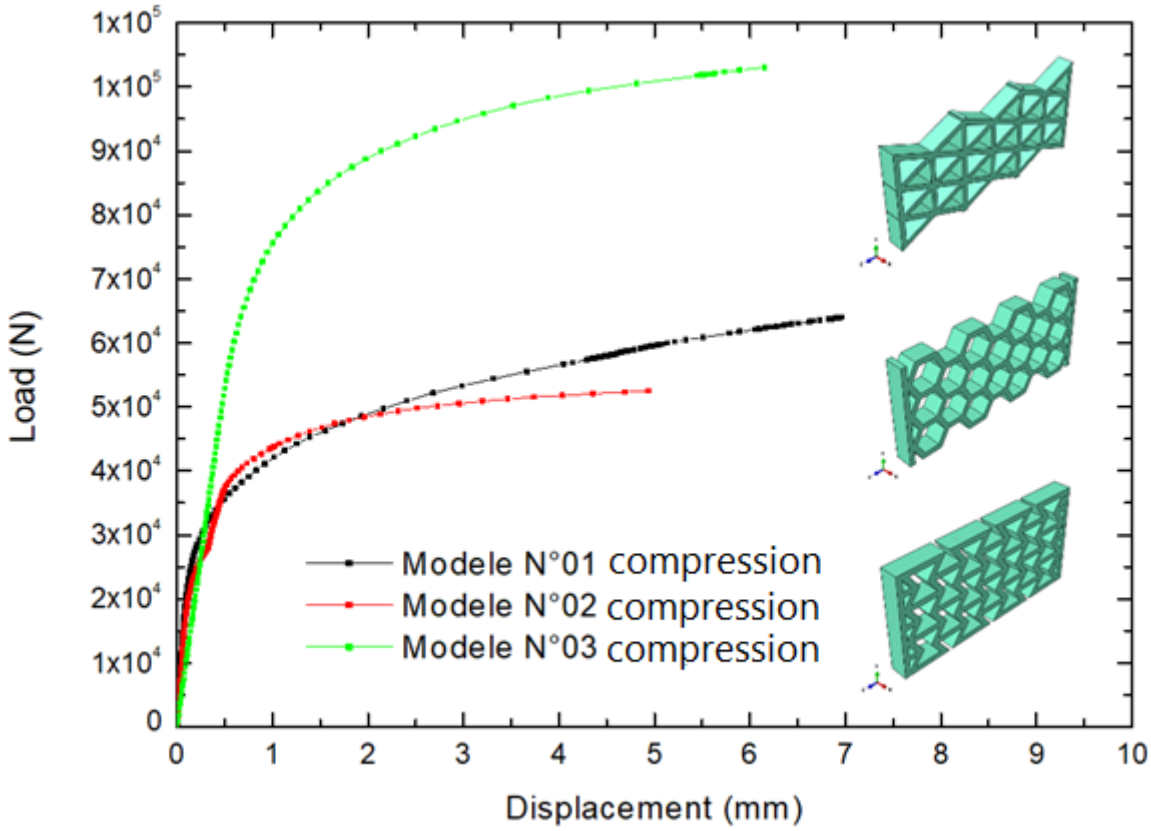

Figure IV.13: Load-displacement curves (Compression) for the three models

Table IV.8. provides a numerical comparison of stress, strain, and displacement during the compression process in Abaqus software. The stress was notably high for the RE-entrant honeycomb, whereas the strain rate and displacement values along the three axes (xx, yy, and zz) were elevated for the hexagonal honeycomb.

Table IV.8: Comparison between numerical results for the three specimens on ABAQUS for compression

		Hexagonal	**RE-entrant**	**Star -fish**
Magnitude (MAX) (mm)	U_{11}	7.965E-3	6.515E-4	4.609E-3
	U_{22}	2.238E-1	2.301E-2	4.343E-2
	U_{33}	8.817E-1	8.012E-2	2.309E-1
STRESS (MAX) (MPa)	S_{11}	2.305E2	8.832E1	5.016E 1
	S_{22}	5.905E2	2.502E2	1.995E2
	S_{33}	1.705E2	1.455E2	4.541E1
Strain (MAX) (%)	E_{11}	2.014E-3	1.412E-4	8.340E-4
	E_{22}	6.634E-3	3.108E-4	2.713E-3
	E_{33}	2.812E-3	2.342E-4	5.940E-4

IV.5. Conclusion:

In conclusion, the comparison between numerical results obtained through finite element analysis using the XFEM technique and experimental values has demonstrated a favorable agreement. The error ratios for maximum stress are found to be less than 3%, indicating a high level of accuracy in predicting the material's response under tensile loading. However, it is important to note that the error rate

increases slightly for Young's modulus, reaching less than 17%, suggesting a somewhat larger variability in predicting this specific mechanical property.

The efficiency of the XFEM technique is underscored in this study, particularly when the mesh of the specimen is well-optimized. This emphasizes the importance of careful meshing practices in achieving reliable and accurate numerical results. The findings suggest that with proper mesh optimization, XFEM can be a robust and efficient tool for predicting the mechanical behavior of materials with geometric discontinuities.

A noteworthy observation from the analysis is the identified high stress concentration around both elliptical and circular notches. Geometric discontinuities, represented by these notches, lead to a reduction in the width of the plate and result in a significant decrease in the maximum tensile stress values. This insight is crucial for understanding how specific geometric features impact stress distribution within the material, providing valuable information for design considerations and material optimization.

In summary, this chapter highlights the success of the XFEM technique in accurately predicting the mechanical response of epoxy-type polymers with different geometric notches. The identified stress concentration effects around notches emphasize the importance of considering geometric factors in material design and structural analysis to enhance the overall reliability and durability of materials in practical applications.

A detailed analysis and objective comparison of recent studies on the application of finite element analysis to honeycomb. The Abaqus/CAE software was used to study the effect of traction and compression on all kinds of honeycombs (RE-entrant, hexagonal and star-fish) and by comparing the simulation results, we came to the following conclusions:

- The localization of the stress occurs at the angle of inclination of the walls of the hive of the three honeycombs under the influence of pressure and traction.

- The loads introduce a more localized deformation in the structure, and therefore an early onset of plasticity and localized instability is expected.

- Honeycomb cell with RE-entrant geometry tends to be more suitable to withstand loads such as traction and compression and it is a comparison between it and the hexagonal honeycomb cell and star-fish. The maximum load was reached at 10^5N for both traction and compression.

- Finally, the honeycomb RE-entrant structure has the best impact resistance during axial impacts (tensile and compression) and this type of structure can be made of aluminum it can work and be used in the equipment of some aircraft, as well as in product packaging, Nevertheless, the use of pure aluminum remains limited due to its poor mechanical properties

CHAPTER V

Output Response Optimization

V.1. Introduction

The final chapter of the thesis thoroughly explores the in-depth analysis, optimization, and modeling of the mechanical behavior, covering both tensile and compression tests, along with water absorption, for bending specimens in diss, sisal, and luffa composites. Cutting-edge methodologies, such as artificial neural networks (ANN) and response surface methodology (RSM), are applied in this section to forecast and optimize the absorption properties and mechanical behavior. Moreover, ANN is employed to foresee the mechanical performance in tensile testing for both fiber-reinforced and non-reinforced epoxy specimens featuring holes.

Utilizing regression analysis, error graphs, and a comparative assessment of experimental and predicted values, this chapter provides valuable insights into the precision and dependability of the developed models. Additionally, it discusses the research findings in connection with previous studies, emphasizing the consistency and significance of these discoveries. This underscores the potential of advanced technologies in predicting and enhancing material properties.

V.2. ANN and RSM method

In the domain of Mechanical/Material Science, Artificial Neural Networks (ANN) and Response Surface Methodology (RSM) are applied in various ways. ANN stands out for predicting material properties, optimizing manufacturing processes, and conducting non-destructive testing, while RSM is valuable for tasks like experimental design, surface modification, and alloy design. When employed in conjunction, these methods synergistically enhance problem-solving capabilities, resulting in precise predictions, efficient processes, and innovative material designs, thus significantly advancing the field. In this study, both ANN and RSM were utilized to predict the mechanical

properties of epoxy specimens based on their geometries and sections. These models serve as tools to comprehend how changes in the epoxy sample's configuration influence its mechanical behavior. The comparative analysis in this study revealed that the ANN model outperformed the RSM model in predicting mechanical properties.

V.2.1. Artificial neural network (ANN) method

Artificial Neural Network (ANN) is a computational algorithm specifically crafted for calculating nonlinear mappings. It emulates the biological nervous system, taking inspiration from nature to replicate its functions [128, 129].**Figure V.1** showcases the computational unit of this artificial neural network, which includes one or two hidden layers, along with input layers where each input xi is represented by a single neuron. The output layer, labeled as y_i, integrates processed information from the inputs using weight values (represented by k) and biases, as outlined in equation 1.**[121].**

$$y_i = \frac{1}{1 + e^{kx_i}} \qquad \textbf{(V.1)}$$

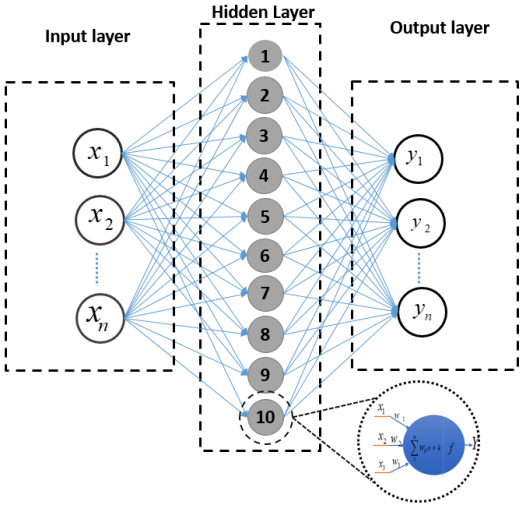

Figure V.1: ANN-N topology

V.2.2. Response surface methodology (RSM) method

Response surface methodology is a technique employed for modeling, analyzing, and simulating problems characterized by multiple response variables and independent variables. It utilizes mathematical, statistical, and graphical methods to construct mathematical models aimed at optimizing experimental processes. These models not only facilitate the optimization of experimental processes but also enable the establishment of correlations between input and response variables observed during experiments[130, 131]. **In Table V.1**, the pertinent parameters, along with their names, are presented, and to model them for obtaining outputs reflecting the mechanical characteristics of the tensile test, the linear and quadratic methods (surface response methodology) were applied. These methods are defined based on the following relationship[132].

$$Y(x) = B_0 + \sum_{j=1}^{k} B_j X_j + \sum_{j=1}^{k} B_{jj} X_j^2 + \sum_{j=1}^{k} \sum_{i\geq 2}^{k} B_{ji} X_j X_i \qquad \textbf{(V.2)}$$

Where Y(x) represents the bound predicted response. In addition, X_i and X_j correspond to the independent variables, while B_0, B_j, B_{jj} and B_{ji} denote a constant, linear first-order interaction and second-order interaction coefficients, respectively**.**

V.3. An Optimizing Epoxy Tensile Properties: ANN vs RSM for epoxy samples

V.3. 1. Response Surface Methodology (RSM) Modeling of Tensile Properties in Epoxy Samples

Table V.2. Presents experimental findings alongside models (ANN and RSM) categorized by two inputs, representing sample geometry and sample cross-sections. The outputs include either Young's Modulus or stress.

Table V.1: RSM factors levels

Symbol	Factor	Unite	Levels		
			Low level (1)	**Intermediate level (0)**	**High level (+1)**
A	**Geometry**	**-**	-1	0	1
B	**Section**	**mm^2**	83.91	92.50	102.00

Table V.2: Experimental and modeling results of stress and Young's Modulus.

N°	Input variables			Output variables					
	Geometry		Specimen section (mm^2)	Maximum Stress (MPa)			Young's Modulus (MPa)		
				EXP	ANN	RSM	EXP	ANN	RSM
1	Hole-notched	-1	102.555	18.404	19.204	19.518	1261.79	1375.474	1311.084
2		-1	97.524	21.060	21.051	20.793	1423.36	1448.134	1410.441
3		-1	83.913	24.221	24.180	24.078	1684.47	1719.382	1671.552
4		-1	102.684	20.391	19.602	19.485	1356.42	1364.197	1308.516
5		-1	90.2979	22.366	22.672	22.567	1526.02	1465.360	1550.464
6	Ellipt	0	88.33	11.008	9.425	12.078	545.09	617.176	760.212
7		0	86.7162	5.6846	10.957	11.79	967.12	953.758	745.283

8		0	84.6945	11.213	12.134	11.425	547.59	617.706	726.357
9		0	86.296	17.404	11.507	11.715	899.84	887.028	741.370
10		0	90.5692	14.171	14.047	12.471	794.25	555.458	780.666
11	**Undamaged specimen**	1	86.31	45.767	41.610	41.899	1858.00	1847.381	1812.549
12		1	85.4642	41.950	41.775	41.396	1836.78	1857.097	1824.658
13		1	87.4324	42.132	41.211	42.566	1713.70	1719.878	1796.414
14		1	87.318	40.133	41.255	42.498	1858.79	1748.445	1798.062
15		1	85.1332	39.576	41.794	41.198	1793.80	1857.939	1829.385

Table V.3: ANOVA of quadratic model obtained for stress and Young's Modulus.

Source	**Sum of Squares**	**df**	**Mean Square**	**F-value**	**p-value**	
(a) ANOVA for Stress						
Model	2375.66	5	475.13	42.93	< 0.0001	**significant**
A-geometry	82.39	1	82.39	7.44	0.0233	
B-section(mm2)	0.8368	1	0.8368	0.0756	0.7895	
AB	3.97	1	3.97	0.3588	0.5639	
A^2	1114.95	1	1114.95	100.74	< 0.0001	**significant**
B^2	0.0028	1	0.0028	0,0003	0.9876	
Residual	99.60	9	11.07			
Total	2475.27	14				
R^2 =0.9598, **R^2** adjusted = 0.9374, **R^2** predicted = 0.9267and **Adequate precision** =14,8008						
(b) ANOVA for Young's Modulus						
Model	3.014E+06	5	6.028E+05	31.40	< 0.0001	**significant**
A-geometry	1.941E+05	1	1.941E+05	10.11	0.0112	
B-section(mm2)	1993.83	1	1993.83	0.1039	0.7546	
AB	10258.86	1	10258.86	0.5344	0.4834	
A^2	1.016E+06	1	1.016E+06	52.91	< 0.0001	
B^2	2.99	1	2.99	0.0002	0.9903	
Residual	1.728E+05	9	19196.36			
Total	3.187E+06	14				
R^2 =0,9458, **R^2** adjusted = 0,9157, **R^2** predicted = 0,8678and **Adequate precision** =12,4394						

To formulate empirical models for mechanical properties and examine the influence of selected parameters, an experimental plan was crafted using the Response Surface Methodology (RSM) technique. Employed for assessing the significance of various factors in a regression model, including quadratic models, Analysis of Variance (ANOVA) was utilized. In the context of a quadratic model that encompasses both linear and quadratic terms, ANOVA plays a crucial role in determining the substantial contribution of the quadratic term to the overall model fit.

The ANOVA table for a quadratic model dissects the total variation in the data into distinct components, each corresponding to the variation explained by the model or its components. This table aids in evaluating the significance of each term (linear and quadratic) in the model and quantifying the extent of variation they contribute. Key components in the ANOVA table include:

- Sum of Squares (SS): Signifying the sum of the squared differences between observed values and predicted values from the model.
- Degrees of Freedom (DF): Representing the number of independent pieces of information available for estimating each component.
- Mean Square (MS): Obtained by dividing the Sum of Squares by its corresponding Degrees of Freedom.
- F-ratio (F-value): Calculated by dividing the Mean Square for a specific component by the Mean Square of the residual (error) term.
- P-value: Reflecting the probability of obtaining an F-ratio as extreme as observed, assuming the null hypothesis is true (i.e., the term does not significantly contribute to the model).

If the p-value linked to the quadratic term (β2) is below a chosen significance level, typically 0.05, it signifies statistical significance. Its incorporation into the model significantly enhances the fit. Conversely, a high p-value suggests the quadratic term's lack of substantial contribution to the model, indicating that a simpler linear model may be more suitable. The ANOVA of a quadratic model evaluates the significance of the quadratic term (x2) and aids in assessing whether its inclusion improves the model compared to a simpler linear version. Response Surface Methodology (RSM), previously utilized in the literature for tensile tests with positive outcomes[133, 134]. was employed in this study. Subsequently, the experimental results underwent analysis using Design-Expert 12 software. The ensuing section and subsections delve into the findings and their implications, aligning with the output responses derived from the analysis.

To establish mathematical relationships between input and output variables of epoxy samples subjected to tensile testing, Response Surface Methodology (RSM) was employed. The data were generated and analyzed using ANOVA variance, as depicted in **Table V.3**, specifically for Young's modulus and constraints. The efficacy of each term was assessed based on its p-value, with smaller p-values indicating more favorable expected results, as demonstrated by our findings (< 0.0001) [135]. ANOVA results highlighted the significance of first-order parameters A (sample geometry), B (section parameter), and AB (product of geometry and section parameters), as well as the square of sample geometry parameter A^2 and the square of sampling section parameter B^2, all exerting a substantial impact on mechanical properties (Young's Modulus and stress). Among these parameters, A^2 (geometry parameter of sample 2) emerged as a particularly crucial predictor of mechanical properties. Overall, the regression models demonstrated a robust fit, exceeding 80%. For Young's Modulus, a correlation coefficient R^2 of 0.95 and an adjusted coefficient R^2 of 0.91 were observed. Stress exhibited a

correlation coefficient R^2 of 0.94 and an adjusted coefficient R^2 of 0.91, indicating excellent results consistent with prior research.

The accuracy of the models for constraints and Young's Modulus was further assessed through graphical representations generated by Design Expert for both actual and predicted values, as illustrated in **Figure V.2 (a-d). Figures V.2 (b-e)** and **V.2 (c-f)** display normal probability with respect to residuals and residuals with respect to predicted values, respectively. These graphs demonstrate that the expected values align closely with the actual values, providing no evidence of uneven or abnormal results.

The equations representing the RSM models, derived from experimental data on sample geometric responses and sample sections, are presented below:

$$\text{Young's Modulus} = 1777.49 - 355.7A - 52.228B + 132.93AB - 627.66A^2 + 1.90B^2 \quad \textbf{(V.3)}$$

$$\text{Stress} = 12.81 + 11.76A + 1.63B + 3.95AB + 20.99A20.0588B^2 \quad \textbf{(V.4)}$$

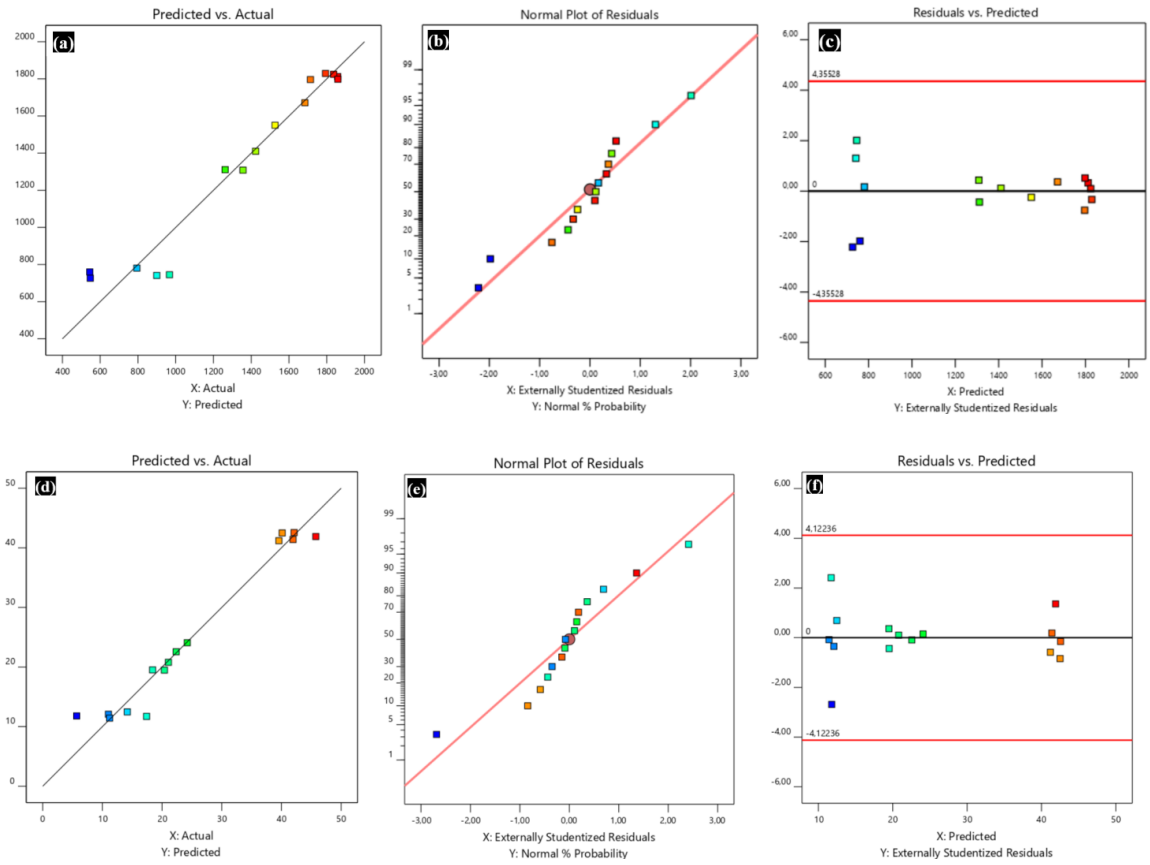

Figure V.2: Plots of stress and Young's Modulus of epoxy samples conductivitymodel; (a)-(d) actual vs. predicted, (b)-(e) normal probability vs. residuals, and (c) -(f) residuals vs. predicted

Figure V.3 illustrates three-dimensional surface diagrams generated by the Design-expert design for Young's Modulus **(Figure V.3-a)**. This visual representation captures the impact of specimen geometry and section characteristics on Young's Modulus. The red area signifies the highest attainable Young's Modulus value, reaching up to 1858.79 MPa, while the blue area represents the lowest value, approximately at 545.09 MPa. **In Figure V.3-b**, stress values are depicted, with the red area indicating the highest stress, reaching 45.76 MPa when the specimen is intact, and the blue area reflecting the lowest stress at 5.68 MPa. **Figure V.4** presents numerical ramps showcasing the optimum stress and Young's Modulus. The maximum desirability was achieved at 0.95, corresponding to a sample section area of 86.36 mm² and

sample geometry of -0.1. The optimal values obtained for the tensile test indicate a stress of 45.76 MPa and Young's Modulus of 1858.79 MPa.

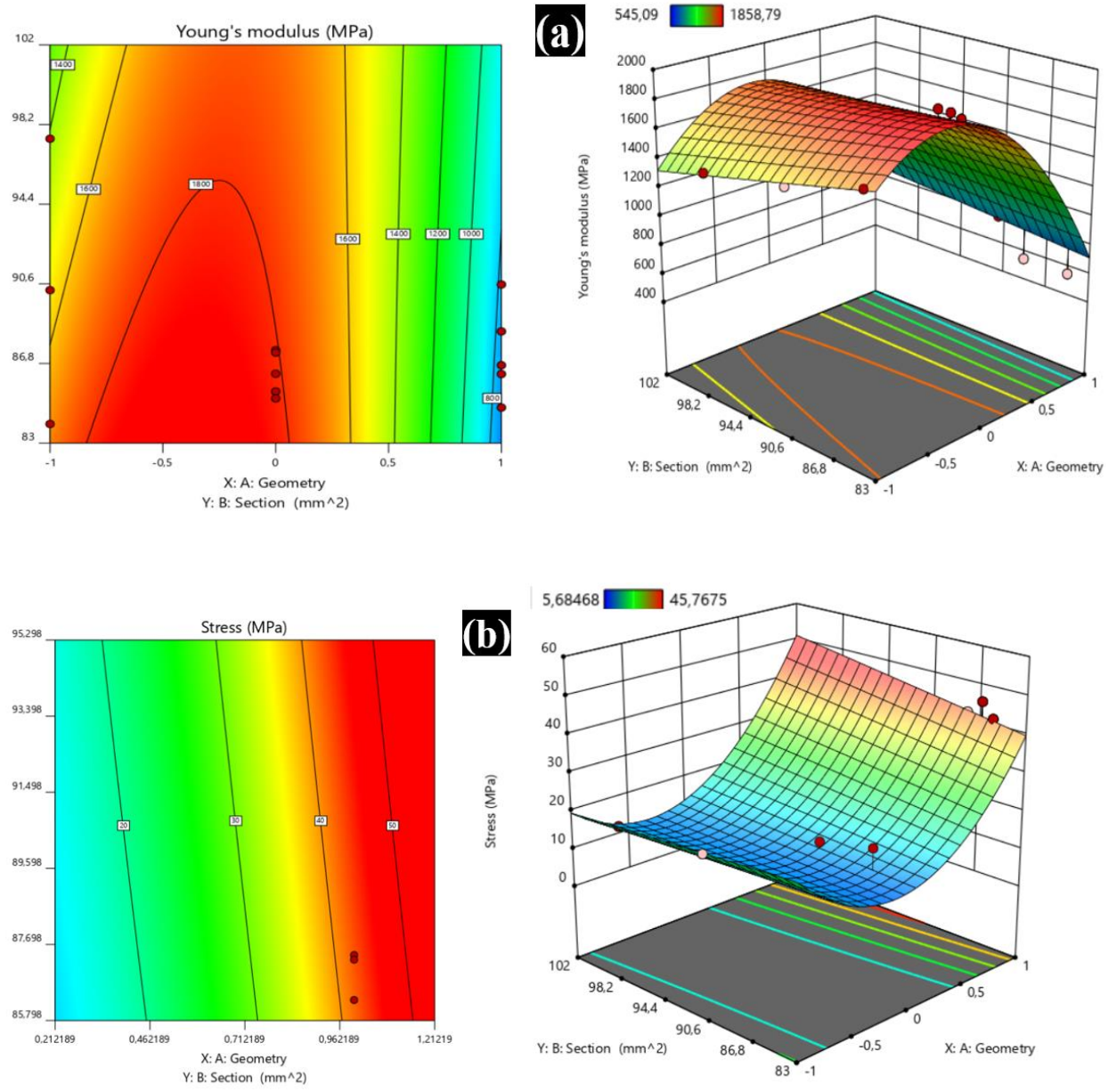

Figure V.3: Contour trace with their 3D response surface plot for (a) Young'sModulus, (b) stress.

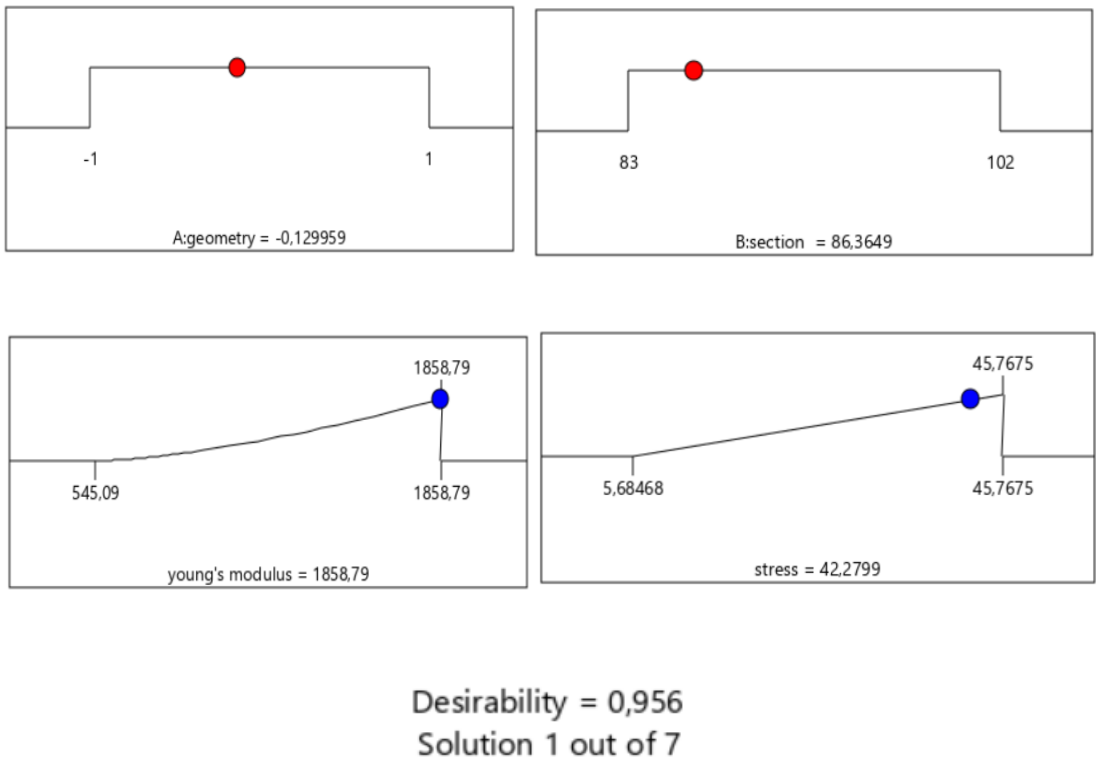

Figure V.4: Numerical ramps for the optimal stress and Young's Modulus

V.3.2. Artificial Neural Networks (ANN) Modeling of Tensile Properties in Epoxy Samples

The ANN (Artificial Neural Network) was chosen for investigating the mechanical properties of Young's Modulus and predicting stress in tensile tests. This is depicted **in Figure V.5**, showcasing a neural network comprising two input units representing sample geometry and section characteristics, two hidden layers, and an output layer for both constraint and Young's Modulus. The formation of this network was based on test data in alignment with statistical analysis.

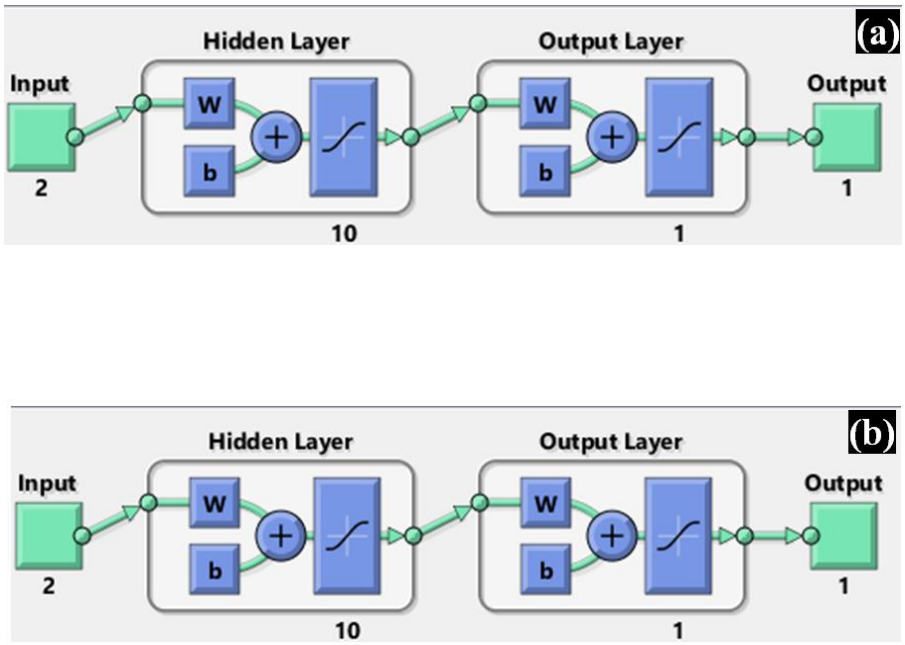

Figure V.5: ANN Structure for :(a) Young's Modulus, (b) stress.

The correlation coefficients (R^2) for Young's Modulus and stress were determined to be 0.984 and 0.981, respectively, as illustrated in **Figure V.6-a**. **Figure V.6-b** visually confirms the high precision of the Artificial Neural Network (ANN), where the experimental and predicted results closely align along the 45° line. This alignment affirms the excellence of the ANN model's predictions across the training, validation, and test datasets. To assess the model's accuracy, mean squared error (MSE) was employed.

As shown **in Figure V.7-a** and **Figure V.7-c,** the randomly distributed data from Table 6 were divided into training (70%), validation (15%), and testing (15%) datasets. The MSE values approach 0 as the accuracy of the ANN model improves. For Young's Modulus, MSE values are approximately 100 for training, testing, and validation, whereas for constraint, MSE values are around 10^2 for training, testing, and validation. In the latter, the convergence of the training, validation, and test lines in **Figure V.7-b**

and **Figure V.7-d** indicates minimal error, emphasizing their proximity to the zero error line and underscoring the effectiveness of the training approach.

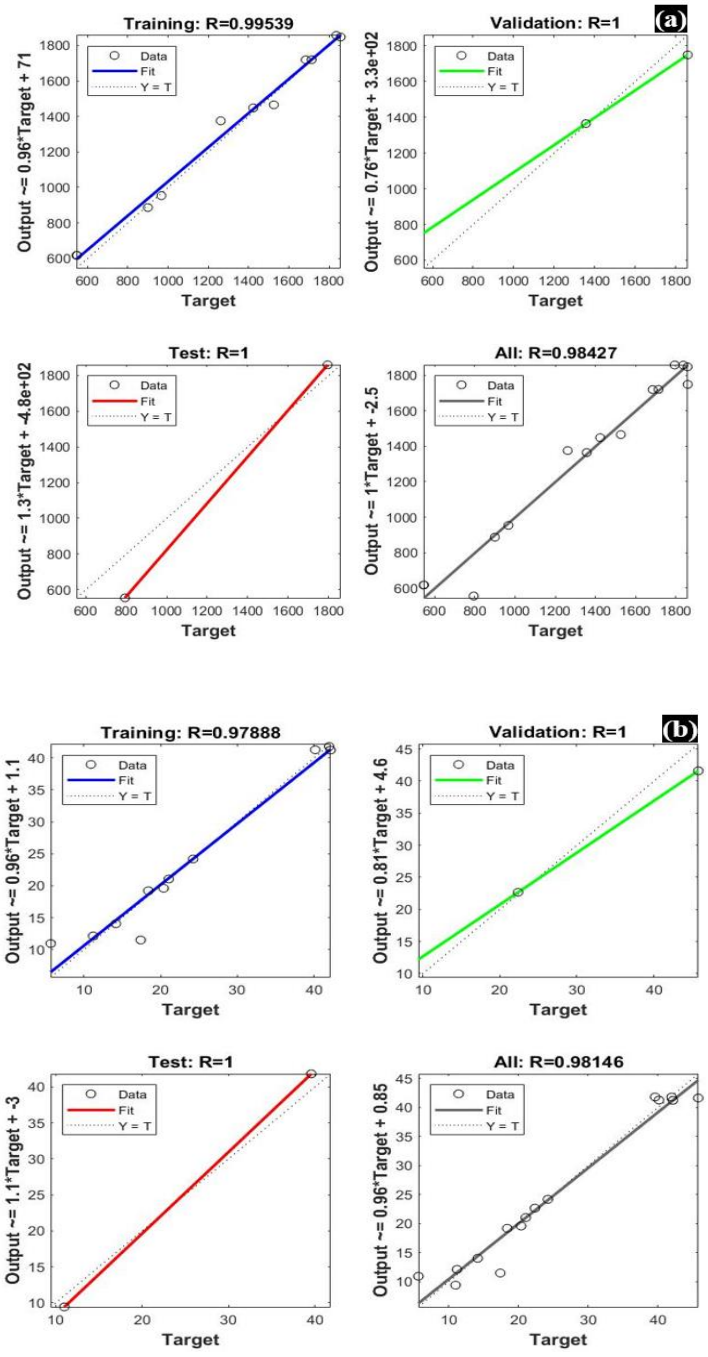

Figure V.6: Predicted values versus experimental values of ANN models for training, validation, testing and all data:(a) Young's Modulus, (b) stress

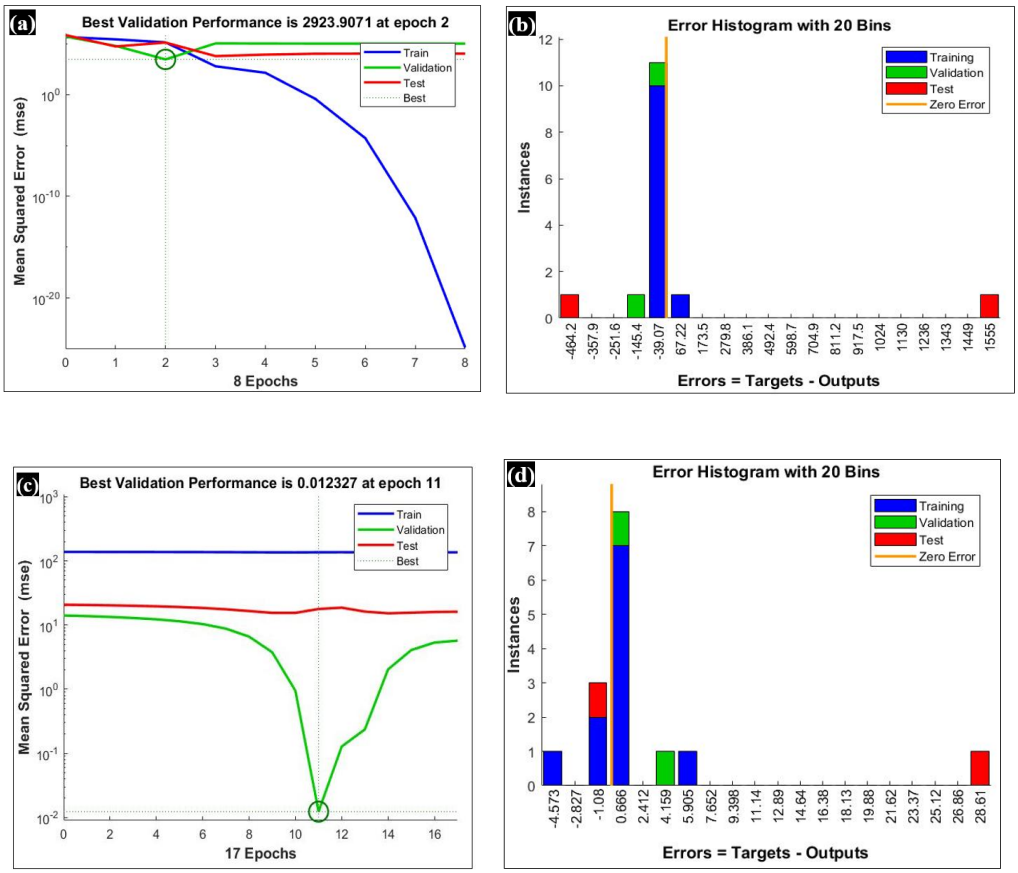

Figure V.7: Mean square error and error histogram variation with respect to time for (a-b) Young‘s Modulus, (c-d) stress.

Table V.4: Allocation both of Young's Modulus and maximum stress used in ANN modeling

		samples	R
Young's Modulus	**training**	11	0.9812
	validation	2	0.9999
	testing	2	1
Maximum stress	**training**	11	0.9734
	validation	2	1
	testing	2	0.9999

V.3.3. Comparison between experimental, ANN and RSM models for samples of epoxy

Figure V.8 provides a side-by-side comparison of results derived from the ANN model, the RSM model, and the experimental outcomes for Young's Modulus and constraint (depicted in **Figure V.8-a** and **Figure V.8-b**, respectively). The findings indicate that both models successfully reproduce the experimental data, with the ANN model standing out for its superior predictive accuracy compared to the RSM model. This underscores the highly accurate prediction capabilities of the ANN model, supported by an overall coefficient of determination of 98% for both Young's Modulus and constraint.

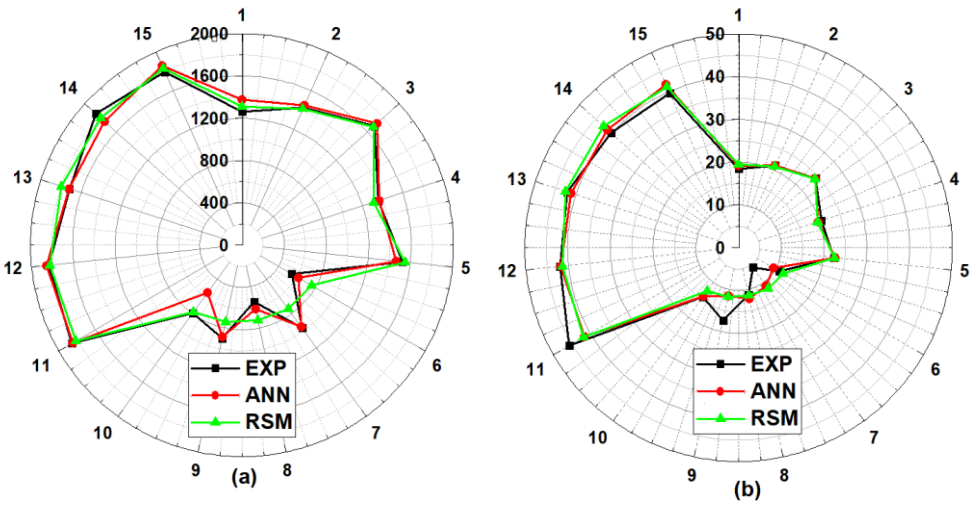

Figure V.8: Comparison between experimental and predicted RSM and ANNmodels tensile data for: (a) Stress - (b) Young's Modulus.

V.4. Response Surface Methodology Modeling for Compression Properties of Honeycomb Samples

The ANOVA results in the **Table .V.5.** indicate that the first-order parameters A (Type of honeycomb), B (Type of fibers), and C (Section), along with the interaction terms AB (Type of

honeycomb multiplied by Type of fibers), AC (Type of honeycomb multiplied by Section), and BC (Type of fibers multiplied by Section), have a significant effect on the mechanical properties (force value). The regression models exhibit a good fit, with values exceeding 90%. For the maximum power value, a correlation coefficient R^2 of 0.88 and an adjusted R^2 coefficient of 0.84 are observed, demonstrating strong results consistent with previous research.

Furthermore, the accuracy of the force prediction can be evaluated through graphs generated by the design expert for each actual or predicted period.

Table V.5: Presents the ANOVA results for the quadratic model obtained in compressive force tests.

Source	Sum of Squares	df		Source	Sum of Squares	df
Model	2,553E+07	9	2,836E+06	22,33	< 0.0001	significant
A-Type of honeycomb	1,643E+07	1	1,643E+07	129,35	< 0.0001	
B-Type of fibers	4,291E+06	1	4,291E+06	33,79	< 0.0001	
C-Section	2,470E+06	1	2,470E+06	19,45	0,0002	
AB	9,335E+05	1	9,335E+05	7,35	0,0117	
AC	5,511E+05	1	5,511E+05	4,34	0,0472	
BC	7,531E+05	1	7,531E+05	5,93	0,0221	
A^2	87280,77	1	87280,77	0,6872	0,4147	
B^2	8870,78	1	8870,78	0,0698	0,7936	
C^2	4472,03	1	4472,03	0,0352	0,8526	
Residual	3,302E+06	26	1,270E+05			
Cor Total	2,883E+07	35				
Std. Dev=356,37				**R^2**=0,8855		
Mean=1215,64				**Adjusted R^2**=0,8458		
C.V. %=29,32				**Predicted R^2**=0,7434		
Adeq Precision=18,2486						
Epoxy, palm, jute, and luffa are assigned the symbols 1, 2, 3, and 4, respectively.						
Hexagonal, Re-entrant, and Star-fish are assigned the values 1, 2, and 3, respectively.						

Force (N) =1 110.63 + 827.334 * A + 463.193 * B + 320.799 * C + 264.595 * AB + 185.596 * AC + 237.653 * BC + 104.451 * A^2 + 35.3193 * B^2 + 23.6433 * C^2 (V.5)

Figure V. 9, 10 and **11** illustrate 3D compression test plots of honeycomb specimens for various fiber geometries (hexagonal, RE-entrant c, star-fish) utilizing jute , luffa, and date palm fibers in the Epoxy-blended biocomposite. The plots showcase the increased force associated with different fiber types (jute, luffa, and date palm), each corresponding to distinct honeycomb structures. These surface diagrams assist in predicting the force increase during compression across the experimental area based on the input parameters.

The findings suggest that enlarging the cross-section of the composites results in higher force values. Particularly, at the star-fish honeycomb, the force reaches 3573.20952 N. Additionally, the type of fiber significantly influences the maximum force, with values of 1642.32898 N for epoxy samples without fibers, 2254.560885 N with date palm fibers, and 2898.187732 N for jute fibers. The highest force is observed at 3573.209 N for date Luffa. These observations are consistent with previous research[136, 137].

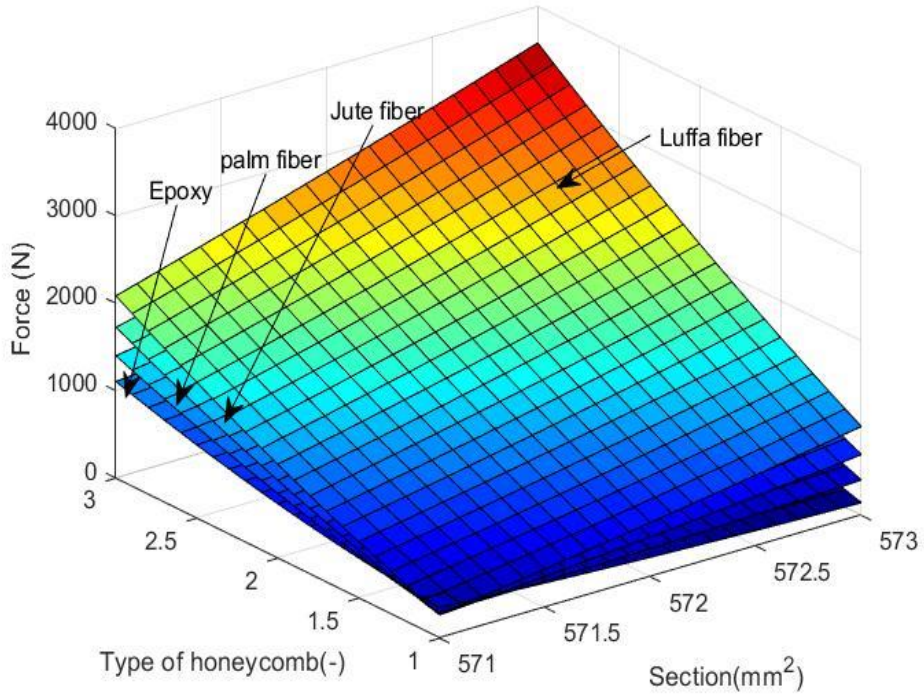

Figure* V. *9: Illustrates the impact of honeycomb type and cross-sectional variation on the compressive force in tests conducted at Epoxy, palm, jute and luffa fiber.

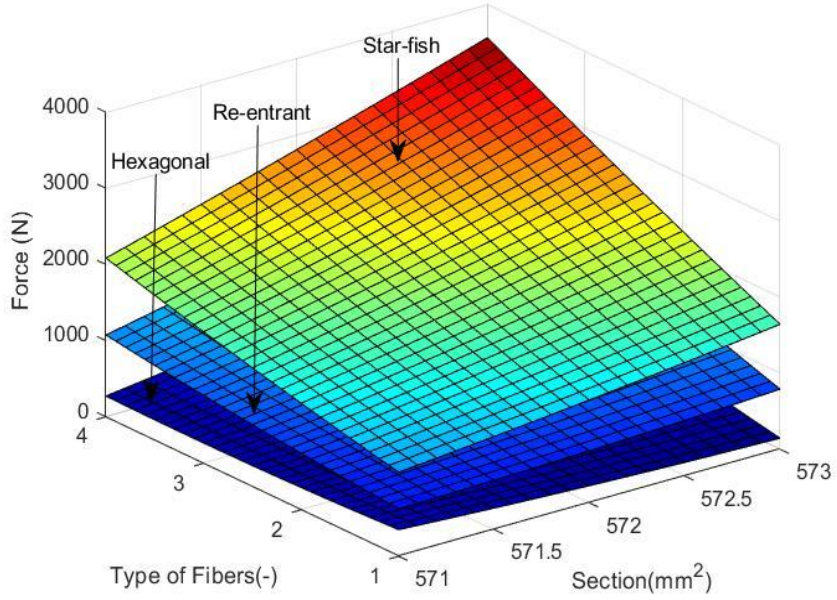

Figure V. 10: illustrates the impact of fibers type and cross-sectional variation on the compressive force in tests conducted at hexagonal, re-entrant, and star-fish.

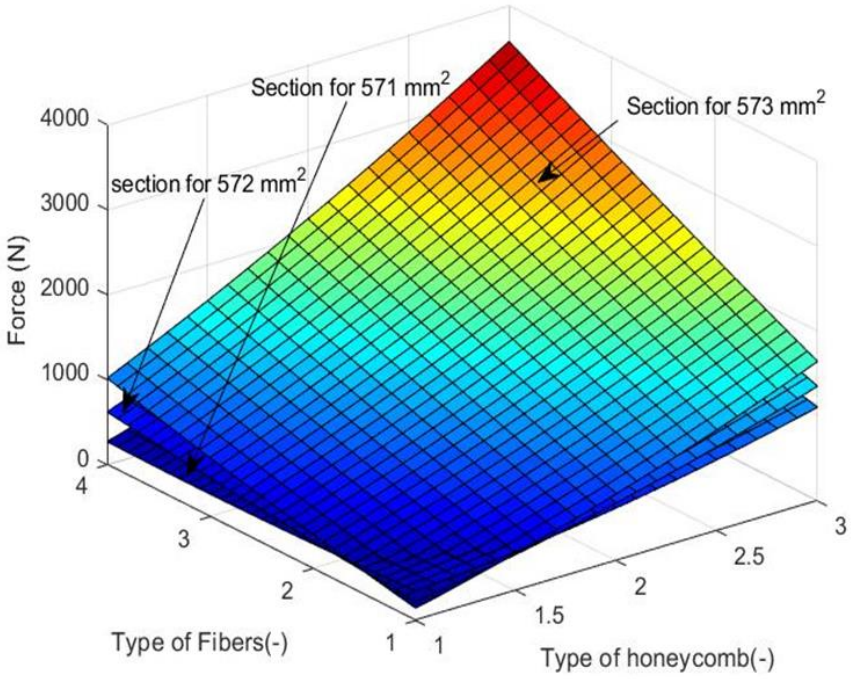

Figure V. 11: Illustrates the impact of fibers type and honeycomb type variation on the compressive force in tests conducted at section 572 mm^2, 571mm^2 and 573mm^2.

The analysis of bio-composites was performed using the Design-Expert software, which recommended employing statistically relevant quadratic models. The plot in **Figure. V. 12.** illustrates the correlation between residual probability and the comparison of predicted versus experimental force values in compression testing of honeycomb specimens. This analysis takes into account various input parameters such as honeycomb type, cross-sections, and the type of fibers utilized in the bio composites. **In Figure V. 12-a**, it is evident that the anticipated outcomes from the Response Surface Methodology (RSM) closely match and resemble the experimental results of the compression test across the 36 represented samples. The findings indicate an excellent fit of the regression model, with predicted values statistically akin to experimental values within an 88% confidence interval, as shown in **Figure V. 13**.

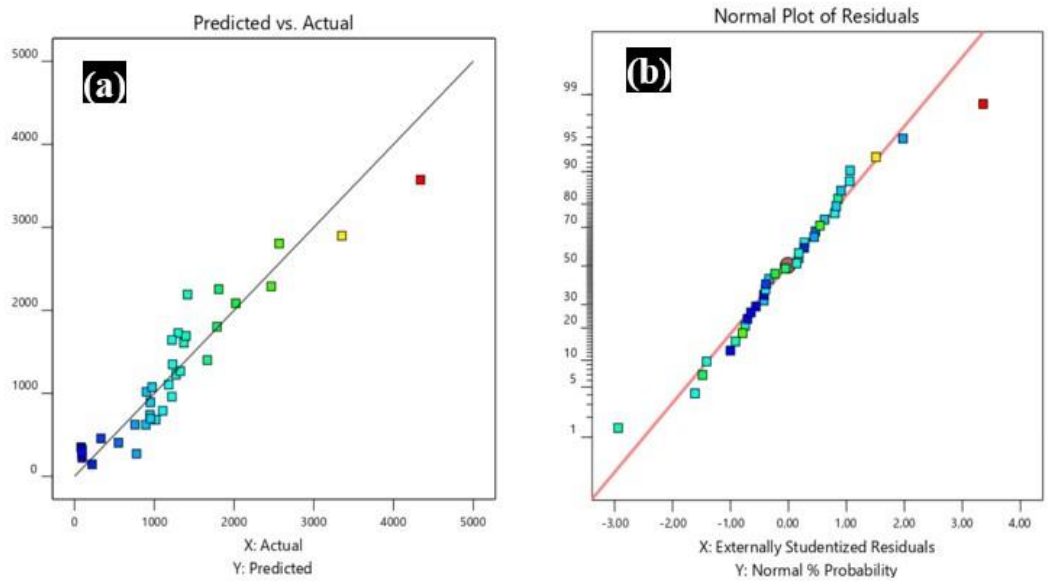

Figure V.12: Presents: (a) Deviations in normal probability distribution for force of compression in bio-composites across all honeycomb types and (b) A comparison between anticipated values and actual values.

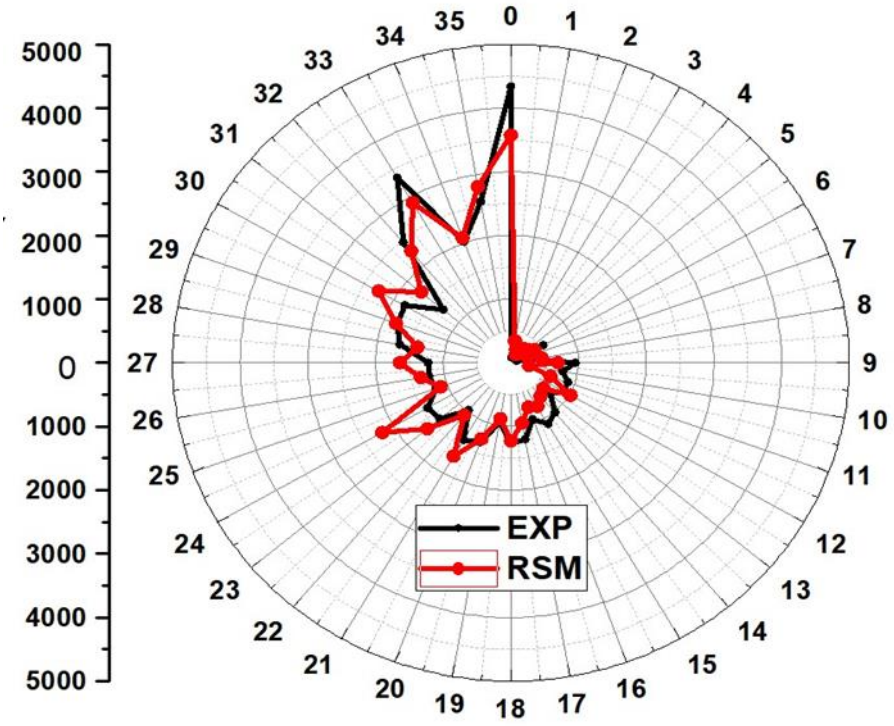

Figure V.13: Comparison between experimental and RSM model for samples of honeycomb of bio composite for results of compression

V.5. Optimization and modeling of the absorption behavior in bending test samples using (RSM)

The overall model demonstrates a high level of significance ($p < 0.0001$), indicating that at least one factor or their interactions have a substantial impact on the response variable. A closer look at **Table V.6,** reveals that A (Time), B (Type of fiber), and C (Rate of fiber) are individually significant with p-values < 0.0001, contributing 7%, 18%, and 54%, respectively, to the overall variability of the model. Among the interactions, AC, BC, A^2, and B^2 also display significant effects ($p < 0.0001$), contributing 1%, 13%, 0.5%, and 4.5%, respectively, to the model's

variability. Conversely, interactions like A.C and C^2 are deemed insignificant and do not exert a notable influence on the model.

Within the complex landscape of data analysis, the Adjusted R^2 value (0.945) and the predicted R^2 value (0.947) seamlessly align, providing strong evidence of the model's remarkable adequacy. In conclusion, it is unmistakable that factors A (Time), B (Type of fiber), and C (Rate of fiber) significantly contribute to the model, while the remaining factors and interactions do not significantly impact the outcome.

Table V.6: Displays the results of the Analysis of Variance (ANOVA) conducted on the quadratic model applied to assess water absorption in bio-composites

Source	Sum Of Squares	Df	Mean Square	F-Value	P-Value		Contribution %
Model	10277.92	9	1141.99	811.68	< 0.0001	significant	
A-Time	742.31	1	742.31	527.60	< 0.0001	significant	7%
B-Type of fiber	1960.66	1	1960.66	1393.56	< 0.0001	significant	18%
C-Rate of fiber	5827.73	1	5827.73	4142.12	< 0.0001	significant	54%
AB	6.97	1	6.97	4.96	0.0266		0%
AC	90.33	1	90.33	64.20	< 0.0001	significant	1%
BC	1409.09	1	1409.09	1001.52	< 0.0001	significant	13%
A^2	47.19	1	47.19	33.54	< 0.0001	significant	0.5%
B^2	478.41	1	478.41	340.03	< 0.0001	significant	4.5%
C^2	4.31	1	4.31	3.06	0.0809		0%
A-Time	543.08	386	1.41				
B-Type of fiber	10821.00	395					
d. Dev.	1.19		**R^2**		0.9498		

Mean	7.00	**Adjusted R^2**	0.9486
C.V. %	16.96	**Predicted R^2**	0.9474

Water absorption =9.64+2.34A+2.75B+4.70C+0.2752AB+0.9725AC+2.78BC-1.11A2-2.33B^2-0.2535C^2 **(V.6)**

Figure V. 14, 15 and **16** exhibit surface 3D plots illustrating the water absorption characteristics of Sisal, Diss, and Luffa fibers in the bio-composite. These visual representations depict the variations in water absorption concerning the rate of fiber for different fiber types (Sisal, Diss, and Luffa) over various absorption durations. The surface plots serve as effective tools for predicting water absorption trends within the experimental context.

The findings suggest that an increase in the fiber content within the composite corresponds to a higher percentage of water absorption. Specifically, the incorporation of Luffa fiber results in the highest absorption rate, reaching 19.75% at a 25% ratio. Furthermore, the type of fiber significantly influences the absorption ratio, with Diss fiber registering a ratio of 16.28%, and Sisal fiber at 8.15%, both at the same 25% ratio. Additionally, time plays a notable role in water absorption, with the peak absorption rate observed on day 44. These observations align with previous research, as demonstrated by Makhlouf et al.[138]and Quiles-Carrillo [139], who reported an increased absorption rate with a higher percentage of fiber in the compound at room temperature.

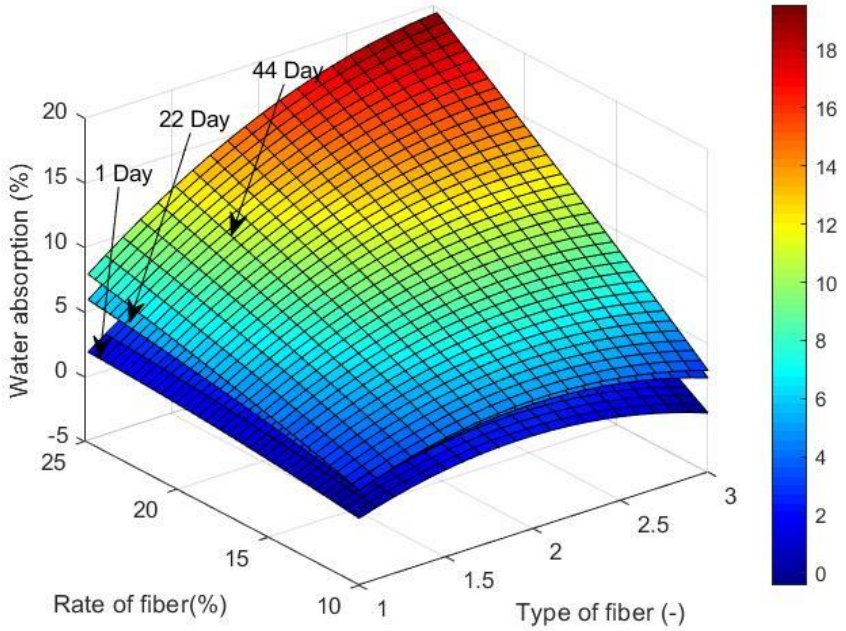

Figure V.14: Effect of Rate of fiber and Type of fiber on water absorption for 1 day, 22 days and 44 days

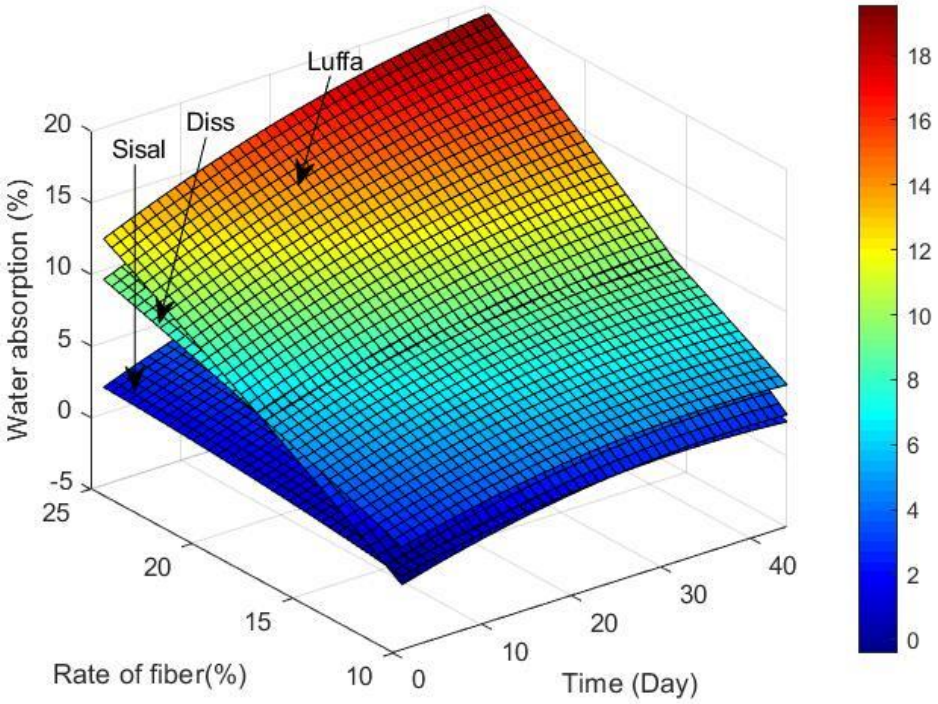

Figure V.15: Effect of Rate of fiber and Time on water absorption for Sisal, Diss and Luffa

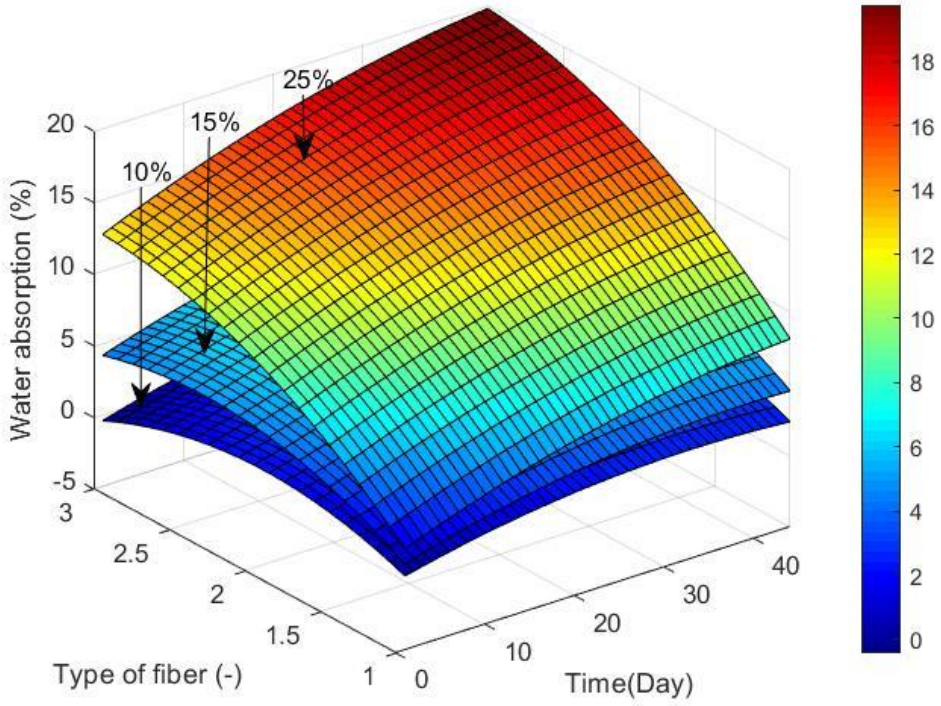

Figure V. 16: Effect of Type of fiber and Time on water absorption for 10% , 15% and 25%

The assessment of bio-composites involved the use of Design-Expert software, which recommended the application of statistically relevant quadratic models. **Figure. V. 17,** portrays a point cloud illustrating the correlation between the probability of residues and the predicted versus experimental values of water absorption. This analysis takes into consideration variables such as Time of absorption, Type of fiber, and Rate of fiber used in bio-composites. In Figure **Figure. V.17-a**, the normal probability curve for water absorption shows that the residues conform to a straight line, indicating well-distributed errors. The outcomes suggest a strong fit of the regression model, with predicted values statistically resembling experimental values within a 94% confidence interval, as depicted in **Figure.V. 13-b.**

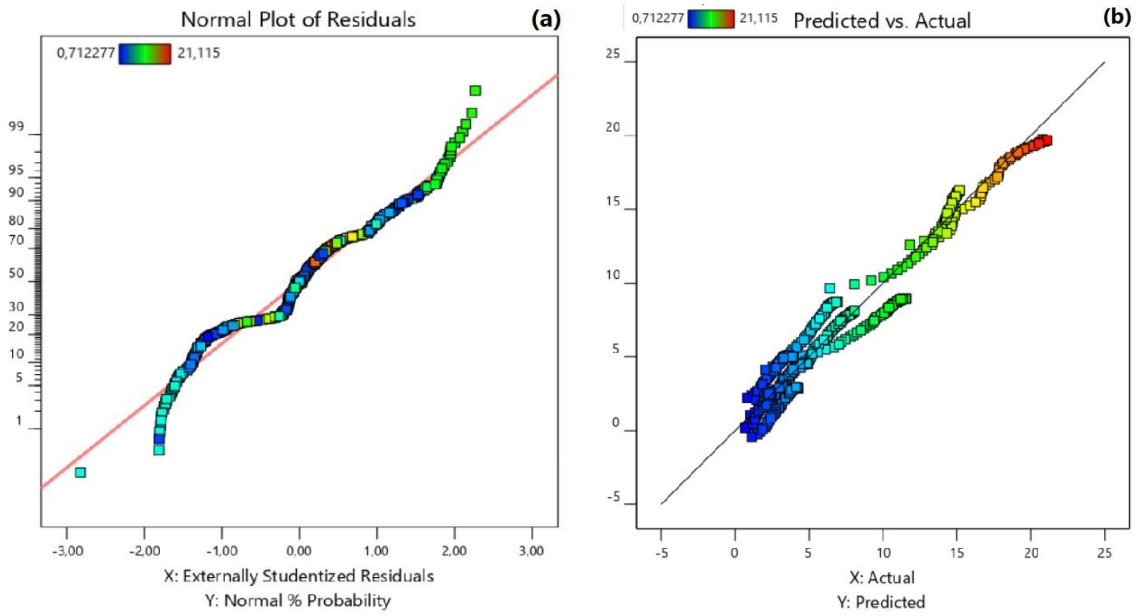

Figure V. 17:(a) Comparison of anticipated values with actual values and (b) Normal probability distribution deviations for water absorption in bio-composites of all fiber types

V.6. Optimization and modeling of tensile test samples using (RSM and ANN)

V.6.1. Comparison of two models (ANN and RSM)

V.6.1.1. Artificial Neural Network (ANN)

Table V.7 presents the experimental results for stress and Young's modulus obtained from 36 tensile samples, alongside the prediction results from both the ANN and RSM models. Notably, the prediction errors for the constraint and Young's modulus are relatively minimal in the case of the ANN model, indicating its superior performance with reduced errors compared to the RSM model. **Figure V.18** provides a visual representation of the architecture of the developed ANN model for stress and Young's modulus prediction. This two-layer backpropagation neural network is configured with 3 inputs and 2 outputs, featuring 10 hidden neurons. The activation function utilized in the model is a combination of the Tansig function. For training and learning both outputs (stress and Young modulus), the TRAINLM and LEARNGDM functions were

employed. The model underwent training and testing using the dataset of 36 collected data points.

Table V.7: Experimental results and for maximum stress and Young's modulus.

N°	Input variables			Output variables					
	Time (h)	Fiber rate (%)	Specimen Section (mm^2)	Maximum Stress (Mpa)			Young's Modulus (Mpa)		
				EXP	ANN	RSM	EXP	ANN	RSM
1	0	15%	102.231	18.545	17.781	19.090	1467.31	1418.865	1600.77
2	0	15%	103.842	18.169	18.549	18.531	1489.18	1478.381	1496.96
3	0	15%	103.070	18.162	18.200	18.782	1497.73	1450.651	1545.43
4	24	15%	094.462	08.229	09.254	14.233	0818.25	0849.484	1384.68
5	24	15%	099.503	10.423	09.992	09.554	0822.54	0865.102	890.11
6	24	15%	101.309	09.913	10.451	08.285	0973.45	0891.018	737.43
7	96	15%	113.926	17.487	17.625	12.815	1362.97	1276.748	991.10
8	96	15%	106.372	15.766	15.464	17.577	1443.28	1364.195	1558.86
9	96	15%	104.065	13.548	13.776	19.778	1331.17	1307.753	1777.25
10	0	20%	103.458	16.569	19.450	18.379	1418.07	1406.658	1535.30
11	0	20%	098.980	18.107	18.293	19.210	1625.35	1573.543	1699.80
12	0	20%	094.608	17.768	17.011	21.301	1637.12	1626.314	1936.91
13	24	20%	097.894	20.420	20.617	08.131	1725.98	1758.507	741.03
14	24	20%	099.150	20.511	20.595	07.432	1874.54	1719.039	669.28
15	24	20%	094.798	21.548	20.627	10.283	1913.96	1816.545	944.48
16	96	20%	108.448	18.922	19.441	13.261	1569.29	1525.658	1103.52
17	96	20%	108.837	19.900	19.471	13.090	1715.42	1511.645	1085.54
18	96	20%	101.476	19.925	19.894	18.122	1733.26	1690.806	1527.30
19	0	25%	091.505	14.066	14.122	20.128	1457.11	1501.285	1892.58
20	0	25%	102.952	15.511	15.345	18.127	1467.17	1505.281	1690.97
21	0	25%	103.878	15.551	15.497	18.334	1501.13	1517.495	1697.31
22	24	25%	102.287	16.964	17.053	04.752	1468.41	1484.936	518.82
23	24	25%	117.376	16.128	16.097	11.751	1376.92	1434.754	858.67
24	24	25%	104.166	15.681	16.743	04.810	1498.34	1509.617	512.05
25	96	25%	118.057	09.452	11.064	11.941	0615.29	0695.361	1037.17
26	96	25%	107.189	10.950	10.813	11.06	803	823.480	989.11
27	96	25%	101.232	14.203	14.202	13.87	1119.72	1117.223	1161.02
28	0	30%	104.509	15.714	15.758	18.79	1662.49	1678.190	2043.08
29	0	30%	100.924	15.282	15.450	17.14	1806.44	1738.654	1903.29
30	0	30%	099.973	15.282	15.351	16.84	1701.75	1750.712	1874.74
31	24	30%	115.121	16.641	16.635	12.01	1674.3	1686.817	1344.09
32	24	30%	122.286	16.479	16.408	21.48	1539.67	1588.400	2006.97
33	24	30%	109.337	15.615	16.580	6.83	1708.52	1767.398	957.11
34	96	30%	115.706	10.950	11.060	10.72	1554.31	1561.272	1251.85
35	96	30%	121.494	13.255	14.907	15.05	1609.13	1603.853	1616.36
36	96	30%	121.491	16.556	14.904	15.04	1587.15	1603.843	1616.14

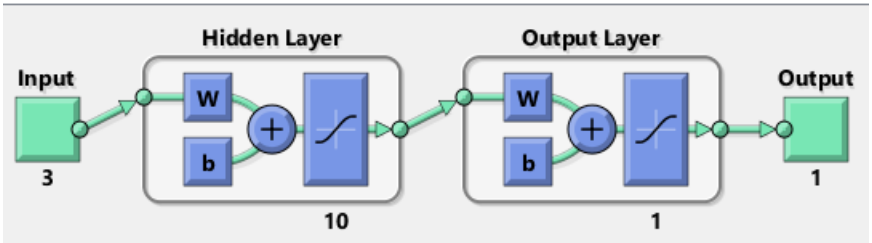

Figure V.18: ANN Structure for tensile strengths

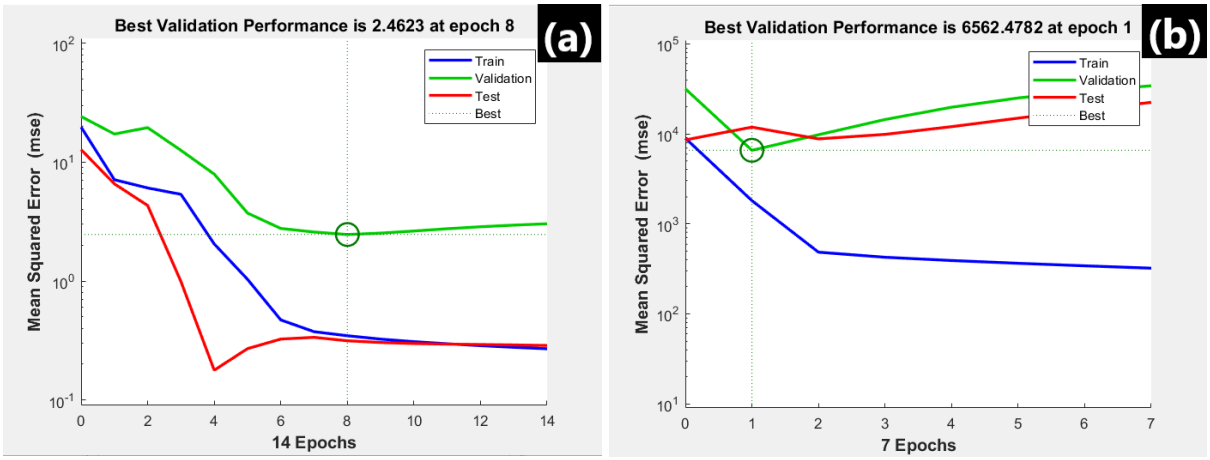

Figure V. 19: Square error during the epochs for: a) maximum stress, and b) Young's modulus

As depicted in **Figure V.20** below, the dotted line represents the optimal correlation achievable, while the thick solid lines depict the actual correlation between the target values and the output values. On the x-axis, we find the target data values derived from the experimental stress and Young's modulus values, and on the y-axis, the stress and Young's modulus values predicted by the ANN after training. The R^2 training values for stress and Young's modulus stand at approximately 0.99, indicating a commendable performance of the Artificial Neural Network (ANN) model. Specifically, the R^2 is 0.97 for stress prediction and 0.98 for Young's modulus prediction.

The overall performance of the ANN model is assessed across training, test, and validation datasets, resulting in R^2 values of 0.98, 0.96, 0.95, and 0.97 for stress (depicted in **Figure V.20-a**). Similarly, for Young's modulus, the corresponding R^2 values across training, test,

and validation datasets are 0.99, 0.96, 0.98, and 0.98, as illustrated in Figure V.20-b.

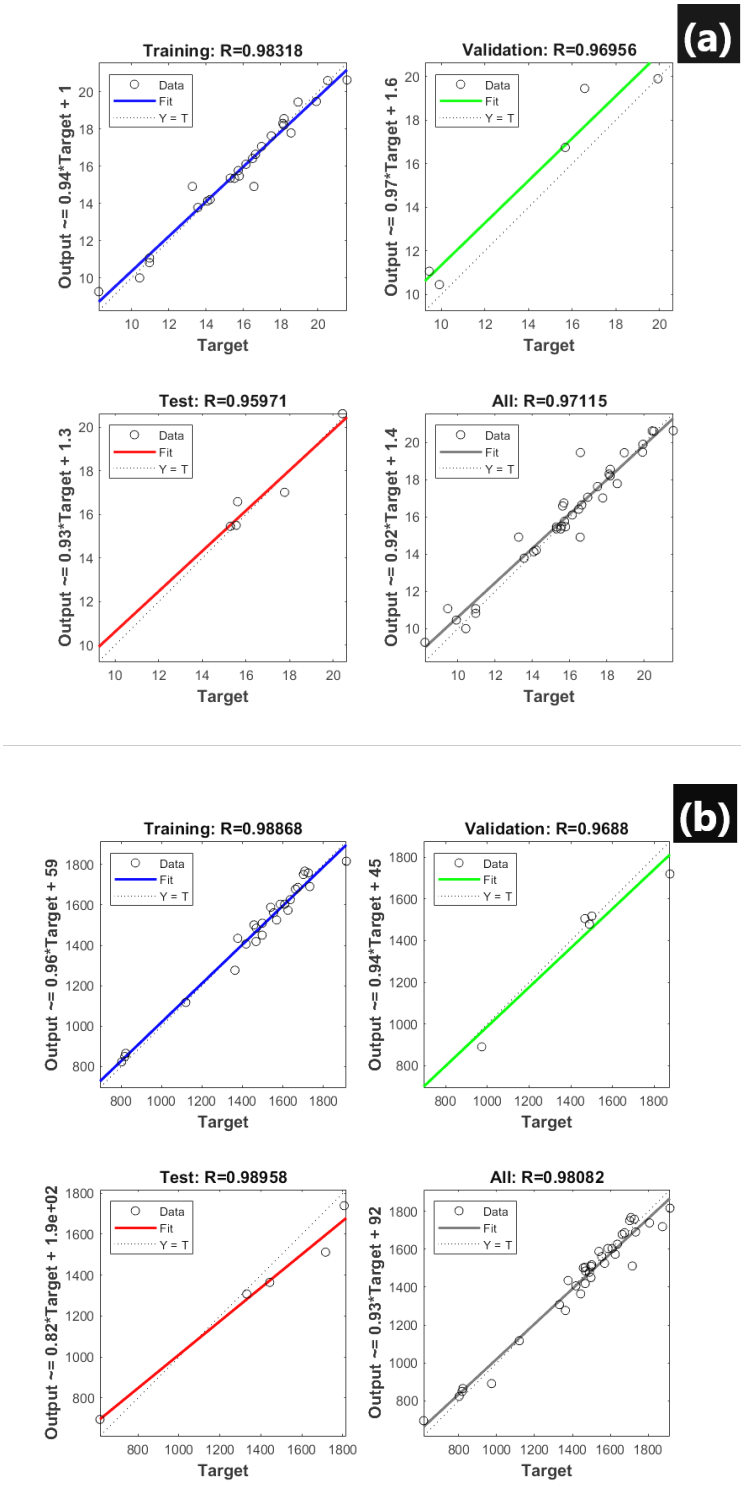

Figure V. 20: ANN modeling results for a) maximum stress, and b) Young's modulus

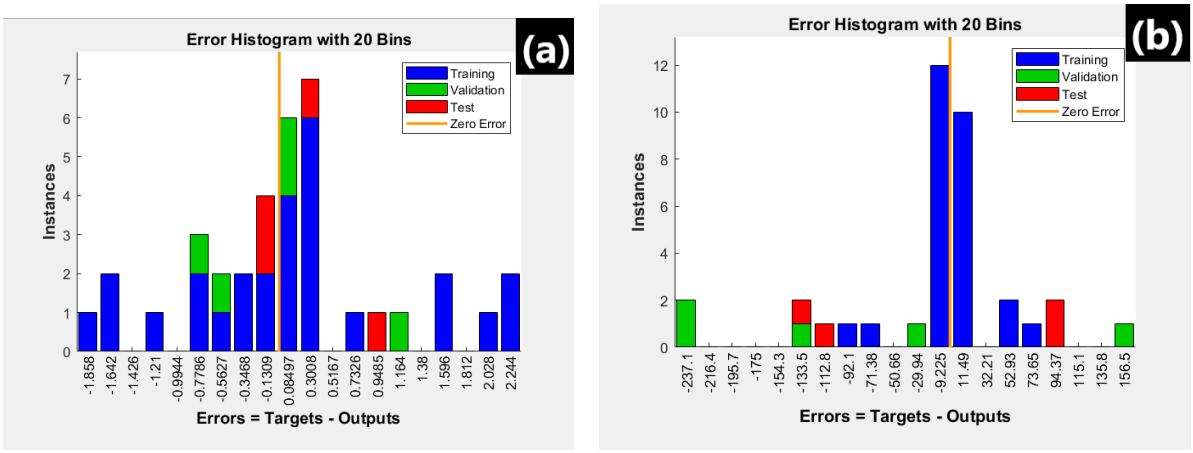

Figure V. 21: Graphic representations of ANN errors by histogram for: a) maximum stress and b) Young's modulus

The error histograms for both networks are show in Figure. V. 21. where:

$$ERR_{stress} \in [-0.7786 - 0.3308]$$

$$ERR_{\substack{young's \\ modulus}} \in [-9.25 - 11.49]$$

Table V.8: Allocation of stress and Young's modulus used in this study for ANN modeling

		samples	MSE	R
maximum stress	**training**	27	1.27956	0.939446
	validation	5	0.45036	0.983778
	testing	4	0.20605	0.966770
Young's modulus	**training**	27	1520.20647	0.992272
	validation	5	22716.61144	0.820958
	testing	4	17600.81339	0.976593

Table V.7 displays the output parameters, namely maximum stress and Young's modulus, derived from various experiments conducted under different input parameters such as Time, Fiber rate, and Specimen section. In this experiment, a Response Surface Methodology design was employed, resulting in a quadratic model with 36 trials. The outcomes were obtained by analyzing the impact of the input parameters on the output parameters. The equations of the

predicted model were formulated, allowing for the estimation of responses. The mathematical representation of the model is provided in **Table V.8** for maximum stress and Young's modulus, where the factors Time, Fiber rate, and Specimen section are denoted as A, B, and C, respectively.

V.6.1.2. Response Surface Methodology (RSM)

Table V.9: ANOVA analysis of variance for stress and Young's modulus

Source	**Sum of Squares**	**df**	**Mean Square**	**F-value**	**p-value**	
(a) ANOVA for Stress						
Model	8209.16	9	912.13	21.60	< 0.0001	**significant**
A-Time	76.59	1	76.59	1.81	0.1893	
B-Fiber rate	61.81	1	61.81	1.46	0.2368	
C-Specimen Section	28.36	1	28.36	0.67	0.4197	
AB	40.66	1	40.66	0.96	0.3352	
AC	68.80	1	68.80	1.63	0.2127	
BC	37.62	1	37.62	0.89	0.3536	
A^2	2146.16	1	2146.16	50.83	< 0.0001	
B^2	0.10	1	0.10	0.002	0.9610	
C^2	71.26	1	71.26	1.69	0.2049	
Residual	1140.10	27	42.23			
Lack of Fit	113.65	26	43.64	8.01	0.2733	**not significant**
Pure Error	5.45	1	5.45			
Total	9349.26	36				
Std. Dev=6.50		**R^2**=0.8781				
Mean =15.78		**Adjusted R^2**=0.8374				
C.V. %=41.17		**Predicted R^2**=0.7995				
(a) ANOVA for Young's modulus						
Model	7,148E+07	9	$7{,}942\times10^6$	24.69	< 0.0001	**significant**
A-Time	6,159E+05	1	$6{,}159\times10^5$	1,92	0,1777	
B-Fiber rate	17869,64	1	17869.64	0.0556	0,8154	
C-Specimen Section	4,585E+05	1	$4.585\text{x}10^5$	1.43	0,2429	
AB	6,368E+05	1	6.368×10^5	1,98	0,1708	
AC	1,823E+05	1	1.823×10^5	0,5667	0,4581	
BC	6.090×10^5	1	6.090×10^5	1.89	0.1801	
A^2	1.562×10^5	1	1.562×10^7	48.57	< 0.0001	
B^2	1.235×10^5	1	1.235×10^5	0.38	0.5406	
C^2	2.587×10^5	1	2.587×10^5	0.80	0.3778	
Residual	8.684×10^6	27	3.216×10^5			
Lack of Fit	8.684×10^6	26	3.340×10^5	1382.6	0.0212	significant
Pure Error	241.56	1	241.56			
Total	8.016×10^7	36				

Std. Dev=567.12	**R^2**=0.8917
Mean=1460.27	**Adjusted R^2**=0.8556
C.V. %=38.84	**Predicted R^2**=0.8226

RSMresponse	**Mathematical model**
Stress	+0.140160×A+225.32968×B-0.283266×C-0.218776×AB-0.001616×AC-0.118491×BC+0.000571×A^2-481.48893×B^2+0.002258×C^2
Young's modulus	-8.49035×A-13647.97112×B+59.41965×C +49.82795×AB+0.116136×AC+ 221.99199×BC+0.055142×A^2-13805.76635×B^2-0.554836×C^2

A: processing time (0, 24 and 96), B: fiber content (15, 20, 25 and 30%), C: test section in mm²

Table V.9 provides a summary of the analysis of variance (ANOVA) for the stress and Young's modulus models. Significantly, both parameters exhibit P-values below 0.05, establishing their statistical significance. A model is deemed significant when the probability of the P-value is less than 0.05 [140]. In the context of the stress response, certain model terms, including C, A×B, B×C, and B^2, were found to be not significant. In contrast, terms A and B, A×C, A^2, and C^2 demonstrated significance owing to their smaller P-values and larger F-values. For Young's modulus, all model terms were statistically significant, with the exception of the interaction terms B, A×C, B^2, and C^2, which exhibited higher P-values and smaller F-values.

Analyzing the F values for the model term A^2 in stress and Young's modulus, reaching maximum values of 50.83% and 48.57% respectively, reveals that the variable "Time" is the most influential, impacting the output parameters by 69.13%. Following closely is "Fiber rate" at 47.95%, and then "Specimen section" at 37.25%. This aligns with a

related study by Adeyi[141], where sensitivity analysis highlighted soaking time (ST) as the most contributing factor to the variance of tensile strength, with an 86.2% value.

Furthermore, the determination coefficients R^2 and adjusted R^2 display high values of 87.81%, 89.17%, and 83.74%, 85.56% for maximum stress and Young's modulus, respectively. Generally, a good model fit falls within an R^2 value range of 0.8 to 0.9[142]. It is evident that this regression model demonstrates a robust correlation between experimental and predicted values, as shown in **Figure V.22**. The last figure underscores the agreement between expected and experimental values, surpassing a confidence level of 85%.

Figure V.23 illustrates Normal probability plots of residual values for **(a)** maximum stress and (b) Young's modulus. The straight alignment of residual values on these plots signifies a well-distributed error. In conclusion, these results affirm the statistical significance of the quadratic model for analyzing maximum stress and Young's modulus.

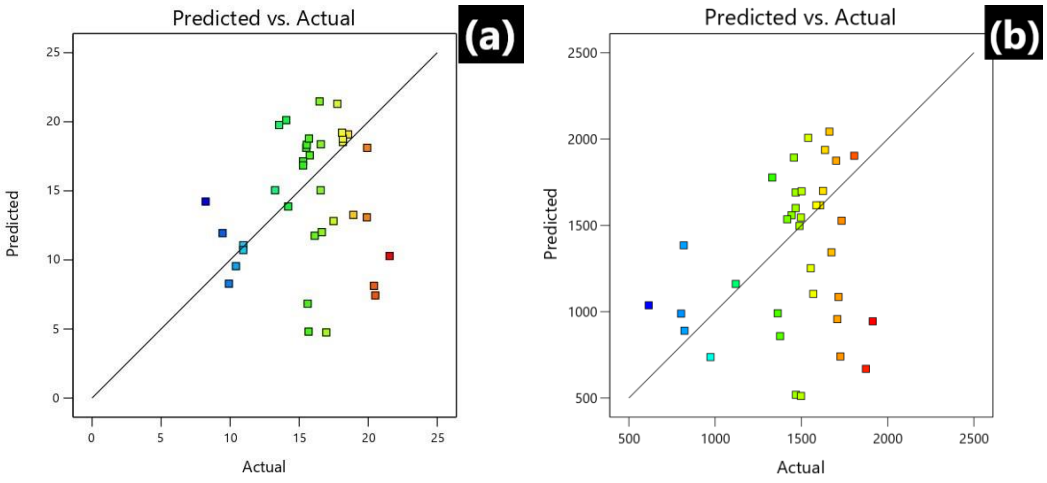

Figure V. 22*: Predicted vs. actual values for (a) maximum stress, and (c) Young's modulus*

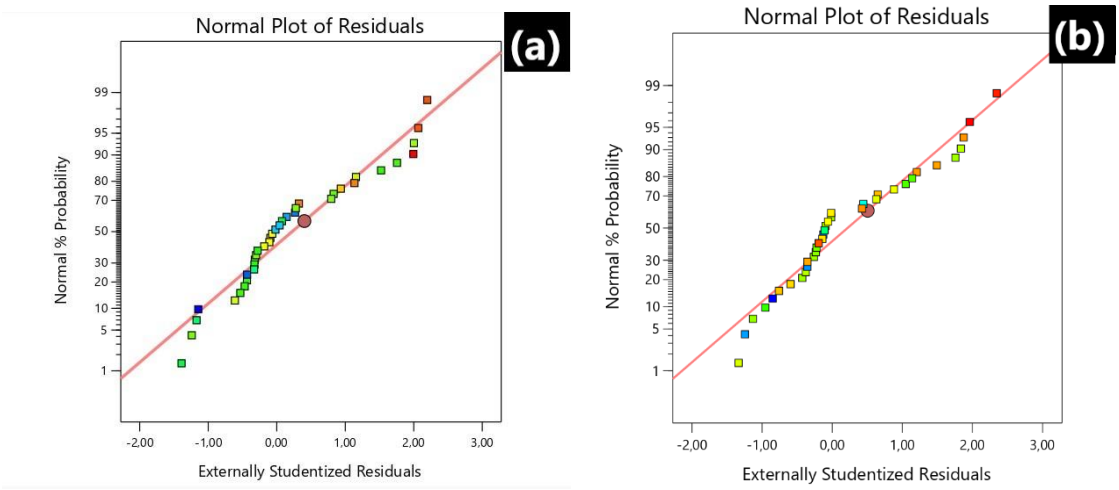

Figure V. 23:Normal probability plots of residual values for (a) maximum stress, and (b) Young's modulus

Figure V. 24 shows 3D surface plots of Stress as a function of the Specimen section with different Fiber rates at different times. **FigureV. 24.**a, 24b and **24c** present the evolution of Stress versus the Specimen section. The stress factor increases with the increase in the sample section rate, so that the stress at 0h, 30%, and 91.5057 mm^2 reached an estimated value of 17.221 MPa, while it reached a greater value estimated at 31.423 MPa at the same hour and fiber rate, with a specimen section estimated at 118.057 mm^2. While **Figure V. 24d, 24e, 24f,** and **24g** demonstrate the significant influence of the fiber rate on stress, mirroring the behavior observed with the sample section. Stress is noted to reach a value of 20.123 MPa at 0 hours, 118.075 mm^2, and a 15% fiber rate. However, a higher value, approximately 31.089 MPa, is observed under identical conditions, except the fiber rate is increased to 30%.

Contrastingly, the time factor exhibits a highly significant effect, diverging from the trends observed in the previous factors. In **Figure V.** 24**h, 24i** and **24j,** the stress is observed to be 20.118 MPa at 0 hours, 118.075 mm2, and a 15% fiber rate. Interestingly,

the stress reaches a minimum value of 7.252 MPa under the same specimen section and fiber rate, but this occurs after 24 hours, highlighting the contrasting impact of the time factor on stress compared to the other influencing factors. **Figure V. 25,** shows 3D surface plots of Young's modulus as a function of the Specimen section with different Fiber rates at different times. **Figure V.25*a*, 25b** and **25c** present the evolution of Young's modulus versus the Specimen section. The Young's modulus factor increases with the increase in the sample section rate so that Young's modulus at 0h, 30%, and 91.5057 mm2 reached an estimated value of 1700.31 MPa, while it reached a greater value estimated at 3000.73 MPa at the same hour and fiber rate, with a specimen section estimated at 118.057 mm2. While **Figure V. 25**d, **25e, 25f** and **25g** illustrate that, the fiber rate has a notable impact on Young's modulus. This behavior mirrors the influence of the sample section on Young's modulus. Specifically, Young's modulus attains a value of 1009.65 MPa at 0 hours and 118.075 mm^2, with a fiber rate of 15%. In contrast, a higher value, approximately 3100.63 MPa, is observed under similar conditions, except the fiber rate is increased to 30%. On the other hand, the time factor showed a very significant effect compared to the previous factors, and its effect on Young's modulus was the opposite of the behavior of the effect of the previous two factors, as **Figure V. 25h, 25i and 25j** showed that Young's modulus reached 1000 MPa at 0 h, 118.075 mm^2, and 15%. While it reached a minimum value estimated at 800.95 MPa at the same specimen section and the fiber rate, unlike the time it reached 96 hours

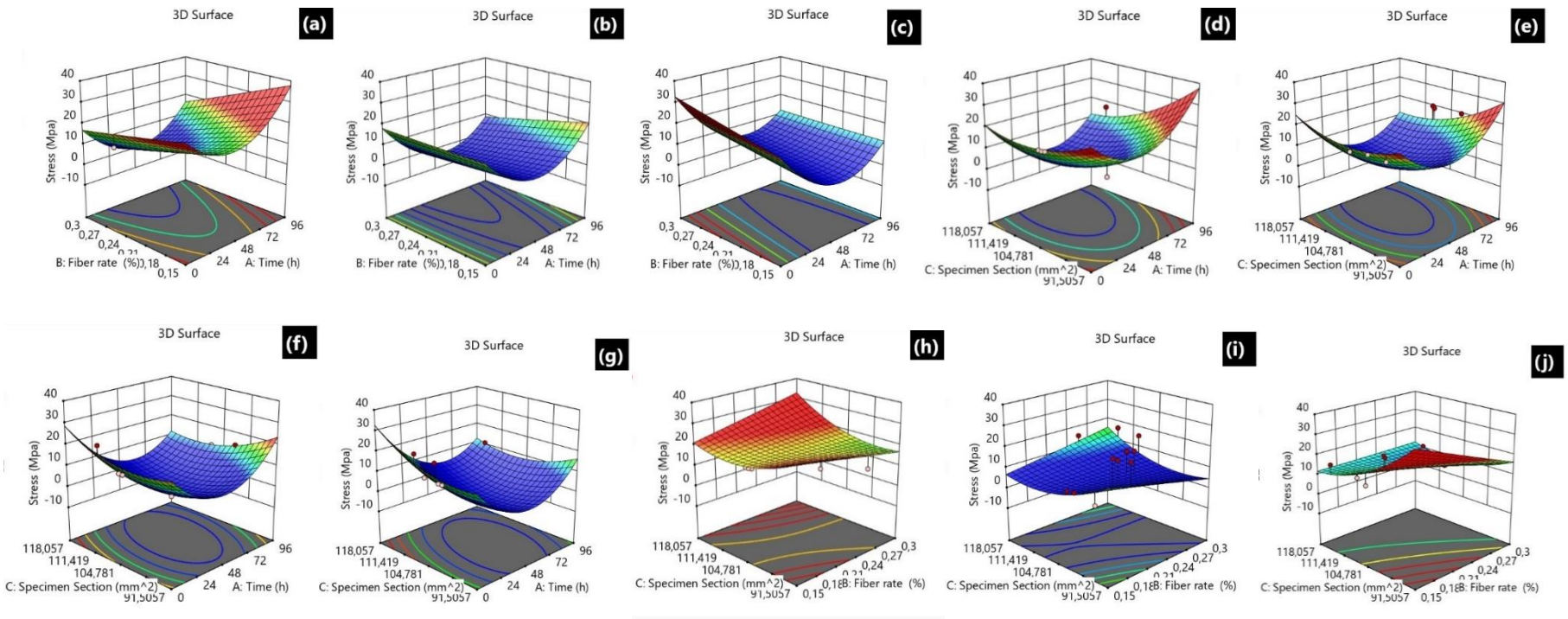

Figure V.24:3D surface plots of Stress as a function of Time , Fiber rate ,and Specimen section : a) 91.5057 mm^2, b) 103.151 mm^2 and c) 118.057 mm^2,and d) 15%, e) 20%, f) 25%,g) 30% ,and h) 0h , i) 24h ,j)96h.

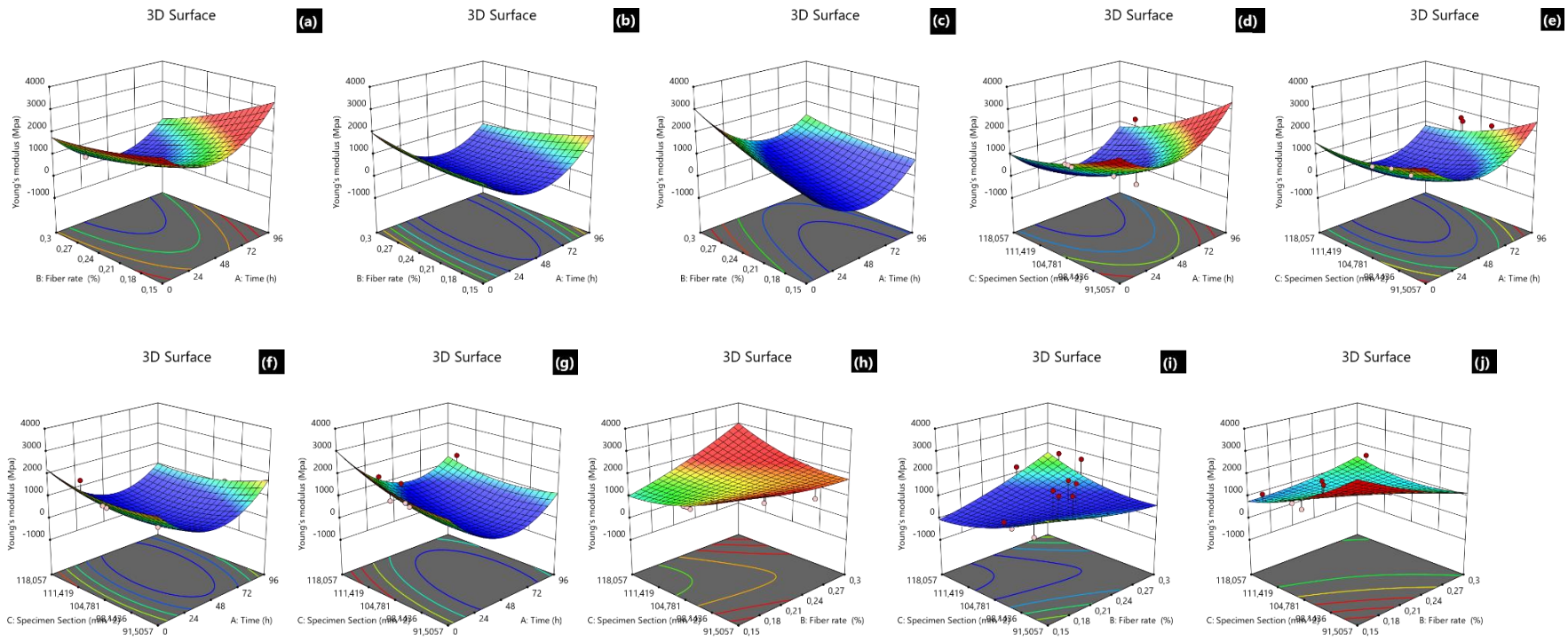

Figure V.25:3D surface plots of Young's modulus as a function of Time , Fiber rate ,and Specimen section : a) 91.5057 mm^2, b) 103.151 mm^2 and c) 118.057 mm^2,and d) 15%, e) 20%, f) 25%,g) 30% ,and h) 0h , i) 24h

Figure V.26 presents the values predicted by the RSM and ANN regression as graphs of determination coefficients with equality regression lines. The graphs of the coefficients of determination with the fitted regression lines clearly show a strong relationship between the trained models and the laboratory results. It is important to note that ANN exceeded the RSM, with an R^2 value of 0.95 for stress and an R^2 value of 0.96 for Young's modulus.

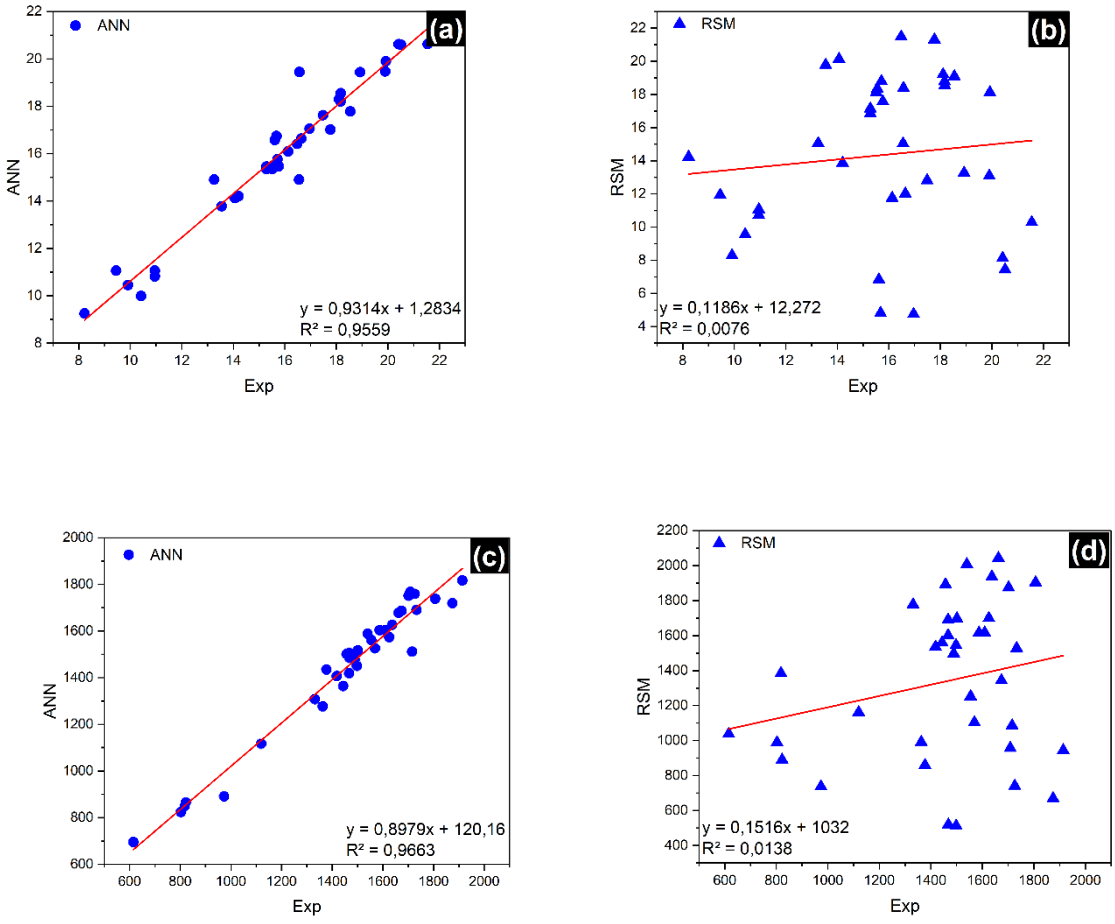

Figure V. 26: Experimental and predicted values of ANN mode predicted values of RSM mode: (a,b) Stress ,(c,d)Young's modulus

V.6.1.2.1.Comparison between experimental and predicted RSM and ANN model

This study implemented ANN and RSM-BBD methods to predict Young's stress and modulus. To assess the accuracy of the ANN and RSM-BBD models developed, the predicted data were compared to the average actual data, as shown in **Figure V. 27.** The values were plotted according to the execution numbers of the experiment.

The results obtained in the experiment confirmed the expected values in both methods for stress and Young's modulus, with close agreement between the predicted values and the experimental results. However, the ANN model provided better predictive values than the RSM-BBD model. The relationship between actual and expected results from the RSM-BBD and ANN models was examined using the coefficient of determination (R^2).

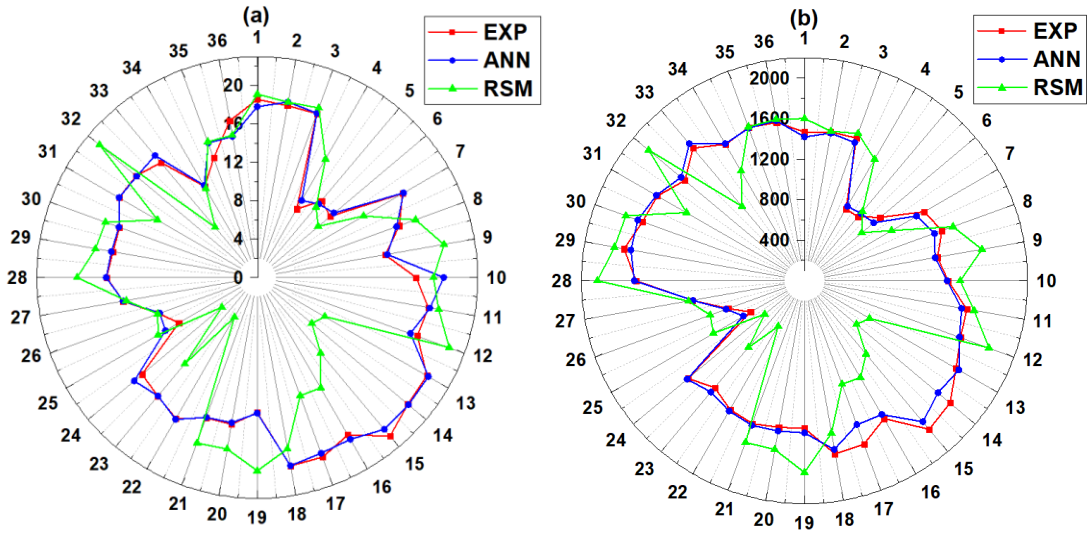

Figure V. 27: Comparison between experimental and predicted RSM and ANN models tensile data for: (a) Stress - (b) Young's modulus

VI.7.Conclusion

In summary, the chapter V of the thesis provides crucial insights into the mechanical behavior of tensile strength, compression, and water absorption of diverse fiber composites. Employing sophisticated methodologies such as artificial neural networks (ANN) and response surface methodology (RSM), this chapter delivers an extensive analysis, optimization, and modeling of the outcomes for these materials. The key discoveries of this chapter can be encapsulated as follows:

1. Regarding the mechanical behavior of epoxy samples:

- The experimental results showed, through tensile tests of the samples studied, that the diameter and shape of the hole affect the mechanical properties of the materials. The lowest stress and Young‘s Modulus were observed in the specimen with elliptical -notched.
- The results we obtained with the ANN and RSM models were excellent, however, the ANN model can be considered the best since it can predict the coefficient and the Young stress due to its high correction coefficient, which is close to 1. As a result, the results of the ANN model are closer to the experimental results.
- We have obtained excellent correlation coefficient results (R) for the Artificial Neural Network (ANN). Specifically, the correlation coefficients (R) for Young's Modulus were consistently greater than 0.984, with R = 0.99 for training, R = 1 for validation, R = 1 for the test set, and R = 0.984 overall. Regarding stress, the R values for all datasets exceeded 0.981, with R = 0.97, 1, and 1 for training, validation, and test sets, respectively.

- After comparing the experimental data to the expected data, the ANN modeling demonstrated an outstanding correlation, with an estimated average error value of 10^{-2} for stress and 10^{-0} for Young‘s Modulus.

- For the prediction of mechanical properties like stress and Young's Modulus values, an optimal network was employed with a training set size of 70%, validation set size of 15%, and test set size of 15%. The mean squared error (MSE) and the correlation coefficients were utilized as the evaluation metric in this study for determining the optimal network performance of ANN.

2. Regarding the mechanical behavior of honeycomb samples:

- Lamination ANOVA results revealed outstanding agreement between the predictive and empirical RSM models, as evidenced by adjusted R^2 and R^2 coefficients of 0.88 and 0.84 for force

3. Concerning the mechanical behavior of epoxy-reinforced palm samples:

- The correlation coefficients (R) for stress datasets are consistently high, exceeding 0.96 for training (1520.20647), validation (22716.61144), and testing (17600.81339). Similarly, for Young's modulus, all R values are above 0.92.
- The analysis of variance revealed that, among the three parameters investigated, time exerted the most significant influence on enhancing both constraint and Young's modulus.
- Utilizing Response Surface Methodology (RSM), optimal parameters for treatment, fiber rate, and sample section were identified, ensuring the achievement of satisfactory values for mechanical properties. This involved employing Analysis of Variance (ANOVA) to evaluate response means, supported by plots like the Mode Predicted Values Plot versus the RSM Mode Plot.
- ANOVA results for delamination indicated excellent agreement between predictive and experimental RSM models, with coefficients R^2 and adjusted R^2 of 0.87 and 0.83 for stress, and 0.89 and 0.85 for Young's modulus.

4. Regarding the absorption behavior:

- Utilizing the RSM model, the study examined how absorption time, fiber type, and fiber rate influence the absorption rate. The findings indicated a noteworthy agreement between

experimental and expected data, with adjusted correlation coefficients R^2 and R^2 reaching 94.98% and 94.86%, respectively

Conclusions and Perspectives

Conclusions and Perspectives

The thesis undertook a thorough investigation into the physical and chemical properties of composites reinforced with various types of fibers. Additionally, I recently delved into and advanced the understanding of the mechanical behavior and manufacturability of composites through molding. This involves incorporating fiber reinforcement with varying fiber ratios, diverse honeycomb geometries, and introducing holes within the tensile specimens.

- This thesis investigated the influence of **sample geometry on the mechanical properties of epoxy** tensile samples, examining intact, hole-notched, and elliptical-notched specimens. The results revealed that variations in hole diameter and shape significantly affected stress and Young's Modulus. Employing Artificial Neural Network (ANN) and Response Surface Methodology (RSM) models, the ANN model demonstrated superior predictive accuracy, achieving correlation coefficients exceeding where R^2= 0.984 for Young's Modulus and 0.981 for stress. The model showcased outstanding correlation and minimal average error values, emphasizing its effectiveness in predicting mechanical properties.
- Increasing hole diameter correlates with decreased strength, with the elliptical-notched specimen being the weakest. Standard deviations within the range of 6–37% indicate variations in mechanical behavior among test samples. The undamaged specimen exhibits the highest ultimate tensile strength (41.22 MPa) and Young's modulus (1793.80 MPa). Comparison with experimental values shows XFEM's efficiency, with error ratios below 3% for maximum stress and less than 17% for Young's modulus. High stress concentration around notches highlights their impact on reducing maximum tensile stress. In summary, XFEM proves effective in predicting epoxy polymer behavior, emphasizing the importance of careful meshing for reliable results and offering insights for practical applications and material design.
- The study on **honeycomb composites** concludes with a distinct preference for the fish star geometry, showcasing superior mechanical performance. The fish star cell, reinforced with

Luffa fibers, achieved a noteworthy maximum force of 4338.335851 N, outperforming the re-entrant geometry (1416.399925 N) and the hexagonal honeycomb (959.649407 N) for the same composite. Lamination ANOVA results further affirmed the reliability of the predictive RSM models, solidifying the fish star geometry's prominence in compression testing.

- A consistent decreasing trend in the bending strength of different types of fiber-reinforced compounds was observed as the percentage of fibers increased. This phenomenon is attributed to the weakened adhesion strength between the polymer's adhesive and the higher percentage of fibers employed. Notably, the bending strength reached its maximum in compounds reinforced with Sisal fibers. For Sisal-reinforced compounds, the maximum stresses were observed at 31.15 MPa, 26.43 MPa, and 23.14 MPa for fiber ratios of 10%, 15%, and 25%, respectively. This contrasted with the reinforced composites using Luffa and Diss fibers. The water absorption percentage results for the investigated compounds were in line with the mechanical characterization findings, revealing: Flexural properties decrease as **the water absorption** content increases in samples with high fiber content. Water absorption tests demonstrated an increasing absorption rate with an augmentation in fiber content within the compound. The lowest and highest absorption rates were observed at reinforcement levels, with approximate values of 2.77% for the Sisal-reinforced compound, 3.94% for the Diss fiber-enhanced compound, and 4.28% for the Luffa-reinforced compound at the 10% reinforcement level. At the 25% reinforcement level, the water absorption rates reached approximate values of 8.08%, 15.71%, and 20.77% for the Sisal, Diss, and Luffa fiber-reinforced compounds, respectively. Utilizing the RSM model, the study systematically examined how absorption time, fiber type, and fiber rate influence the absorption rate. The findings indicated a noteworthy agreement between experimental and expected data, with adjusted correlation coefficients R^2 and R^2 reaching 94.98% and 94.86%, respectively. This comprehensive analysis contributes

valuable insights into the mechanical behavior and water absorption characteristics of fiber-reinforced compounds.

- This study delves into the **mechanical properties of palm fiber-reinforced epoxy composite** laminates, emphasizing the impact of processing time, fiber content, and section. Key findings point towards significant enhancement (up to 20%) in mechanical properties with a 24-hour fiber strengthening process. Artificial Neural Networks (ANN) and Response Surface Methodology (RSM) models showcase strong correlations, though ANN reliability may vary. Low Mean Squared Error (MSE) values validate model effectiveness in capturing data patterns. High correlation coefficients (R) for stress and Young's modulus, along with influential time-dependent effects, underscore the study's robustness. Optimal parameters identified through RSM open avenues for further exploration.
- In-depth Study of Fiber-Matrix Interactions: Deepen the understanding of interactions between natural fibers and polymeric matrices. This includes exploring bonding mechanisms, adhesion phenomena, and structural changes induced by the chemical treatment of fibers.
- Continuous Optimization of Bio-composites: The promising results obtained in this thesis suggest the possibility of ongoing optimization of bio-composites by further exploring combinations of natural fibers, honeycomb geometries, and chemical pre-treatments. This could lead to even more high-performance materials suitable for a variety of applications.
- Optimization of Manufacturing Parameters: Further investigate manufacturing parameters, such as polymerization conditions, treatment temperatures, and fiber loading rates. The goal would be to optimize these parameters to enhance mechanical strength, durability, and other desirable properties.
- Studies on Environmental Sustainability: Evaluate the ecological footprint of developed bio-composites, with a focus on life cycle assessment, recyclability, and degradation. This could contribute to positioning these materials as more sustainable alternatives to synthetic materials.

- Industry-Specific Applications: Explore specific industrial applications of bio-composites reinforced with natural fibers. In-depth research in sectors such as the automotive industry, lightweight construction, aerospace, and other domains could reveal optimal use possibilities for these materials.
- Development of New Natural Fibers: Investigate the possibility of developing new natural fibers or genetically modifying existing fibers to enhance their mechanical properties and adaptability to bio-composites.
- Integration of Advanced Technologies: Incorporate advanced technologies, such as multi-material 3D printing, to create complex structures. The use of advanced numerical modeling techniques, multi-physics simulations, and artificial intelligence could also contribute to more precise design and optimization of material properties.
- Studies on Resistance to Environmental Conditions: Evaluate the resistance of bio-composites to extreme environmental conditions, such as exposure to UV radiation, humidity, extreme temperatures, etc. This would help anticipate the long-term behavior of these materials in real-world environments.
- Technology Transfer and Industrial Adoption: Facilitate technology transfer by collaborating with the industry to integrate these materials into existing manufacturing processes. This would also require efforts to raise awareness among industrial stakeholders about the economic and environmental benefits of bio-composites.
- Development of New Predictive Models: The comparison between ANN (Artificial Neural Network) and RSM (Response Surface Methodology) models has revealed the superiority of ANN in predicting mechanical behavior. The development of new predictive models based on machine learning techniques could be a perspective to enhance prediction accuracy.

- By investing in these research areas, it would be possible to significantly advance the science of bio-composites reinforced with natural fibers, paving the way for technological innovations and sustainable solutions in various industrial sectors.

References

1. **Hsissou, R., R. Seghiri, Z. Benzekri, M. Hilali, M. Rafik, and A. Elharfi, *Polymer composite materials: A comprehensive review.* Composite Structures, 2021. 262: p. 113640. https://doi.org/10.1016/j.compstruct.2021.113640.**

2. **Lu, Y., J. Chen, D. Feng, L. Wang, and M. Liu, *Numerical modeling of hypervelocity impacts on carbon fiber reinforced plastics using a GPU-accelerated SPH model.* Computational Mechanics, 2023. 10.1007/s00466-023-02318-7.**

3. **Yuhazri, M.Y., A.J. Zulfikar, and A. Ginting, *Fiber Reinforced Polymer Composite as a Strengthening of Concrete Structures: A Review.* IOP Conference Series: Materials Science and Engineering, 2020. 1003(1): p. 012135. 10.1088/1757-899x/1003/1/012135.**

4. **Abramovich, H., *1 - Introduction to composite materials*, in *Stability and Vibrations of Thin Walled Composite Structures*, H. Abramovich, Editor 2017, Woodhead Publishing. p. 1-47.**
5. **Kim, Y.K. and V. Chalivendra, *14 - Natural fibre composites (NFCs) for construction and automotive industries*, in *Handbook of Natural Fibres (Second Edition)*, R.M. Kozłowski and M. Mackiewicz-Talarczyk, Editors. 2020, Woodhead Publishing. p. 469-498.**
6. **Taj, S., M.A. Munawar, and S. Khan, *Natural fiber-reinforced polymer composites.* Proceedings-Pakistan Academy of Sciences, 2007. 44(2): p. 129.**

7. **Keya, K.N., N.A. Kona, F.A. Koly, K.M. Maraz, M.N. Islam, and R.A. Khan, *Natural fiber reinforced polymer composites: history, types, advantages and applications.* Materials Engineering Research, 2019. 1(2): p. 69-85.**

8. **Faruk, O., A.K. Bledzki, H.-P. Fink, and M. Sain, *Biocomposites reinforced with natural fibers: 2000–2010.* Progress in polymer science, 2012. 37(11): p. 1552-1596.**

9. **Nguong, C., S. Lee, and D. Sujan, *A review on natural fibre reinforced polymer composites.* International Journal of Materials and Metallurgical Engineering, 2013. 7(1): p. 52-59.**

10. **Rajak, D.K., D.D. Pagar, R. Kumar, and C.I. Pruncu, *Recent progress of reinforcement materials: a comprehensive overview of composite materials.* Journal of Materials Research and Technology, 2019. 8(6): p. 6354-6374. https://doi.org/10.1016/j.jmrt.2019.09.068.**

11. **Pickering, K., *Properties and performance of natural-fibre composites*2008: Elsevier.**
12. **Bekele, A.E., H.G. Lemu, and M.G. Jiru, *Experimental study of physical, chemical and mechanical properties of enset and sisal fibers.* Polymer Testing, 2022. 106: p. 107453. https://doi.org/10.1016/j.polymertesting.2021.107453.**

13. **Amroune, S., A. Bezazi, A. Belaadi, C. Zhu, F. Scarpa, S. Rahatekar, and A. Imad, *Tensile mechanical properties and surface chemical sensitivity of technical fibres from date palm fruit branches***

(Phoenix dactylifera L.). **Composites Part A: Applied Science and Manufacturing, 2015. 71: p. 95-106. https://doi.org/10.1016/j.compositesa.2014.12.011.**

14. **Balaji, V., *Mechanical characterization of coir fiber and cotton fiber reinforced unsaturated polyester composites for packaging applications.* Journal of Applied Packaging Research, 2017. 9(2): p. 2.**

15. **Jha, K., P. Tamrakar, R. Kumar, S. Sharma, J. Singh, R.A. Ilyas, S.M. Rangappa, and S. Siengchin, *Effect of hybridization on physio-mechanical behavior of Vetiver and Jute fibers reinforced epoxy composites for structural applications: Studies on fabrication, physicomechanical, water-absorption, and morphological properties.* Journal of Industrial Textiles, 2022. 51(2_suppl): p. 2642S-2664S.**

16. **Sellami, A., M. Merzoud, and S. Amziane, *Improvement of mechanical properties of green concrete by treatment of the vegetals fibers.* Construction and Building Materials, 2013. 47: p. 1117-1124. https://doi.org/10.1016/j.conbuildmat.2013.05.073.**

17. **Qaiss, A., R. Bouhfid, and H. Essabir, *Effect of processing conditions on the mechanical and morphological properties of composites reinforced by natural fibres.* Manufacturing of natural fibre reinforced polymer composites, 2015: p. 177-197.**

18. **Sathishkumar, G.K., M. Ibrahim, M. Mohamed Akheel, G. Rajkumar, B. Gopinath, R. Karpagam, P. Karthik, M. Martin Charles, G. Gautham, and G. Gowri Shankar, *Synthesis and Mechanical Properties of Natural Fiber Reinforced Epoxy/Polyester/Polypropylene Composites: A Review.* Journal of Natural Fibers, 2022. 19(10): p. 3718-3741. 10.1080/15440478.2020.1848723.**

19. **AMROUNE, S., *Caractérisations mécaniques et étude de l'endommagement des matériaux composites renforcés par des fibres de palmier*, 2016.**
20. **Koçak, D., S. Mistik, M. Akalin, and N. Merdan, *The use of Luffa cylindrica fibres as reinforcements in composites*, in *Biofiber reinforcements in composite materials*2015, Elsevier. p. 689-699.**
21. **Tanobe, V.O., T.H. Sydenstricker, M. Munaro, and S.C. Amico, *A comprehensive characterization of chemically treated Brazilian sponge-gourds (Luffa cylindrica).* Polymer Testing, 2005. 24(4): p. 474-482.**

22. **Bisen, H.B., C.K. Hirwani, R.K. Satankar, S.K. Panda, K. Mehar, and B. Patel, *Numerical study of frequency and deflection responses of natural fiber (Luffa) reinforced polymer composite and experimental validation.* Journal of Natural Fibers, 2018.**

23. **Asyraf, M., M. Yahya, and S. Hassan, *Hybrid Synthetic and Natural Fibres in Honeycomb Sandwich Composites for Structural Applications: A Brief Review.* Journal of Natural Fibre Polymer Composites (JNFPC).**

24. **Luzi, F., D. Puglia, F. Sarasini, J. Tirillò, G. Maffei, A. Zuorro, R. Lavecchia, J. Kenny, and L. Torre, *Valorization and extraction of cellulose nanocrystals from North African grass: Ampelodesmos mauritanicus (Diss).* Carbohydrate polymers, 2019. 209: p. 328-337.**

25. **Zhang, M.Q., M.Z. Rong, and X. Lu, *Fully biodegradable natural fiber composites from renewable resources: all-plant fiber composites.* Composites Science and Technology, 2005. 65(15-16): p. 2514-2525.**

26. **Alvarez, V.A., J.M. Kenny, and A. Vázquez, *Creep behavior of biocomposites based on sisal fiber reinforced cellulose derivatives/starch blends.* Polymer Composites, 2004. 25(3): p. 280-288.**

27. **de Andrade Silva, F., B. Mobasher, and R.D. Toledo Filho, *Cracking mechanisms in durable sisal fiber reinforced cement composites.* Cement and Concrete Composites, 2009. 31(10): p. 721-730.**

28. **Badanayak, P., S. Jose, and G. Bose, *Banana pseudostem fiber: A critical review on fiber extraction, characterization, and surface modification.* Journal of Natural Fibers, 2023. 20(1): p. 2168821.**

29. **Zhao, J., X. Wu, X. Yuan, X. Yang, H. Guo, W. Yao, D. Ji, X. Li, and L. Zhang, *Nanocellulose and Cellulose Making with Bio-Enzymes from Different Particle Sizes of Neosinocalamus Affinis.* Coatings, 2022. 12(11): p. 1734.**

30. **Daramola, O., A. Akinwekomi, A. Adediran, O. Akindote-White, and E. Sadiku, *Mechanical performance and water uptake behaviour of treated bamboo fibre-reinforced high-density polyethylene composites.* Heliyon, 2019. 5(7).**

31. **Bezazi, A., A. Belaadi, M. Bourchak, F. Scarpa, and K. Boba, *Novel extraction techniques, chemical and mechanical characterisation of Agave americana L. natural fibres.* Composites Part B: Engineering, 2014. 66: p. 194-203.**

32. **Gañán, P., J. Cruz, S. Garbizu, A. Arbelaiz, and I. Mondragon, *Stem and bunch banana fibers from cultivation wastes: Effect of treatments on physico-chemical behavior.* Journal of Applied Polymer Science, 2004. 94(4): p. 1489-1495.**

33. **Boddula, R., M.I. Ahamed, and A.M. Asiri, *Green adhesives: preparation, properties, and applications*2020: John Wiley & Sons.**

34. **Heng, J.Y., D.F. Pearse, F. Thielmann, T. Lampke, and A. Bismarck, *Methods to determine surface energies of natural fibres: a review.* Composite Interfaces, 2007. 14(7-9): p. 581-604.**

35. **Mohankumar, D., V. Amarnath, V. Bhuvaneswari, S. Saran, K. Saravanaraj, M.S. Gogul, S. Sridhar, G. Kathiresan, and L. Rajeshkumar. *Extraction of plant based natural fibers–A mini review*. in *IOP Conference Series: Materials Science and Engineering*. 2021. IOP Publishing.**

36. **Adekunle, K.F., *Surface treatments of natural fibres—A review: Part 1.* Open Journal of Polymer Chemistry, 2015. 5(03): p. 41-46.**

37. **George, S., S. Thomas, N. Nandanan Nedumpillil, and S. Jose, *Extraction and Characterization of Fibers from Water Hyacinth Stem Using a Custom-Made Decorticator.* Journal of Natural Fibers, 2023. 20(2): p. 2212927.**

38. **Saravanakumar, A. and S. Sivalingam, *Dry sliding wear of AA2219/Gr metal matrix composites.* Materials Today: Proceedings, 2018. 5(2): p. 8321-8327.**

39. **Chakar, F.S. and A.J. Ragauskas, *Review of current and future softwood kraft lignin process chemistry.* Industrial Crops and Products, 2004. 20(2): p. 131-141.**

40. **Shaker, K., R.M.W.U. Khan, M. Jabbar, M. Umair, A. Tariq, M. Kashif, and Y. Nawab, *Extraction and characterization of novel fibers from Vernonia elaeagnifolia as a potential textile fiber.* Industrial Crops and Products, 2020. 152: p. 112518.**

41. **Kargarzadeh, H., J. Huang, N. Lin, I. Ahmad, M. Mariano, A. Dufresne, S. Thomas, and A. Gałęski, *Recent developments in nanocellulose-based biodegradable polymers, thermoplastic polymers, and porous nanocomposites.* Progress in polymer science, 2018. 87: p. 197-227.**

42. **Amroune, S., A. Belaadi, R. Dalmis, Y. Seki, A. Makhlouf, and H. Satha, *Quantitatively Investigating the Effects of Fiber Parameters on Tensile and Flexural Response of Flax/Epoxy Biocomposites.* Journal of Natural Fibers, 2022. 19(6): p. 2366-2381. https://doi.org/10.1080/15440478.2020.1817831.**

43. **Hestiawan, H., Jamasri, and Kusmono, *Effect of chemical treatments on tensile properties and interfacial shear strength of unsaturated polyester/fan palm fibers.* Journal of Natural Fibers, 2018. 15(5): p. 762-775.**

44. **Ramesh, D., B.G. Ayre, C.L. Webber, and N.A. D'Souza, *Dynamic mechanical analysis, surface chemistry and morphology of alkali and enzymatic retted kenaf fibers.* Textile Research Journal, 2015. 85(19): p. 2059-2070.**

45. **Jayamani, E., S. Hamdan, M.R. Rahman, K.H. Soon, and M.K.B. Bakri, *Processing and characterization of epoxy/luffa composites: Investigation on chemical treatment of fibers on mechanical and acoustical properties.* BioResources, 2014. 9(3): p. 5542-5556.**

46. **Ashok, K., K. Kalaichelvan, and A. Damodaran, *Effect of nano fillers on mechanical properties of luffa fiber epoxy composites.* Journal of Natural Fibers, 2022. 19(4): p. 1472-1489.**

47. **Raharjo, P.W., R. Soenoko, A. Purnowidodo, and A. Choiron, *Characterization of sodium-bicarbonate-treated Zalacca fibers as composite reinforcements.* 2019.**

48. **Younis, A.A., S.A.A. Mohamed, and M. El-Sakhawy, *Fire resistant and mechanical properties of bagasse packaging paper coated with hexachlorocyclodiphosph(V)azane/starch/NaHCO3/CaCO3/cellulose nanocrystals composite.* Egyptian Journal of Petroleum, 2022. 31(3): p. 55-64. https://doi.org/10.1016/j.ejpe.2022.07.001.**

49. **Yogesh, P., S.P. Singarayar, M. Rajkamal, T. Venkatesh, R. kumar Gupta, and G. Yatika, *Mechanical performance of aloe vera/dharbai-based hybrid epoxy composites with enhanced NaHCO3 treatment.* Materials Today: Proceedings, 2022. 69: p. 1394-1401.**

50. **Fiore, V., T. Scalici, and A. Valenza, *Effect of sodium bicarbonate treatment on mechanical properties of flax-reinforced epoxy composite materials.* Journal of Composite Materials, 2018. 52(8): p. 1061-1072.**

51. **Fiore, V., T. Scalici, F. Nicoletti, G. Vitale, M. Prestipino, and A. Valenza, *A new eco-friendly chemical treatment of natural fibres: Effect of sodium bicarbonate on properties of sisal fibre and its epoxy composites.* Composites Part B: Engineering, 2016. 85: p. 150-160. https://doi.org/10.1016/j.compositesb.2015.09.028.**

52. **Das, P.P., A. Manral, F. Ahmad, B. Sharma, V. Chaudhary, S. Gupta, and P. Gupta, *Environmentally sustainable chemical treatment of plant fibers for improved performance of polymeric composites.* Polymer Composites, 2022. 43(10): p. 7155-7169.**

53. **Shalwan, A. and B.F. Yousif, *In State of Art: Mechanical and tribological behaviour of polymeric composites based on natural fibres.* Materials & Design, 2013. 48: p. 14-24. https://doi.org/10.1016/j.matdes.2012.07.014.**

54. **Ramesh, M., K. Palanikumar, and K.H. Reddy, *Mechanical property evaluation of sisal–jute–glass fiber reinforced polyester composites.* Composites Part B: Engineering, 2013. 48: p. 1-9. https://doi.org/10.1016/j.compositesb.2012.12.004.**

55. **Gulías, J., R. Melis, D. Scordia, J. Cifre, G. Testa, S.L. Cosentino, and C. Porqueddu, *Exploring the potential of wild perennial grasses as a biomass source in semi-arid Mediterranean environments.* Italian Journal of Agronomy, 2018. 13(2): p. 103-111.**

56. **Roy, S., S. Shit, R. Sengupta, and P. Shukla, *A review on bio-composites: fabrication, properties and applications.* Int. J. Innov. Res. Sci. Eng. Technol, 2014. 3(10): p. 16814-16824.**

57. **Lotfi, A., H. Li, D.V. Dao, and G. Prusty, *Natural fiber–reinforced composites: A review on material, manufacturing, and machinability.* Journal of Thermoplastic Composite Materials, 2021. 34(2): p. 238-284.**

58. **Khalid, M.Y., A. Al Rashid, Z.U. Arif, W. Ahmed, H. Arshad, and A.A. Zaidi, *Natural fiber reinforced composites: Sustainable materials for emerging applications.* Results in Engineering, 2021. 11: p. 100263.**

59. **Maaruf, S.Z., E.M. Zain, and N. Abdullah, *Sustaining local heritage: fibre art as a new paradigm to uplift Malaysian craft production.* Malaysian Journal of Sustainable Environment, 2020. 7(2): p. 119-132.**

60. **Bourban, P.-E., *Matériaux composites à matrice organique: constituants, procédés, propriétés*. Vol. 15. 2004: PPUR presses polytechniques.**

61. **Wallenberger, F.T. and N. Weston, *Natural fibers, plastics and composites*2003: Springer Science & Business Media.**

62. **Igwegbe, C.A., O.D. Onukwuli, J.O. Ighalo, and M.C. Menkiti, *Bio-coagulation-flocculation (BCF) of municipal solid waste leachate using Picralima nitida extract: RSM and ANN modelling.* Current Research in Green and Sustainable Chemistry, 2021. 4: p. 100078. https://doi.org/10.1016/j.crgsc.2021.100078.**

63. **Onu, C.E., P.K. Igbokwe, J.T. Nwabanne, C.O. Nwajinka, and P.E. Ohale, *Evaluation of optimization techniques in predicting optimum moisture content reduction in drying potato slices.* Artificial intelligence in Agriculture, 2020. 4: p. 39-47.**

64. **Geyikçi, F., E. Kılıç, S. Çoruh, and S. Elevli, *Modelling of lead adsorption from industrial sludge leachate on red mud by using RSM and ANN.* Chemical Engineering Journal, 2012. 183: p. 53-59. https://doi.org/10.1016/j.cej.2011.12.019.**

65. **Alara, O.R., N.H. Abdurahman, H.K. Afolabi, and O.A. Olalere, *Efficient extraction of antioxidants from Vernonia cinerea leaves: Comparing response surface methodology and artificial neural network.* Beni-Suef University Journal of Basic and Applied Sciences, 2018. 7(3): p. 276-285.**

66. **Okewale, A., F. Omoruwuo, and O. Adesina. *Comparative studies of response surface methodology (RSM) and predictive capacity of artificial neural network (ANN) on mild steel corrosion inhibition using water hyacinth as an inhibitor*. in *Journal of Physics: Conference Series*. 2019. IOP Publishing.**

67. **Feng, Y., M. Mohammadi, L. Wang, M. Rashidi, and P. Mehrabi, *Application of artificial intelligence to evaluate the fresh properties of self-consolidating concrete.* Materials, 2021. 14(17): p. 4885.**

68. **Congro, M., V.M. de Alencar Monteiro, A.L. Brandão, B.F. dos Santos, D. Roehl, and F. de Andrade Silva, *Prediction of the residual flexural strength of fiber reinforced concrete using artificial neural networks.* Construction and Building Materials, 2021. 303: p. 124502.**

69. **Farooq, A., M.I. Sarwar, M.A. Ashraf, D. Iqbal, A. Hussain, and S. Malik, *Predicting cotton fibre maturity by using artificial neural network.* Autex Research Journal, 2018. 18(4): p. 429-433.**

70. **Tapkın, S., A. Çevik, and Ü. Uşar, *Accumulated strain prediction of polypropylene modified marshall specimens in repeated creep test using artificial neural networks.* Expert Systems with Applications, 2009. 36(8): p. 11186-11197.**

71. **Nwosu-Obieogu, K., G.W. Dzarma, G. Christian, U.C. Nonso, A.M. Awele, and O.O. Anozie, *Physico-chemical/mechanical properties of treated groundnut shell fibre; Response surface methodology and artificial neural network performance evaluation and optimisation.* Cleaner Waste Systems, 2022. 2: p. 100017.**

72. **Barbero, E.J., *Finite Element Analysis of Composite Materials using Abaqus®*2023: CRC press.**

73. **Cruz, S.F., D. Pasquini, D.A. Cerqueira, V.d.S. Prado, and R.M.N. Assunção, *Water flux through cellulose triacetate films produced from heterogeneous acetylation of sugar cane bagasse.* J Membrane Sci, 2000. 177. 10.1016/s0376-7388(00)00469-5.**

74. **Abdellah, M.Y., A.S. Abo-El Hagag, W. Marzok, A. Hashem, and A.H. Backer, *Tensile and Farcture Properties of Hybrid Date Palm Fibre Composite Structures Embedded with Chopped Rubber.***

75. Tillmann, V.B., *Análise Estrutural de Elementos Compósitos Com a Utilização do Método de Elementos Finitos.* 2015.

76. Daniel, I.M., O. Ishai, I.M. Daniel, and I. Daniel, *Engineering mechanics of composite materials*. Vol. 1994. 2006: Oxford university press New York.
77. Bednarcyk, B.A., J. Aboudi, and S.M. Arnold, *Micromechanics of composite materials governed by vector constitutive laws.* International Journal of Solids and Structures, 2017. 110-111: p. 137-151. https://doi.org/10.1016/j.ijsolstr.2017.01.033.

78. Bauchau, O.A. and J.I. Craig, *Structural analysis: with applications to aerospace structures*. Vol. 163. 2009: Springer Science & Business Media.
79. Soriano, H.L., *Método de Elementos Finitos em Análise de Estruturas Vol. 48*2003: EdUSP.
80. David Müzel, S., E.P. Bonhin, N.M. Guimarães, and E.S. Guidi, *Application of the finite element method in the analysis of composite materials: A review.* Polymers, 2020. 12(4): p. 818.

81. Caycedo Garcia, M.S., G.H. Siqueira, L.C.M. Vieira Junior, and I. Vizotto, *Evaluation of structural capacity of triangular and hexagonal reinforced concrete free-form shells.* Engineering Structures, 2019. 188: p. 519-537. https://doi.org/10.1016/j.engstruct.2019.03.044.

82. Azevedo, C.A.C.d., *Formulação alternativa para análise de domínios não-homogêneos e inclusões anisotrópicas via MEC*, 2007, Universidade de São Paulo.
83. Kumar, K.S., R. Biju, and C.R. Nair, *Progress in shape memory epoxy resins.* Reactive and Functional Polymers, 2013. 73(2): p. 421-430.

84. Jeon, H., J. Park, and M. Shon, *Corrosion protection by epoxy coating containing multi-walled carbon nanotubes.* Journal of Industrial and Engineering Chemistry, 2013. 19(3): p. 849-853.

85. Lee, S.B., H.J. Lee, and I.K. Hong, *Diluent filler particle size effect for thermal stability of epoxy type resin.* Journal of Industrial and Engineering Chemistry, 2012. 18(2): p. 635-641.

86. Jin, F.-L., S.-Y. Lee, and S.-J. Park, *Polymer matrices for carbon fiber-reinforced polymer composites.* Carbon letters, 2013. 14(2): p. 76-88.

87. Pham, V.H., Y.W. Ha, S.H. Kim, H.T. Jeong, M.Y. Jung, B.S. Ko, Y.J. Hwang, and J.S. Chung, *Synthesis of epoxy encapsulated organoclay nanocomposite latex via phase inversion emulsification and its gas barrier property.* Journal of Industrial and Engineering Chemistry, 2014. 20(1): p. 108-112.

88. Li, Y., P. Badrinarayanan, and M.R. Kessler, *Liquid crystalline epoxy resin based on biphenyl mesogen: Thermal characterization.* Polymer, 2013. 54(12): p. 3017-3025.

89. Jin, F.-L. and S.-J. Park, *Recent advances in carbon-nanotube-based epoxy composites.* Carbon letters, 2013. 14(1): p. 1-13.

90. **Baley, C., F. Busnel, Y. Grohens, and O. Sire, *Influence of chemical treatments on surface properties and adhesion of flax fibre–polyester resin.* Composites Part A: Applied Science and Manufacturing, 2006. 37(10): p. 1626-1637.**

91. **Bledzki, A. and J. Gassan, *Composites reinforced with cellulose based fibres.* Progress in polymer science, 1999. 24(2): p. 221-274.**

92. **Santos, J.C.d., L.Á.d. Oliveira, L.M. Gomes Vieira, V. Mano, R.T.S. Freire, and T.H. Panzera, *Eco-friendly sodium bicarbonate treatment and its effect on epoxy and polyester coir fibre composites.* Construction and Building Materials, 2019. 211: p. 427-436. https://doi.org/10.1016/j.conbuildmat.2019.03.284.**

93. **Santos, J.C.d., P.R. Oliveira, R.T.S. Freire, L.M.G. Vieira, J.C.C. Rubio, and T.H. Panzera, *The Effects of Sodium Carbonate and Bicarbonate Treatments on Sisal Fibre Composites.* Materials Research, 2022. 25.**

94. **Yao, T., Z. Deng, K. Zhang, and S. Li, *A method to predict the ultimate tensile strength of 3D printing polylactic acid (PLA) materials with different printing orientations.* Composites Part B: Engineering, 2019. 163: p. 393-402.**

95. **Primo, T., M. Calabrese, A. Del Prete, and A. Anglani, *Additive manufacturing integration with topology optimization methodology for innovative product design.* The International Journal of Advanced Manufacturing Technology, 2017. 93: p. 467-479.**

96. **Pakkanen, J., D. Manfredi, P. Minetola, and L. Iuliano, *About the use of recycled or biodegradable filaments for sustainability of 3D printing: State of the art and research opportunities.* Sustainable Design and Manufacturing 2017: Selected papers on Sustainable Design and Manufacturing 4, 2017: p. 776-785.**

97. **Turner, B.N. and S.A. Gold, *A review of melt extrusion additive manufacturing processes: II. Materials, dimensional accuracy, and surface roughness.* Rapid Prototyping Journal, 2015. 21(3): p. 250-261.**

98. **Menderes, K., H. Saruhan, and A. Ipekci, *Investigation the effects of 3D printer system vibrations on mechanical properties of the printed products.* Sigma Journal of Engineering and Natural Sciences, 2018. 36(3): p. 655-666.**

99. **Aumnate, C., A. Pongwisuthiruchte, P. Pattananuwat, and P. Potiyaraj, *Fabrication of ABS/graphene oxide composite filament for fused filament fabrication (FFF) 3D printing.* Advances in Materials Science and engineering, 2018. 2018: p. 1-9.**

100. **Gohar, S., G. Hussain, A. Ali, and H. Ahmad, *Mechanical performance of honeycomb sandwich structures built by FDM printing technique.* Journal of Thermoplastic Composite Materials, 2023. 36(1): p. 182-200.**

101. **Özdilli, Ö., *Comparison of the Surface Quality of the Products Manufactured by the Plastic Injection Molding and SLA and FDM Method.* International Journal of Engineering Research and Development, 2021. 13(2): p. 428-437.**

102. **Kun, K., *Reconstruction and development of a 3D printer using FDM technology.* Procedia Engineering, 2016. 149: p. 203-211.**

103. **Petersen, E.E., R.W. Kidd, and J.M. Pearce, *Impact of DIY home manufacturing with 3D printing on the toy and game market.* Technologies, 2017. 5(3): p. 45.**

104. **Kam, M., A. Ipekci, and O. Sengul, *Taguchi optimization of fused deposition modeling process parameters on mechanical characteristics of PLA+ filament material.* Scientia Iranica, 2022. 29(1): p. 79-89.**

105. **Atakok, G., M. Kam, and H.B. Koc, *Tensile, three-point bending and impact strength of 3D printed parts using PLA and recycled PLA filaments: A statistical investigation.* Journal of Materials Research and Technology, 2022. 18: p. 1542-1554.**

106. **Saada, K., M. Zaoui, S. Amroune, R. Benyettou, A. Hechaichi, M. Jawaid, M. Hashem, and I. Uddin, *Exploring tensile properties of bio composites reinforced date palm fibers using experimental and Modelling Approaches.* Materials Chemistry and Physics, 2023: p. 128810. https://doi.org/10.1016/j.matchemphys.2023.128810.**

107. **Goutham, E.R.S., Y. Vamshi, M. Namratha, K.B. Gupta, M. Chandrasekar, and J. Naveen. *Influence of glass fibre hybridization on the open hole tensile properties of pineapple leaf fiber/epoxy composites*. in *AIP Conference Proceedings*. 2022. AIP Publishing LLC.**

108. **Zhu, l., F. Xu, and w. Shen, *Numerical analyses of axial tension mechanisms of 3D orthogonal woven E-glass/epoxy composites with drilled holes.* Textile Research Journal, 2022. 92(19-20): p. 3478-3487.**

109. **Saada, K., S. Amroune, M. Zaoui, A. Houari, K. Madani, and A. Hachaichi, *Experimental and Numerical Study of the Effect of the Presence of a Geometric Discontinuity of Variable Shape on the Tensile Strength of an Epoxy Polymer.* Acta Mechanica et Automatica, 2023. 17(2): p. 192-199.**

110. **Najafi, M., R. Ansari, and A. Darvizeh, *Environmental effects on mechanical properties of glass/epoxy and fiber metal laminates, Part I: hygrothermal aging.* Mechanics of advanced composite structures, 2017. 4(3): p. 187-196.**

111. **Bhaskar, K., V. Santhanam, and A. Devaraju, *Dielectric strength analysis of acacia nilotica with chemically treated sisal fiber reinforced polyester composite.* Dig J Nanomater Biostructures, 2020. 15(1): p. 107-113.**

112. **Zhang, Y. and C. Mi, *Improved hydrothermal aging performance of glass fiber-reinforced polymer composites via silica nanoparticle coating.* Journal of Applied Polymer Science, 2020. 137(19): p. 48652.**

113. **Handoko, W., F. Pahlevani, and V. Sahajwalla, *Enhancing corrosion resistance and hardness properties of carbon steel through modification of microstructure.* Materials, 2018. 11(12): p. 2404.**

114. **Tse, W.F.W., *Effects of C and B microalloying additions on the microstructure and processability of Ren\'e 41 Ni-based superalloy.* arXiv preprint arXiv:2304.12763, 2023.**

115. **Kavvads, M. and G. Gazetas, *Kinematic seismic response and bending of free-head piles in layered soil.* Geotechnique, 1993. 43(2): p. 207-222.**

116. **Geramizadeh, H., S. Dariushi, and S.J. Salami, *Optimal face sheet thickness of 3D printed polymeric hexagonal and re-entrant honeycomb sandwich beams subjected to three-point bending.* Composite Structures, 2022. 291: p. 115618.**

117. **Hosseinabadi, H.G., R. Bagheri, L.A. Gray, V. Altstädt, and K. Drechsler, *Plasticity in polymeric honeycombs made by photo-polymerization and nozzle based 3D-printing.* Polymer Testing, 2017. 63: p. 163-167.**

118. **Colatosti, M., N. Fantuzzi, P. Trovalusci, and R. Masiani, *New insights on homogenization for hexagonal-shaped composites as Cosserat continua.* Meccanica, 2022. 57(4): p. 885-904. 10.1007/s11012-021-01355-x.**

119. **Zhang, K., C. Wang, Y. Zhao, and J. Bi, *Experimental study on cracking behavior of concrete containing hole defects.* Journal of Building Engineering, 2023. 65: p. 105806. https://doi.org/10.1016/j.jobe.2022.105806.**

120. **Lin, Q., P. Cao, J. Meng, R. Cao, and Z. Zhao, *Strength and failure characteristics of jointed rock mass with double circular holes under uniaxial compression: Insights from discrete element method modelling.* Theoretical and Applied Fracture Mechanics, 2020. 109: p. 102692.**

121. **Pyl, L., K.-A. Kalteremidou, and D. Van Hemelrijck, *Exploration of the design freedom of 3D printed continuous fibre-reinforced polymers in open-hole tensile strength tests.* Composites Science and Technology, 2019. 171: p. 135-151. https://doi.org/10.1016/j.compscitech.2018.12.021.**

122. **Zeng, C., L. Liu, W. Bian, J. Leng, and Y. Liu, *Compression behavior and energy absorption of 3D printed continuous fiber reinforced composite honeycomb structures with shape memory effects.* Additive Manufacturing, 2021. 38: p. 101842.**

123. **Zienkiewicz, O.C. and R.L. Taylor, *The finite element method, ; volume 1: basic formulation and linear problems*1994.**

124. **Ya, S., S. Eisenträger, C. Song, and J. Li, *An open-source ABAQUS implementation of the scaled boundary finite element method to study interfacial problems using polyhedral meshes.* Computer Methods in Applied Mechanics and Engineering, 2021. 381: p. 113766.**

125. Song, C., *The scaled boundary finite element method: introduction to theory and implementation*2018: John Wiley & Sons.
126. Xu, H.H., H.C. Luo, X.G. Zhang, W. Jiang, X.C. Teng, W.Q. Chen, J. Yang, Y.M. Xie, and X. Ren, *Mechanical properties of aluminum foam filled re-entrant honeycomb with uniform and gradient designs.* International Journal of Mechanical Sciences, 2023. 244: p. 108075. https://doi.org/10.1016/j.ijmecsci.2022.108075.

127. Vincent, V.A., C. Kailasanathan, V.K. Shanmuganathan, J.V.S.P. Kumar, and V.R. Arun Prakash, *Strength characterization of caryota urens fibre and aluminium 2024-T3 foil multi-stacking sequenced SiC-toughened epoxy structural composite.* Biomass Conversion and Biorefinery, 2022. 12(9): p. 4009-4019. 10.1007/s13399-020-00831-w.

128. Yang, B., K. Fu, J. Lee, and Y. Li, *Artificial Neural Network (ANN)-Based Residual Strength Prediction of Carbon Fibre Reinforced Composites (CFRCs) After Impact.* Applied Composite Materials, 2021. 28(3): p. 809-833. 10.1007/s10443-021-09891-1.

129. Atuanya, C.U., M.R. Government, C.C. Nwobi-Okoye, and O.D. Onukwuli, *Predicting the mechanical properties of date palm wood fibre-recycled low density polyethylene composite using artificial neural network.* International Journal of Mechanical and Materials Engineering, 2014. 9(1): p. 7. 10.1186/s40712-014-0007-6.

130. Nanda, B.P. and A. Satapathy, *An Analysis of the Sliding Wear Characteristics of Epoxy-Based Hybrid Composites Using Response Surface Method and Neural Computation.* Journal of Natural Fibers, 2021. 18(12): p. 2077-2091. 10.1080/15440478.2020.1722781.

131. Omrani, E., P.L. Menezes, and P.K. Rohatgi, *State of the art on tribological behavior of polymer matrix composites reinforced with natural fibers in the green materials world.* Engineering Science and Technology, an International Journal, 2016. 19(2): p. 717-736. https://doi.org/10.1016/j.jestch.2015.10.007.

132. Teimouri, A., R. Barbaz Isfahani, S. Saber-Samandari, and M. Salehi, *Experimental and numerical investigation on the effect of core-shell microcapsule sizes on mechanical properties of microcapsule-based polymers.* Journal of Composite Materials, 2022. 56(18): p. 2879-2894. 10.1177/00219983221107831.

133. Vahdati, M., M. Moradi, and M. Shamsborhan, *Modeling and Optimization of the Yield Strength and Tensile Strength of Al7075 Butt Joint Produced by FSW and SFSW Using RSM and Desirability Function Method.* Transactions of the Indian Institute of Metals, 2020. 73(10): p. 2587-2600. https://doi.org/10.1007/s12666-020-02075-8.

134. Heidarzadeh, A., H. Khodaverdizadeh, A. Mahmoudi, and E. Nazari, *Tensile behavior of friction stir welded AA 6061-T4 aluminum alloy joints.* Materials & Design, 2012. 37: p. 166-173. https://doi.org/10.1016/j.matdes.2011.12.022.

135. **Bala, N., M. Napiah, and I. Kamaruddin, *Performance evaluation of composite asphalt mixture modified with polyethylene and nanosilica.* International Journal of Civil Engineering and Technology, 2017. 8(9): p. 616-628.**

136. **Saada, K., M. Zaoui, S. Amroune, R. Benyettou, A. Hechaichi, M. Jawaid, M. Hashem, and I. Uddin, *Exploring tensile properties of bio composites reinforced date palm fibers using experimental and Modelling Approaches.* Materials Chemistry and Physics, 2024. 314: p. 128810.**

137. **Saada, K., S. Amroune, and M. Zaoui, *Prediction of mechanical behavior of epoxy polymer using Artificial Neural Networks (ANN) and Response Surface Methodology (RSM).* Frattura ed Integrità Strutturale, xx, 2023.**

138. **Makhlouf, A., A. Belaadi, M. Boumaaza, L. Mansouri, M. Bourchak, and M. Jawaid, *Water absorption behavior of jute fibers reinforced HDPE biocomposites: Prediction using RSM and ANN modeling.* Journal of Natural Fibers, 2022. 19(16): p. 14014-14031.**

139. **Quiles-Carrillo, L., R. Balart, T. Boronat, S. Torres-Giner, D. Puglia, F. Dominici, and L. Torre, *Development of compatibilized polyamide 1010/coconut fibers composites by reactive extrusion with modified linseed oil and multi-functional petroleum derived compatibilizers.* Fibers and Polymers, 2021. 22: p. 728-744.**

140. **Benyettou, R., S. Amroune, M. Slamani, Y. Seki, A. Dufresne, M. Jawaid, and S. Alamery, *Assessment of induced delamination drilling of natural fiber reinforced composites: a statistical analysis.* Journal of Materials Research and Technology, 2022. 21: p. 131-152. https://doi.org/10.1016/j.jmrt.2022.08.161.**

141. **Adeyi, A.J., O. Adeyi, E.O. Oke, O.A. Olalere, S. Oyelami, and A.D. Ogunsola, *Effect of varied fiber alkali treatments on the tensile strength of Ampelocissus cavicaulis reinforced polyester composites: Prediction, optimization, uncertainty and sensitivity analysis.* Advanced Industrial and Engineering Polymer Research, 2021. 4(1): p. 29-40. https://doi.org/10.1016/j.aiepr.2020.12.002.**

142. **Ahmad, A., M.A. Lajis, N.K. Yusuf, and S.N. Ab Rahim, *Statistical optimization by the response surface methodology of direct recycled aluminum-alumina metal matrix composite (MMC-AlR) employing the metal forming process.* Processes, 2020. 8(7): p. 805.**

Publications and Conferences

Publications:

- Saada, K., M. Zaoui, S. Amroune, R. Benyettou, A. Hechaichi, M. Jawaid, M. Hashem, and I. Uddin, Exploring tensile properties of bio composites reinforced date palm fibers using experimental and Modelling Approaches. Materials Chemistry and Physics, 2024. 314: p. 128810.

- Saada, K., C. Farsi, S. Amroune, M. Fnides, M. Zaoui, and H. Heraiz, Examining the bending test properties of bio-composites strengthened with fibers through a combination of experimental and modeling approaches. Journal of Composite Materials, 2024: p. 00219983241240819. 10.1177/00219983241240819.

- Saada, K., S. Amroune, and M. Zaoui, Prediction of mechanical behavior of epoxy polymer using Artificial Neural Networks (ANN) and Response Surface Methodology (RSM). Frattura ed Integrità Strutturale, xx, 2023.

- Saada, K., S. Amroune, M. Zaoui, A. Houari, K. Madani, and A. Hachaichi, Experimental and Numerical Study of the Effect of the Presence of a Geometric Discontinuity of Variable Shape on the Tensile Strength of an Epoxy Polymer. Acta Mechanica et Automatica, 2023. 17(2): p. 192-199.

- Benyettou, R., S. Amroune, M. Slamani, K. Saada, H. Fouad, M. Jawaid, and S. Sikdar, Modelling and optimization of the absorption rate of date palm fiber reinforced composite using response surface methodology. Alexandria Engineering Journal, 2023. 79: p. 545-555. https://doi.org/10.1016/j.aej.2023.08.042.

- Amroune, S., A. Belaadi, M. Zaoui, N. Menaseri, B. Mohamad, K. Saada, and R. Benyettou, Manufacturing of rapid prototypes of mechanical parts using reverse engineering and 3D Printing. Journal of the Serbian Society for Computational Mechanics/Vol, 2021. 15(2): p. 1-10.

- ZERGANE, S., S. AMROUNE, M. SLAMANI, K. SAADA, M. ZAOUI, C. FARSI, and A. BAKHTI, INVESTIGATION FOR THE AUTOMATED GENERATION OF TOOLPATHS ON A 3AXIS CNC MACHINE. ACADEMIC JOURNAL OF MANUFACTURING ENGINEERING, 2024. 22(1).

- ZERGANE, S., S. AMROUNE, M. SLAMANI, M. ZAOUI, C. FARSI, K. SAADA, and A. BAKHTI, G-CODE GENERATION FOR MACHININING SPUR GEAR IN CNC MACHINES USING THE IMACHINING STRATEGY. Academic Journal of Manufacturing Engineering, 2023. 21

Conferences:

- Participation à “1st International Conference on Innovative Academic Studies on 10-13 September in 2022 at Konya/Turkey”.Sous le titer:” Surface method (RSM) and artificial neural networks (ANN) for modeling tensile mechanical of natural fibers”
- Participation à “1st International Conference on Innovative Academic Studies on 10-13 September in 2022 at Konya/Turkey”.Sous le titer:” Numerical study of mechanical properties and crack propagation in a 2024 T3 Aluminum plate”

- Participation à “2nd International Conference on Engineering and Applied Natural Sciences on 15-18 October in 2022 at Konya/Turkey”.Sous le titer:” The effect of the meshing technique on cracking and its extension in a bio composite plate”

- Participation à “2nd International Conference on Engineering and Applied Natural Sciences on 15-18 October in 2022 at Konya/Turkey”.Sous le titer:” The effect of fiber orientation on the thermo mechanical properties of bio composites”

- Participation à “2nd International Conference on Engineering and Applied Natural Sciences on 15-18 October in 2022 at Konya/Turkey”.Sous le titer:” Analysis of the effect of cutting conditions for circularity and cylindricity errors for drilling bio composites”

- Participation à “2nd International Seminar on Industrial Engineering and Applied Mathematics (Isieam'22) In Skikda (Algeria), October 23 & 24th, 2022”.Sous le titer:” STUDY AND NUMERICAL SIMULATION OF THE STRESS INTENSITY FACTOR OF CRACKED PLATES

- Participation à “2nd International Seminar on Industrial Engineering and Applied Mathematics (Isieam'22) In Skikda (Algeria), October 23 & 24th, 2022”.Sous le titer:” Investigation of machinability of biocomposites reinforced by natural fibers: artificial neuron network (ANN)”

- Participation à “ST National Conference on Mechanics and Materials NCMM’2023, 06 - 07 December 2023, Boumerdes University- Algeria” Sous le titer:” NUMERICAL ANALYSIS OF THE EFFECT OF FORCES ON THE CRACK IN A COMPOSITE PLATE IN ABAQUS SOFTWARE

- Participation à “Le 2ème colloque national de chimie (CNC2@2024)6 - 7 mai 2024, Msila University- Algeria” Sous le titer:” Analysis of Stresses and Boundary Conditions in Unidirectional Jute-Reinforced Polymer Composites: A Tensile Testing Approach and Finite Element Modeling